Geochemistry of Magnetitite Layers in the Upper Zone of the Bushveld Complex, South Africa

By

Ramphelane Prince Maila

A Dissertation submitted to the School of Geosciences, University of the Witwatersrand, Johannesburg, South Africa in fulfilment of the requirements for the degree of Master of Science

May 2015

Declaration

I declare that this dissertation is my own, unaided work. It is being submitted for the Degree of Master of Science at the University of the Witwatersrand, Johannesburg. It has not been submitted before for any degree or examination in any other University.

_____ Date: _____

Ramphelane Prince Maila

School of Geosciences
University of the Witwatersrand
Johannesburg
May 2015

Abstract

The Upper Zone (UZ) of the Bushveld Complex (BC) comprises several magnetitite layers throughout the entire sequence with the most prominent layer, the 2 m thick Main Magnetitite Layer (MML), located towards the base of the sequence. Magnetite mineral separates have been obtained from the UZ with particular focus on the MML in vertical profiles through the MML, Layer 1 and bifurcations of the MML, as well as profiles along the base of the MML and bifurcations. Magnetite mineral separates were also collected from Bierkraal and UCAR mine drill cores. The magnetite mineral separates were analyzed primarily for Cr and V as these two elements have the highest partition coefficients (D>200 and D=20-25 respectively) in magnetite and can be used as magmatic tracers. Electron microprobe data from the Bellevue drill core are also included. The gradational upper contacts of magnetitite layers with overlying anorthosite could be interpreted to suggest that the magnetitite layers accumulated through crystal settling. However, vertical profiles through 1 m of the MML all show an upward exponential decrease in Cr content (12 000-580 ppm) which is inconsistent with crystal settling but better explained by diffusion controlled bottom crystallization. The sharp base of the MML with the underlying anorthosite may suggest that the MML crystallized due to an abrupt event. The MML is not entirely homogeneous as evidenced by lateral heterogeneity along the base of the MML, identified by irregular Cr concentrations along the base of the MML and magnetitite bifurcations. This heterogeneity further supports the contention that the magnetitite layers are a product of diffusion controlled bottom crystallization. Reversals in Cr content, of differing magnitudes, in 3 of 4 vertical profiles above a dome structure interrupting the MML and in 2 of 4 vertical profiles through the MML, are attributed to intermittent convection on various scales bringing primitive undepleted magma into the crystallization zone. The magnitude of the reversals depends on the level to which the convection descends. The feldspar parting, a 10 cm thick horizon with cumulus plagioclase 1 m above the base of the MML, appears at a fairly constant Cr content in magnetite. The lack of a chemical break immediately above the feldspar parting suggests a physical process, such as pressure change, as a mechanism to account for the mineralogical change from the feldspar parting into massive magnetite in the upper portion of the MML. Vanadium, unlike Cr shows no systematic trends. Vanadium content of magnetitite layers is found to be comparable to that of the disseminated magnetite thus ruling out the possibility of a change in fo_2 as a mechanism to induce magnetite crystallization. Disseminated magnetite in the UZ is suggested to have re-equilibrated with pyroxene and/or olivine during subsolidus

cooling resulting in lower MgO contents of the disseminated magnetite compared to that of massive magnetitite layers. Similarities between magnetitite layers in Magnet Heights (eastern lobe); UCAR mine drill core, east of Brits (western lobe); Bierkraal drill core, north of Rustenburg (western lobe) and Bellevue drill core (northern limb) suggest that the different lobes of the BC may be connected.

Acknowledgements

I would like to thank my supervisor Prof. Grant Cawthorn for his invaluable support and insight during the course of the completion of this dissertation. Funding from the National Research Fund is acknowledged. I would like to thank David Long from Sci-Ba Laboratories and Scientific Consultations for laboratory technical assistance. I would like to thank Neo Makhohlisa (Mine Manager) for allowing access to Evraz Mapochs mine and Thapelo Mphahlele (Geologist) for his assistance during the mine visit.

I would also like to thank my fellow student peers Khuliso Masindi, Mehrnaz Siahil and Siyanda Mgandi for support and encouragement.

Table of Contents

List of Figures

List of Tables

Chapter 1 – Introduction

Layered mafic intrusions (LMI) have for many years been a major subject of study for petrologists worldwide. These LMI provide a vast insight into the processes operating during magmatic differentiation. Studies considering different aspects regarding LMI have been carried out in an attempt to understand these rather complex geological entities. One aspect involves the study of the wealth of economic mineralization commonly associated with LMI. Amongst these, are Fe-Ti oxides which are commonly mined for either titanium (ilmentite) or vanadium (titanomagnetite).

The geochemistry of Fe-Ti oxides have been widely documented in several LMI around the world; USA (Dymek and Owens, 2001); China (Zhou et al., 2005; Howarth et al., 2013; Chen et al., 2013; Pang et al., 2008), India (Roy, 1956; Vidyashankar and Govidaiah, 2009; Saha et al., 2010), Ukraine (Duchesne et al., 2006), Norway (Duchesne, 1972; Jensen et al., 1993), Canada (Namur et al., 2010), South Africa (Bateman, 1951; Willemse, 1969; Molyneux, 1972; Reynolds, 1985a; Tegner et al., 2006; Cawthorn and Ashwal, 2009; Maier et al., 2013; Cawthorn, 2013) and others (Lister, 1966; Morse, 1980; Carmichael, 1967; Juliusz, 2000). Insight into the petrogenesis of Fe-Ti oxides has been gained also through experimental work (Buddington and Lindsley, 1964; Toplis and Carroll, 1995; Schuiling and Feenstra, 1980; Hill and Sack, 1987; Lindh, 1973; Philpotts and Doyle, 1983; Toplis and Corgne, 2002; Veksler et al., 2006, 2007).

Compositions of Fe and Ti oxides can be separated into three major solid solution series; magnetite-ulvöspinel (Fe_3O_4-Fe_2TiO_4) (the titanomagnetite series), hematite-ilmenite (Fe_2O_3-$FeTiO_3$ (the titanohematite series), and pseudobrookite-“ferropseudobrookite” (Fe_2TiO_5-$FeTi_2O_5$) (Pearce et al., 2010). Increasing the degree of oxidation of the magnetite-ulvöspinel solid solution, the main focus here, results in intergrowths of ilmenite lamellae along the (111) planes. At the slowest rate of cooling, highest subsolidus temperatures and increased oxidation, ilmenite granules may exsolve from the magnetite-ulvöspinel solid solution series.

The Fe-Ti oxides of the Bushveld Complex (BC) are part of the titanomagnetite series with a minor amount of discrete ilmenite grains (Von Gruenewaldt et al., 1985). The oxides are commonly concentrated in the form of stratiform magnetitite layers or are sparsely

disseminated through the Upper Zone (UZ). The Fe-Ti oxides are also concentrated as magnetitite plugs which occur both in the MZ and UZ (Von Gruenewaldt, 1973; Molyneux, 1974; Scoon and Mitchell, 1994, 2012). Geological relationships of Ti-magnetitite layers with their host rocks suggest that the layers are an integral part of the BC (Reynolds, 1985a). For that reason, it is imperative to understand the genesis of Ti-magnetitite layers in the quest of understanding the processes and mechanisms that operated during the crystallization of LMI. The focus of this study is to determine compatible trace element concentration data from pure magnetite separates in order to model crystallization processes, especially of magnetitite layers.

1.1. Geology

The Bushveld Complex is by far the world's largest LMI, spanning an area of ~65 000 km^2. This large LMI hosts several of the world's most prestigious economic deposits (Willemse, 1969). Dated at ~2060 Ma, the BC comprises five limbs (Fig. 1.1.) (Cawthorn and Walraven, 1998). A number of stratigraphic subdivisions, based on mineralogy of the different rock types, have been distinguished namely; Marginal Zone, Lower Zone (LZ); Critical Zone (CZ); Main Zone (MZ); Upper Zone (UZ) and the Roof Zone (RZ) (Fig. 1.2) (Hall, 1932; Cawthorn and Walraven, 1998, Cawthorn, 2013). Unlayered, medium-grained rocks comprising chiefly norite with minor pyroxenite define the lowermost basal unit, the Marginal Zone (Cawthorn et al., 2006). Overlying it is the LZ ranging in thickness from 0-1000m. This unit comprises layers of pyroxenite, harzburgite and dunite, which are suggested to be the product of episodes of magma addition (Cawthorn and Walraven, 1998; Boorman et al., 2004). World renowned Platinum Group Elements (PGE) deposits (UG2, Merensky reef and Platreef) along with a number of chromitite layers are hosted in the CZ (Cawthorn et al., 2006; Cawthorn, 1999). Up to seven of the chromitite layers can be distinguished in the lower pyroxenitic unit (C_LZ) whereas up to five of the prominent layers can be distinguished in the upper CZ (C_UZ) (Cawthorn and Walraven, 1998; Cawthorn, 2007). The C_UZ shows more defined layering than the C_LZ and comprises rhythmic units of chromitite, pyroxenite, norite and anorthosite (Cawthorn and Walraven, 1998). Overlying the CZ, the MZ is characterized by a thick package, varying in thickness across the BC (2200 m western BC and 3100 m eastern BC), of norite and gabbronorite with minor pyroxenite and anorthosite layers (Von Gruenewaldt, 1973). A thin layer of orthopyroxenite, termed the pyroxenite marker (PM), within the MZ can be traced along strike across the eastern and western BC (Von

Gruenewaldt, 1973; Molyneux, 1974). A short distance above the PM, the appearance of cumulus magnetite marks the base of the overlying unit, the UZ (Cawthorn and Walraven, 1998).

The UZ is ~2 km thick and hosts the largest vanadium ore deposit in the world (Willemse, 1969). This unit has been subdivided into subzones; A, B and C. The appearance of cumulus magnetite marks the base of subzone A, comprising magnetite-bearing leucogabbronorite, gabbronorite, gabbro and anorthosite. Cumulus Fe-rich olivine marks the base of subzone B which chiefly comprises magnetite gabbro along with minor olivine bearing magnetite gabbro (Harney and Von Gruenewaldt, 1995). The appearance of cumulus apatite marks the base of subzone C which comprises chiefly magnetite gabbro and magnetite bearing olivine diorite however, olivine free rocks are present in the vicinity of magnetitite layers (Von Gruenewaldt, 1976). In view of the recognition by Hall (1932) and re-examined by Cawthorn (2013) of more evolved rocks, there should be included a RZ with rocks with no clear cumulus texture and containing abundant hornblende, quartz and alkali feldspar in addition to plagioclase, olivine, pyroxenes, oxides and apatite. A striking feature of the UZ is the presence of magnetitite layers throughout the entire sequence. Twenty five magnetitite layers have been identified in the east. Three of the layers (lower layers -1 to -3) are situated below the prominent Main Magnetitite Layer (MML) and the remaining layers (1-21) are situated above the MML (Fig. 1.3) (Harney and Von Gruenewaldt, 1995). The cumulative thickness of the magnetitite layers is ~20.4 m (Tegner et al., 2006) with individual layers ranging in thickness from 0.1 m to 10 m (Harney and Von Gruenewaldt, 1995). The magnetitite layers show a remarkable lateral continuity. The MML best displays the lateral continuity of these layers, extending 100 km in the eastern (Cawthorn, 1994), 200 km in the western and 100 km in the northern limbs of the BC (Reynolds, 1985a). Relationships of the magnetitite layers with host rocks typically show sharp lower contacts with underlying anorthosite whereas the upper contacts are gradational into anorthosite (Reynolds, 1985b; McCarthy et al., 1985). In the upper layers are nelsonite (Fe-Ti-P) layers (Reynolds, 1985a). Throughout the UZ sulfides are rare but may occur with magnetitite layers (Von Gruenewaldt, 1976).

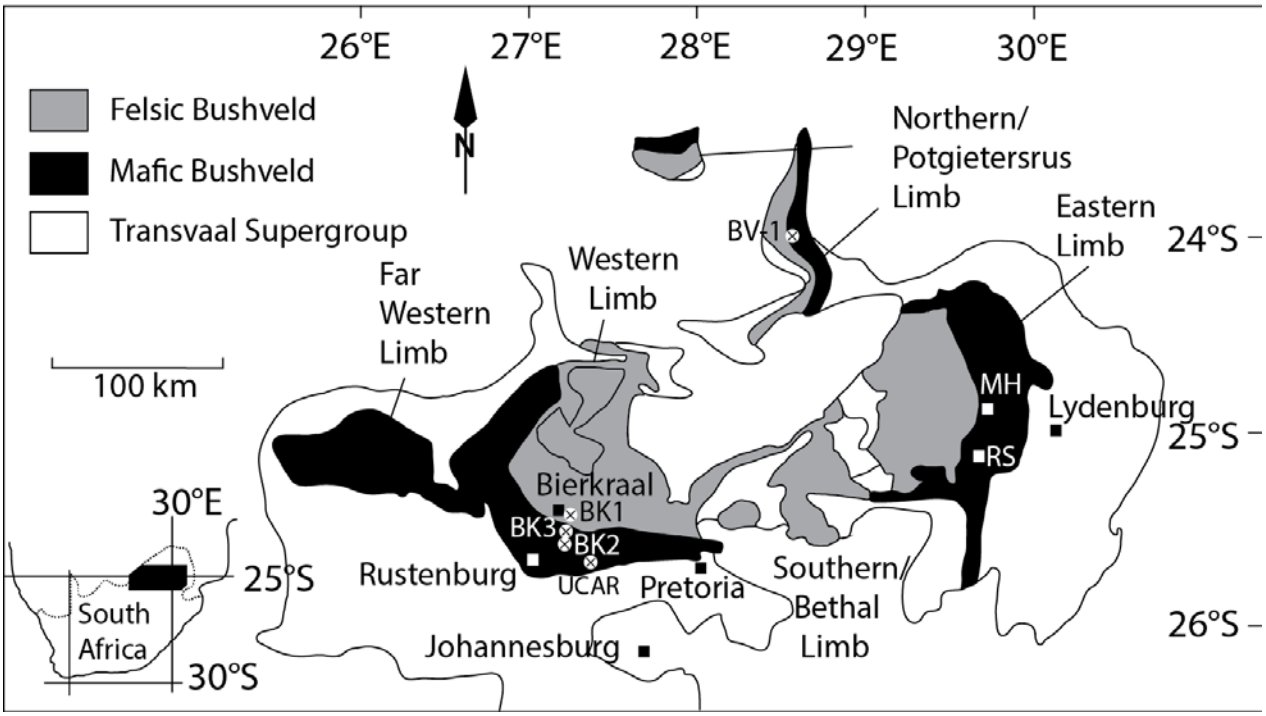

Fig. 1.1. Geological map of the Bushveld Complex. Four limbs (northern, eastern, western and southern) and localities of BK1, BK2 and BK3; BV-1 and UCAR mine drill cores are shown. MH=Magnet Heights; RS=Roossenekal (modified Tegner et al., 2006).

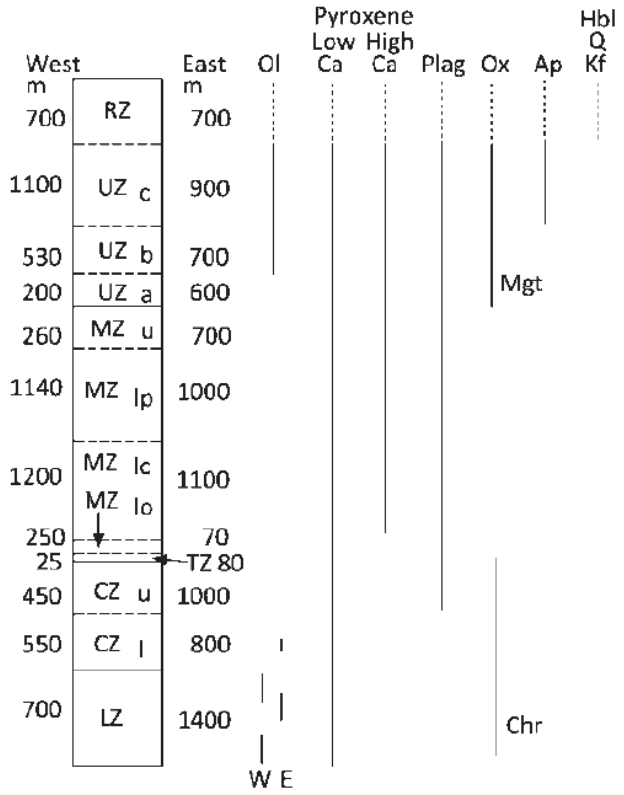

Fig. 1.2. General stratigraphy of the Bushveld Complex (Cawthorn, 2013).

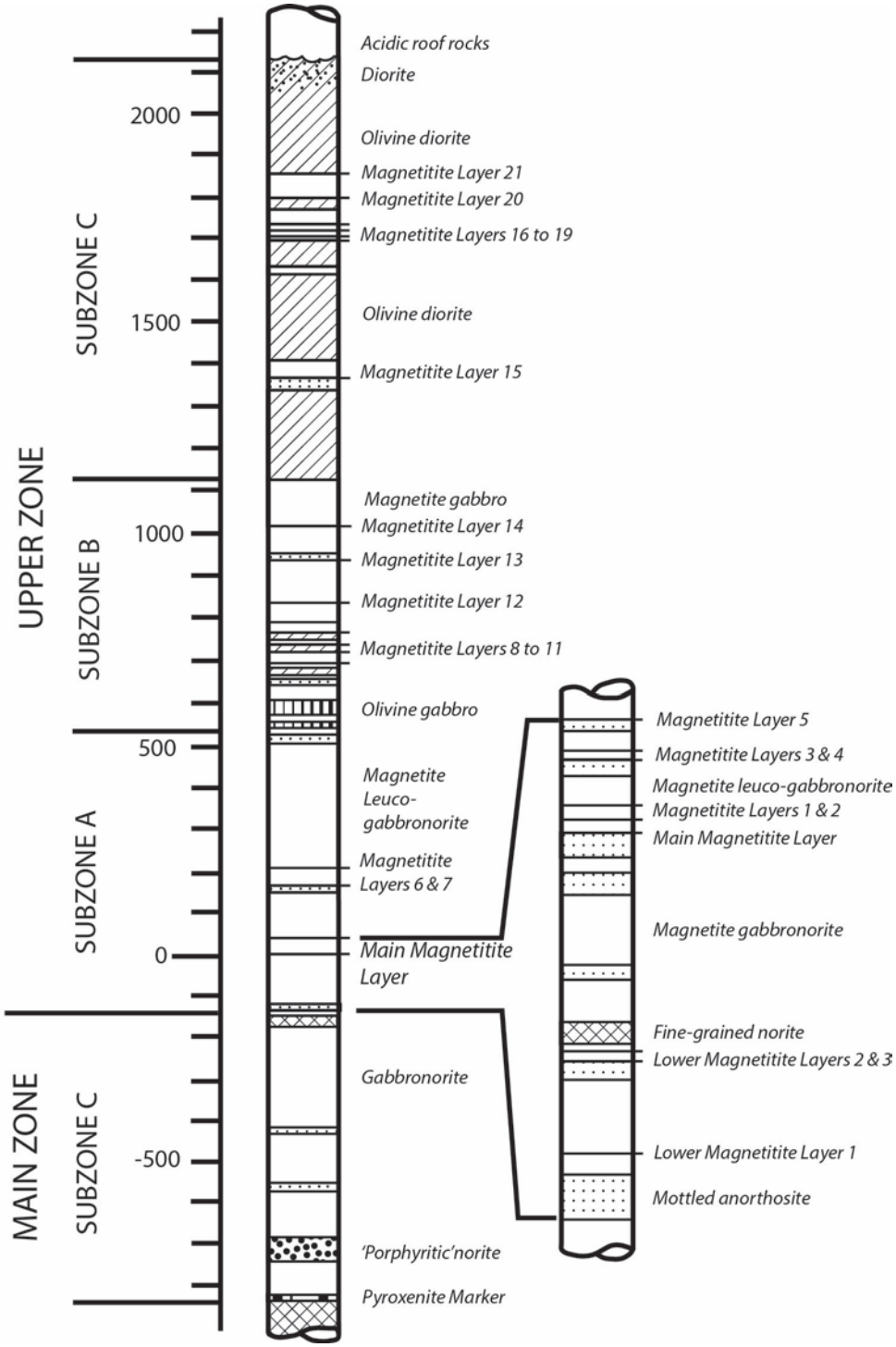

Fig. 1.3. Stratigraphic position of magnetitite layers in the Upper Zone of the Bushveld Complex (modified after Harney and Von Gruenewaldt, 1995).

1.2. Petrography of Fe-Ti Oxides

Much work has been done on the petrography of Fe-Ti oxides (Buddington and Lindsley, 1964; Willemse, 1969; Molyneux, 1970; Von Gruenewaldt et al., 1985; Reynolds, 1985b; Klemm et al., 1985; Butcher and Merkle, 1987). The grain size of magnetite in the BC varies depending on surrounding minerals. In sections where only magnetite is present, the grains are commonly coarse grained reaching up to 1 cm in diameter in the magnetitite layers, whereas in sections where magnetite is adjacent to silicates the magnetite grains are commonly smaller (0.1-2 mm) (Reynolds, 1985a; Butcher and Merkle, 1987). Magnetite-magnetite grain boundaries are commonly polygonal with an interfacial angle of 120° whereas magnetite-silicate boundaries are more irregular (Butcher and Merkle, 1987). Several exsolution textures can be observed in Fe-Ti oxides with the most common texture being a cloth texture intergrowth of magnetite and ulvöspinel (Reynolds, 1985b). Other exsolution phases commonly present include ilmenite, pleonaste, corundum and an Al-Mg spinel. The size of the exsolution phases within the magnetite are variable ranging from 5 to 100µm (Von Gruenewaldt et al., 1985). Small granular ilmentite grains may be found interstitial between magnetite grains (Reynolds, 1985b). The composition of magnetite lying between exsolution phases in the magnetite depends on the type of exsolution phases present (Reynolds, 1985b; Von Gruenewaldt et al., 1985). No further detailed work has been undertaken on the petrography in this study, but awareness of these textures is important in undertaking analysis and interpretation discussed below.

1.3. Models for Fe-Ti Oxide Layer Formation

Several mechanisms have been proposed to explain the formation of the Fe-Ti oxide layers in LMI. The mechanisms have evolved over the years as a consequence of increased experimental work on Fe-Ti oxides. Many of the processes involved are analogous to processes which have been put forward for the genesis of chromitite layers also hosted in LMI.

1.3.1. Crystal Settling and Sorting

Crystal settling and sorting is a mechanism which has been proposed to explain layering commonly observed in LMI (Wager and Brown, 1968). Differential settling rates of different minerals, as a function of their density, size and magma viscosity, may result in modally graded layers commonly observed in LMI (Wager and Brown, 1968; Maaløe, 1978; Campbell, 1978; Naslund and McBirney, 1996; Cawthorn and Ashwal, 2009). The sharp base and gradational upper contacts of the magnetitite layers of the UZ may be taken as evidence in support of crystal settling and sorting (Cawthorn et al., 2005). If it is assumed that the magma was crystallizing magnetite, pyroxene and plagioclase, it is possible that magnetite may have sunk and accumulated at the bottom followed by pyroxene and plagioclase creating a sharp base and gradational upper contacts. Sharp bases and gradational upper boundaries of the magnetitite layers observed in the Panzhihua and Hongge intrusions, China have been suggested to be evidence for crystal settling and sorting taking place (Zhou et al., 2005; Bai et al., 2012). The absence of pyroxene in the gradational upper contacts of the magnetitite layers, however creates a problem for gravity sorting mechanism (Cawthorn and Ashwal, 2009; Cawthorn et al., 2005).

1.3.2. Magma Addition

The introduction of more primitive magma into the magma chamber where it may mix with the residual magma has received some support as a genetic mechanism to explain several economic horizons in LMI (Irvine, 1977; Campbell, 1983; Naldrett et al., 2012). The introduction of primitive magma may drive the composition of the resultant magma into the spinel stability field where spinel only will crystallize without other minerals thus resulting in

a monomineralic layer (Naslund and McBirney, 1996; Cawthorn et al., 2005). Although this process has only been experimentally shown to be plausible for the crystallization of chromitite layers, this process may also apply to magnetitite layers if the addition of new magma will result in magnetite saturation. Magma addition commonly involves a change in mineral composition across the level of the suggested mixing event (Naslund and McBirney, 1996). Ashwal et al. (2005) noted a number of compositional reversals in the UZ. They attributed the reversals to mixing of the residual magma with a different magma with a similar isotopic composition. Reversals in plagioclase composition have been documented in the UZ, however, are never coincident with the stratigraphic position of magnetitite layers (Ashwal et al., 2005; Tegner et al., 2006; Cawthorn and Ashwal, 2009). Therefore, the lack of compositional reversals coincident with magnetitite layers argues against magma addition as a mechanism for the formation of the magnetitite layers (Cawthorn and Ashwal, 2009; Cawthorn et al., 2005). Furthermore, the uniformity of initial Sr isotope ratio suggests the UZ formed without magma addition (Kruger et al., 1987).

1.3.3. Rhythmic Layering

Variations in the proportions of plagioclase and olivine defining several layers namely mesocratic gabbro, melanocratic gabbro and leucocratic gabbro were observed by Maaløe (1978) in the Skaergaard layered intrusion. Rhythmic layering comprising olivine, and troctolite cumulates has also been observed in the Rhum layered intrusion by Maaløe (1978) who ascribed this kind of layering to oscillatory nucleation under supersaturated conditions at the crystal-liquid interface. In his model Maaløe (1978) suggested that the latent heat released during crystallization as a result of low cooling rates, is large enough to compensate for heat lost through conduction. This results in a situation whereby crystallization can take place at a constant temperature. In a two component system comprising A and B, the crystallization of A will drive the magma composition, along an isothermal path to cross the liquidus of A into a field where B may crystallize. Once B starts to crystallize it will drive the composition of the magma back to cross the liquidus of B back into a field where A may crystallize. Repetition of this process is suggested to result in the rhythmic layering observed, characterised by rhythmic variations in modal proportions of minerals.

1.3.4. Liquid Immiscibility

Through the evolution of experimental work (Philpotts, 1967; Philpotts and Doyle, 1983; Charlier and Grove, 2012), liquid immiscibility has received some support as a mechanism by which magnetitite layers may crystallize. Fe-rich immiscible liquid may separate from a magma under intermediate fO_2 (approximating QFM buffer) conditions leading to the crystallization of apatite-rich magnetitite layers (Philpotts, 1983). Namur et al. (2012) suggested Fe-Ti-P gabbros in Mega Cyclic Unit 2 (MCII) of the Sept Iles layered intrusion (Canada) to have originated from liquid immiscibility. They modeled the liquid line of descent of MCII of the intrusion and observed that the liquid line of descent entered the two liquid field postulated by Charlier and Grove (2012) where immiscibility may take place. Furthermore, they observed a bimodal distribution of bulk rock compositions in MCII which they attributed to liquid immiscibility. Moreover, they suggested nelsonite layers located in the uppermost portions of the UZ of the BC to be a result of liquid immiscibility. They demonstrated that the liquid line of descent of the Bushveld magma modeled by Tegner et al. (2006) entered the two liquid field postulated by Charlier and Grove (2012). Through experimental work, Philpotts (1967) observed a eutectic composition of two thirds by volume magnetite to one third apatite in the magnetite-fluorapatite system. A similar eutectic oxide: apatite ratio of 2:1 has also been distinguished in a number of nelsonite (Fe-Ti and apatite) rocks around the world, supporting the contention that the nelsonite layers may be a result of liquid immiscibility (Kolker, 1982). A number of apatite-enriched zones have been identified in the uppermost portions of the UZ (Reynolds, 1985b). These zones were shown by Von Gruenewaldt (1993) to comprise apatite content ranging from 6 to 20 vol%. Reynolds (1985b) attributed the presence of opaque oxide-apatite assemblage in the apatite enriched horizons in the UZ to liquid immiscibility. Liquid immiscibility, however, cannot explain the crystallization of most of the magnetitite layers occurring throughout the entire UZ as these layers commonly lack apatite (Cawthorn, 1985; Tegner et al., 2006). Furthermore, immiscible Fe-rich liquids were shown to only contain 30-40 % FeO, thus do not approach the composition of pure magnetitite (Cawthorn et al., 2005).

1.3.5. Changes in Oxygen Fugacity

Experimental work has shown oxygen fugacity (fO_2) to be a vital factor controlling the crystallization of magnetite and Fe-bearing phases (Toplis and Carol, 1995; Toplis and Corgne, 2002). The stability of Fe-Ti magnetite has been shown to be largely dependent on fO_2, with oxidizing conditions promoting the crystallization of magnetite (Toplis and Carol, 1995). Oxidation conditions affect the valence state and proportion of vanadium which can occur terrestrially as either V^{3+}, V^{4+} or V^{5+} (Toplis and Corgne, 2002). Based on textural features of the magnetite grains in massive magnetitite layers and disseminated magnetite of the BC, Von Gruenewaldt et al. (1985) concluded that the magnetitite layers crystallized at higher fO_2 than the disseminated magnetite. Furthermore, samples from the MML and layer 21 of the BC were shown to have similar V^{4+} ratios, suggesting they crystallized under similar fO_2 conditions (Balan et al., 2006). The partition coefficient (D) of V into magnetite increases with decreasing fO_2 (Toplis and Corgne, 2002). Klemm et al. (1985) noted a lower V_2O_5 content of the massive magnetitite layers when compared to disseminated magnetite in the host rocks and concluded that the magnetitite layers must have crystallized under higher fO_2 conditions than the disseminated magnetite. Sources for the introduction of fO_2 into the system have been proposed including CO_2 degassing of footwall rocks (Howarth et al., 2013) and volatile diffusion from underlying cumulates (Klemm, 1985). Although a change in fO_2 can account for a change in crystallizing mineralogy, the lateral continuity of the magnetitite layers located in the BC necessitates oxygen to be introduced instantaneously and homogeneously, over hundreds of km strike, which is rather difficult to envisage. Furthermore, the source of oxygen introduced into the system as a mechanism to abruptly change the fO_2 still remains elusive (Cawthorn and McCarthy, 1981; Harney and Von Gruenewaldt, 1995).

1.3.6. Diffusion Controlled Bottom Crystallization

In-situ crystallization has been suggested to take place in LMI (Jackson, 1961; Campbell, 1978; Martin, 1990). It has been shown that the degree of supercooling of the magma is the major control on the type of nucleation namely: homogeneous or heterogeneous crystallization. The amount of supercooling required for heterogeneous crystallization is much smaller than that required for homogeneous crystallization (Martin, 1990; Campbell, 1978). The bottom of LMI presents preferable conditions for in-situ crystallization as pre-

existing crystals at the bottom allow for new crystals to nucleate (Campbell, 1978). Trace element modeling is one of the most useful techniques employed in tracing fractionation in LMI. Cr can be used to trace crystallization processes of magnetite as it has a high partition coefficient (D>200) (Irving, 1978) into magnetite. An upward decrease in Cr content of magnetite has been observed in the MML (Cawthorn and McCarthy, 1980, 1981; McCarthy et al., 1985). This upward decrease has also been observed on a smaller scale in a 2cm magnetite grain from a sample collected at the base of the MML (Cawthorn, et al., 1983). Furthermore, a number of reversals in the Cr content of the MML were noted by Cawthorn and McCarthy (1980). Crystallizing magnetite at the base of the magma chamber can locally deplete the magma in Cr thus resulting in a magma becoming inhomogeneous. The local depletion of Cr results in a decrease in the Cr content of later crystallizing magnetite. However, convection can bring more primitive, undepleted magma from higher in the magma chamber into the crystallization front thus resulting in a higher Cr content of the newly crystallized magnetite. Cawthorn and McCarthy (1980, 1981) have attributed observed Cr gradients and reversals in Cr content of the MML to this sort of diffusion controlled bottom crystallization within an inhomogeneous magma.

1.3.7. Changes in Pressure

Episodic pressure fluctuation has also received some attention as a possible mechanism by which magnetitite layers may crystallize. Osborn (1978) showed that an increase in pressure results in the increase in the stability of spinel and pyroxene fields at the expense of plagioclase and olivine. In light of experimental work, Cameron (1978) concluded that chromitite layers located in the CZ crystallized as a consequence of a change in pressure. This process may also be applied to magnetitite layers. A major observation in the support for pressure fluctuation is the lateral continuity of both the chromitite and magnetitite layers. A fluctuation in pressure, unlike a fluctuation in oxygen fugacity, may result in a uniform pressure change simultaneously across the entire strike length. Several mechanisms to change the pressure including magma addition to the chamber and tectonics have been suggested (Cameron, 1978; Cawthorn and McCarthy, 1981).

1.3.8. Double-Diffusive Layering

Double-diffusive convection is convection created in an unstable, stratified liquid as a result of differential diffusion rates of temperature and the components controlling the density of the liquid (Radko and Smith, 2012). A necessity for double-diffusive convection is that the components have opposing effects on the density of the liquid (Naslund and McBirney, 1996). This process is a naturally occurring phenomenon which has been documented in oceans and saline lakes but has also been postulated in LMI (Naslund and McBirney, 1996; Irvine et al., 1983; Huppert, 1984). Kruger and Smart (1987) demonstrated that the reversals in Cr contents of the MML observed by Cawthorn and McCarthy (1981) may be explained by the breakdown and mixing of adjacent double-diffusive layers. A change in Sr and Sr/Al_2O_3 ratio in plagioclase above and below the MML has been documented by Harney et al. (1996). They attributed this compositional change to the breakdown and mixing of adjacent double-diffusive layers. Tegner et al. (2006), however, observed no change in the plagioclase composition above and below the magnetitite layers. Furthermore, Tegner et al. (2006) proposed a mechanism in which a magma may become inhomogeneous leading to the development of double-diffusive layering. The crystallization of a gabbronoritic mineral assemblage from the magma results in a residual magma of higher density which will not be able to circulate back to the top, but rather pond at the bottom of the magma chamber. This situation creates a stable vertical density profile and may result in the development of double diffusive layering (Tegner et al., 2006). Tegner et al. (2006) postulated 'fractionation cycles', some of which were found to be coincident with magnetitite layers. The protracted lowering of the density of the lowermost layer as a consequence of magnetite crystallization causes the density of the lower layer to equal the density of the overlying layer. This situation results in the breakdown of the diffusive layer boundary between the two layers allowing them to mix. The observation that some of the 'fractionation cycles' are coincident with magnetitite layers led Tegner et al. (2006) to the conclusion that the magnetite layers are a result of normal fractional crystallization. However, not all cycles are coincident with magnetitite layers.

1.3.9. Magma Currents

Modally graded layering in LMI has been suggested to be the result of crystal-laden density currents depositing material as they sweep across the floor (Wager and Brown, 1968; Irvine, 1980, 1998; Naslund and McBirney, 1996; Maier et al., 2013).This mechanism is analogous with the formation of graded sedimentary rocks formed by turbidity currents. As a dense slurry of crystals sweeps across the floor, the denser minerals sink first leaving the less dense minerals to be deposited on top (Irvine, 1987). This mechanism has been previously invoked to explain modally graded layering observed in the Skaergaard intrusion (Wager and Brown, 1968; Irvine, 1980, 1998). Maier et al. (2013) re-evaluated the crystallization of the BC and suggested that post emplacement subsidence in the center of the BC resulted in semi-consolidated cumulate layers flowing down dip, as crystal-laden slurries, from the edges towards the center of the intrusion. Cumulate unmixing occurred during the flow of crystal-laden slurries resulting in density sorting with plagioclase being separated from denser pyroxene and oxides. Maier et al. (2013) suggested the heterogeneity, in terms of Cr, along the base of the MML to reflect compositional variation inherent in the slurry that deposited the MML. They argued that large early-formed Cr-rich magnetite grains were concentrated at the base of the slurry and were subsequently deposited at the base of the MML. As a result of post depositional sintering, any textures would have been obliterated leaving no evidence of such sorting. The systematic upward decrease in Cr content of magnetite in the MML observed by Cawthorn and McCarthy (1980) however, is unlikely to have been produced through a process of density sorting as density sorting would not sort minerals according to composition.

1.4. Summary

Fe-Ti magnetitite layers are an integral part of LMI. It is therefore necessary to study these geological entities in order to expand our understanding of processes which led to the crystallization of LMI. Mechanisms including crystal settling, magma addition, rhythmic layering, liquid immiscibility, change in oxygen fugacity, diffusion controlled bottom crystallization, pressure change, double-diffusive layering and magma currents have been proposed as the driving factors behind the genesis of Fe-Ti magnetite concentrations observed in LMI. However, many of the models have short-comings as has been discussed in the preceding paragraphs and further highlighted by several authors (Harney and Von

Gruenewaldt, 1995; Cawthorn et al., 2005; Cawthorn and Ashwal, 2009). This study aims to provide a more comprehensive understanding of the geochemistry of Fe-Ti magnetite in magnetitite layers of the BC.

Chapter 2 – Field Relations

The UZ contains many magnetitite layers. There are only a few localities where there are well exposed outcrops of the MML. The MML is commonly traced along strike using magnetite rubble and therefore detailed vertical sampling is rarely possible. Klemm et al. (1985) collected samples of the magnetitite layers including the MML along traverses in the Roossenekal area (Fig. 1.1) in the eastern limb in their study on the magnetitite layers but exact locations are not recorded. A number of localities were investigated in the current study. The field relations are described below and the samples collected described in Chapter 3.

2.1. Sampled Locations

2.1.1. Magnet Heights River Section

The 2 m thick MML is well exposed along a ~100 m river section in the Magnet Heights area (Figs. 1.1, 2.1.1A). This area has previously been documented by Cawthorn and McCarthy (1980, 1981). Sharp, planar contacts characterize the basal contact of the MML with the underlying mottled anorthosite (Fig. 2.1.1B). The top contact of the MML with the overlying anorthosite is, however, gradational. Anorthosite fragments are trapped and concentrated towards the base of the MML (Fig. 2.1.1C). An intermediate zone termed the feldspar parting is distinguished by the presence of minor cumulus plagioclase. In the exposed river section the feldspar parting is ~ 10 cm thick and about 1 m above the base (Fig. 2.1.1D). At one place the feldspar parting is absent and truncated by a dome structure which interrupts the planar nature of the MML (Figs. 2.1.1E, F). Associated with the dome structures, are xenoliths of basalt enclosed in the underlying mottled anorthosite (Figs. 2.1.1E, G). The overlying anorthosite to the MML is about 2 m thick. This anorthosite is overlain by magnetitite layer 1 which is 30 cm thick and shows similar features to the MML. The bottom contact of layer 1 with the underlying anorthosite is sharp whereas the upper contact grades into the overlying anorthosite (Fig. 2.1.1H). The feldspar crystals in layer 1 show a preferred orientation with the long axis of the feldspars aligned parallel to the layering (Fig, 2.1.1I). Layer 1 is at one locality underlain by an impermeable basalt xenolith 11 m in length (Fig. 2.1.1J).


A

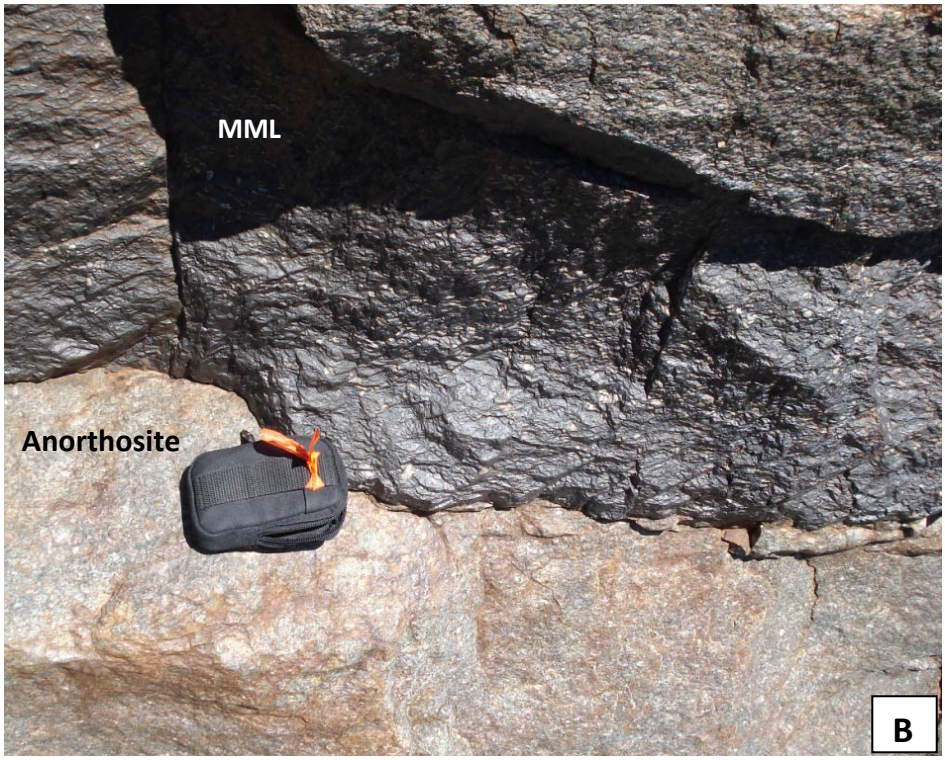
MML
Anorthosite
B

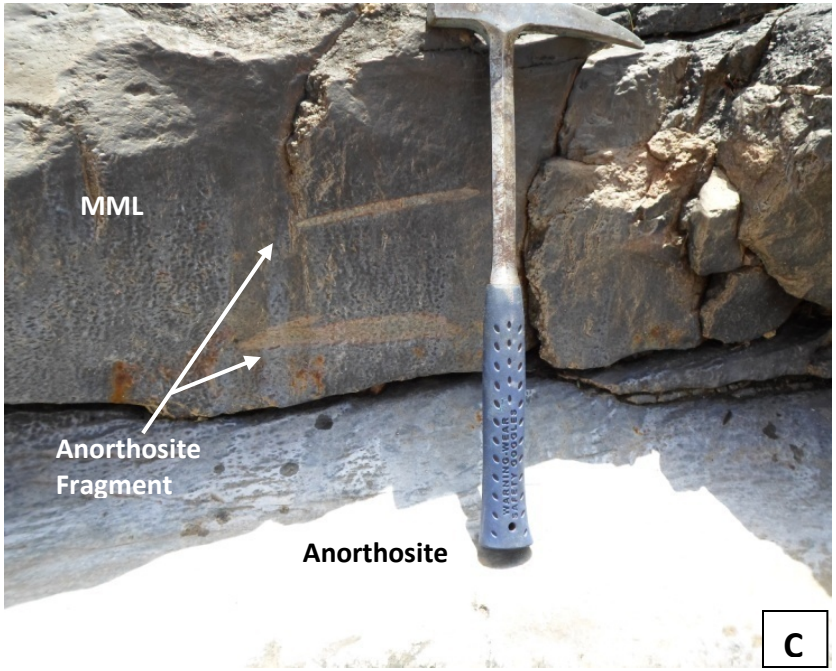
MML
Anorthosite
Fragment
Anorthosite
C

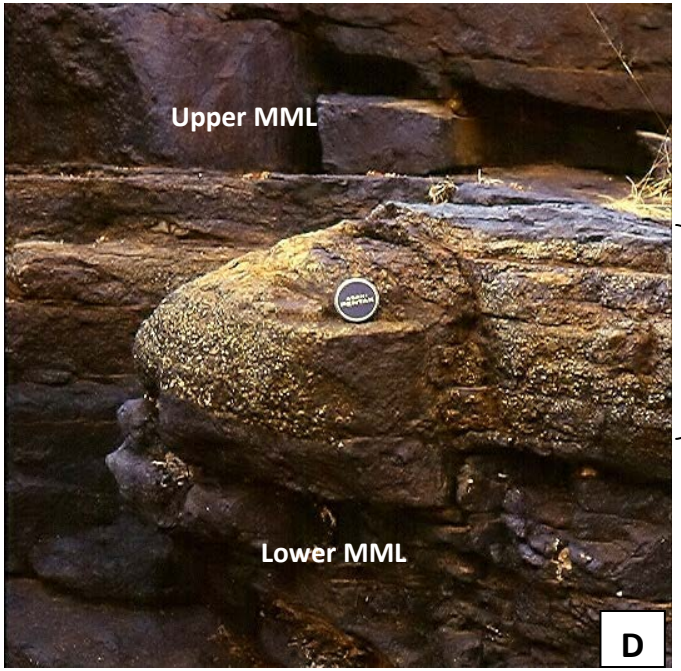
Upper MML
Feldspar
parting
Lower MML
D


Basalt
fragment
E


Truncated
Feldspar parting
F

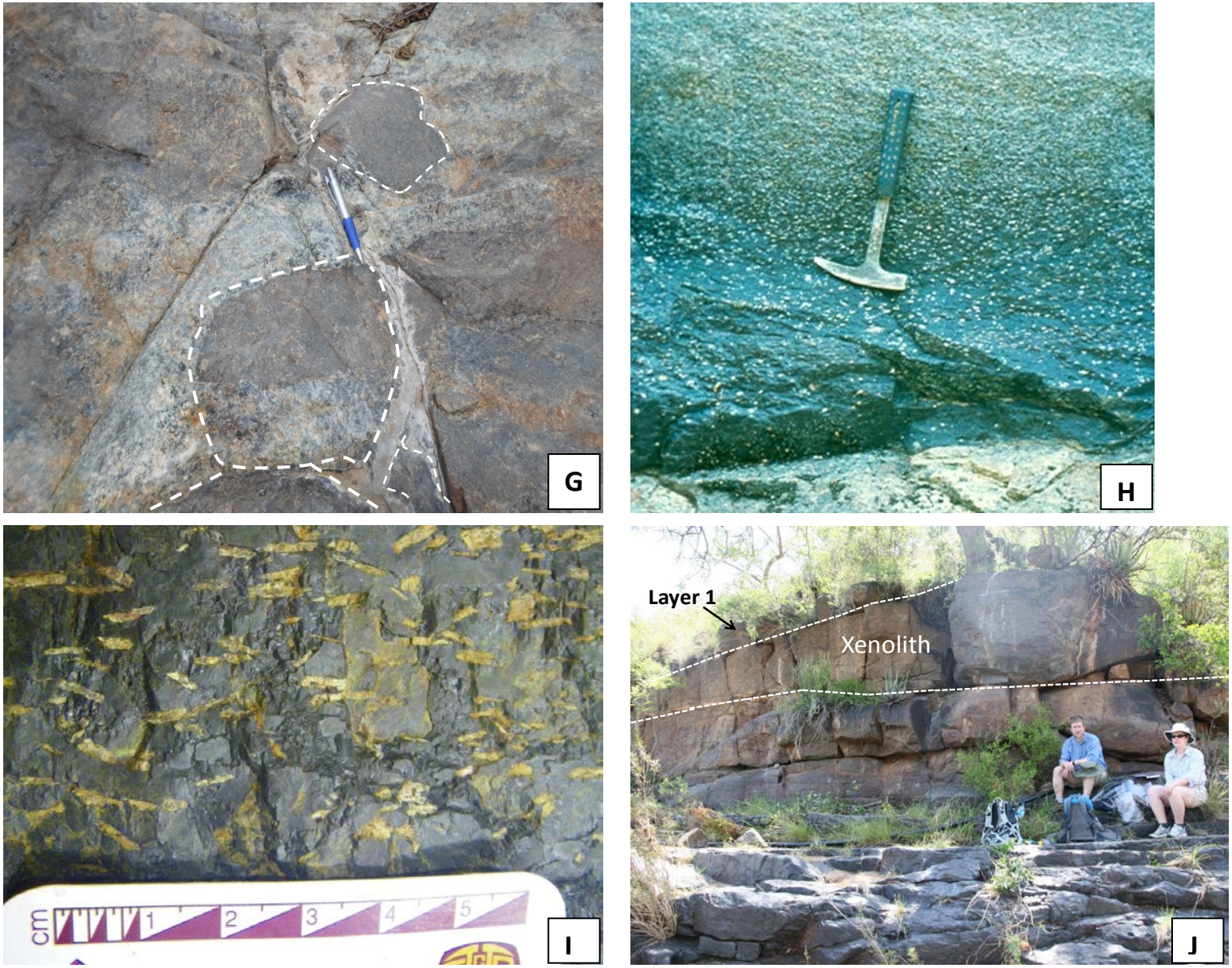

Fig. 2.1.1. Field observations areas sampled in Magnet Heights (Fig 1.1). (A) Overview Magnet Heights river section. (B) Sharp lower contact of MML with underlying anorthosite. (C) Anorthosite fragments trapped in MML. (D) Cumulus feldspar crystals in Feldspar parting. (E, F) Dome structure. (G) Basalt fragments associated with footwall anorthosite of the dome structure. (H) Sharp lower contact and gradational upper contact of layer 1with anorthorsite. (I). Planar oriented feldspar crystals in layer 1. (J) Basalt xenolith underlying layer 1.

2.1.2. Roossenekal

Magnetitite bifurcations similar to the chromitite bifurcations observed in Dwars River were present on Swartkop farm, north of Roossenekal but have since been mined out. These were originally documented by Hammerbeck (1970). The total thickness of all the sub-layers is somewhat less than the typical 2 m thickness of the MML, but is rather variable. The upper most sub-layer (sub-layer 4) merges with layer 1 (Fig. 2.1.2A). Both the upper and lower contacts of the sub-layers with the magnetite-rich anorthosite separating the sub-layers are sharp as those observed at the base of the MML in Magnet Heights. The thickness of the magnetitite sub-layers are laterally variable ranging from 18-26 cm at sampling localities. Magnetite bifurcations can also observed on a smaller scale from several samples collected from the Evraz Mapochs mine, north of Roossenekal (Figs. 2.1.2C, D).

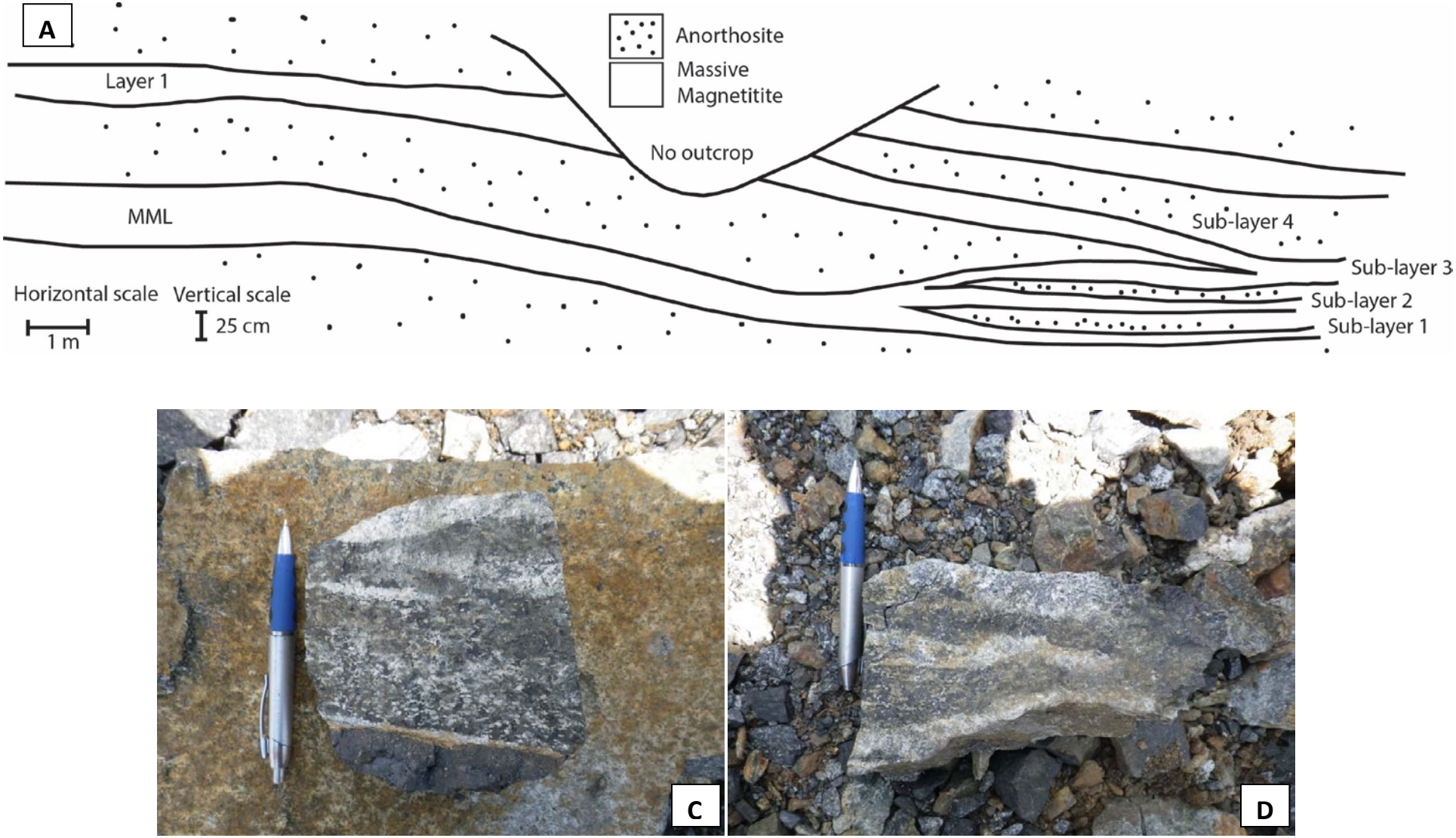

Fig. 2.1.2. Magnetitite bifurcations north of Roossenekal (Fig. 1.1). (A) Sketch of MML spitting into three sub-layers and merging with layer 1. (B, C) Small scale magnetite bifurcation in samples from Evraz Maphochs mine in Roossenekal (Fig. 1.1).

2.2. Relevant Data from other Areas

Some areas visited provide observation on features that may provide insight into the processes operating in the BC. They are documented here and included in later discussion but no samples were collected for analytical work. In a section near the Magnet Heights dam several magnetitite layers as well as associated magnetite plugs can be observed, however, only the MML and layer 1 can be identified. The exposed section of the MML shows it is underlain by highly weathered anorthosite whereas the overlying anorthosite has been completely eroded away by surface processes (Fig. 2.2A). The feldspar parting in this section has been removed by surface processes leaving a gap midway within the MML, however the feldspar parting is still present in the succession (Fig. 2.2B). One uncommon observation in this section is the presence of a near vertical dipping magnetitite layer (Fig. 2.2C). The orientation of plagioclase grains parallel to the layer, may suggest that this layer was initially horizontal and has now been rotated to its current position and is not a dyke or discordant body. Based on the magnetitite layer's V_2O_5 content it has been correlated with lower layer -1 (Cawthorn, pers. comm.)

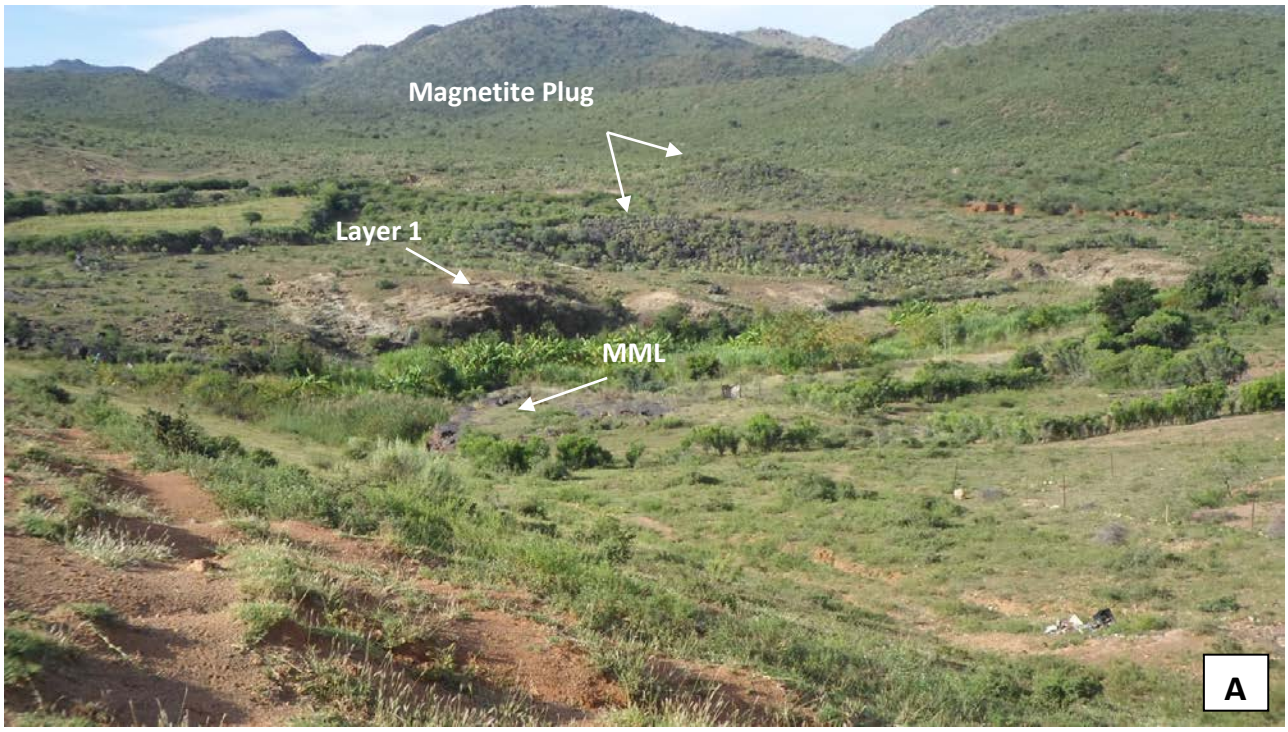

Fig. 2.2. Field observations areas not sampled in Magnet Heights area (Fig. 1.1). (A) Overview Magnet Heights dam section. (B) Exposed MML in the Magnet Heights dam section. (C) Vertical dipping lower magnetitite layer.

Lower layer -3 (Fig. 2.3A) is exposed a few kilometres east from the Magnet Heights dam. This layer contains variable concentrations of plagioclase grains. A planar feldspar fabric is present in the lower layer (Fig. 2.3B). The layer is not entirely planar but changes in dip across the outcrop creating a concave, channel-like structure (Fig. 2.4.). Exposure of the footwall is highly weathered and the rocks are so unlayered, that it is impossible to determine if this structure is erosive and discordant or whether the entire sequence has been rotated as in Figure 2.2C.

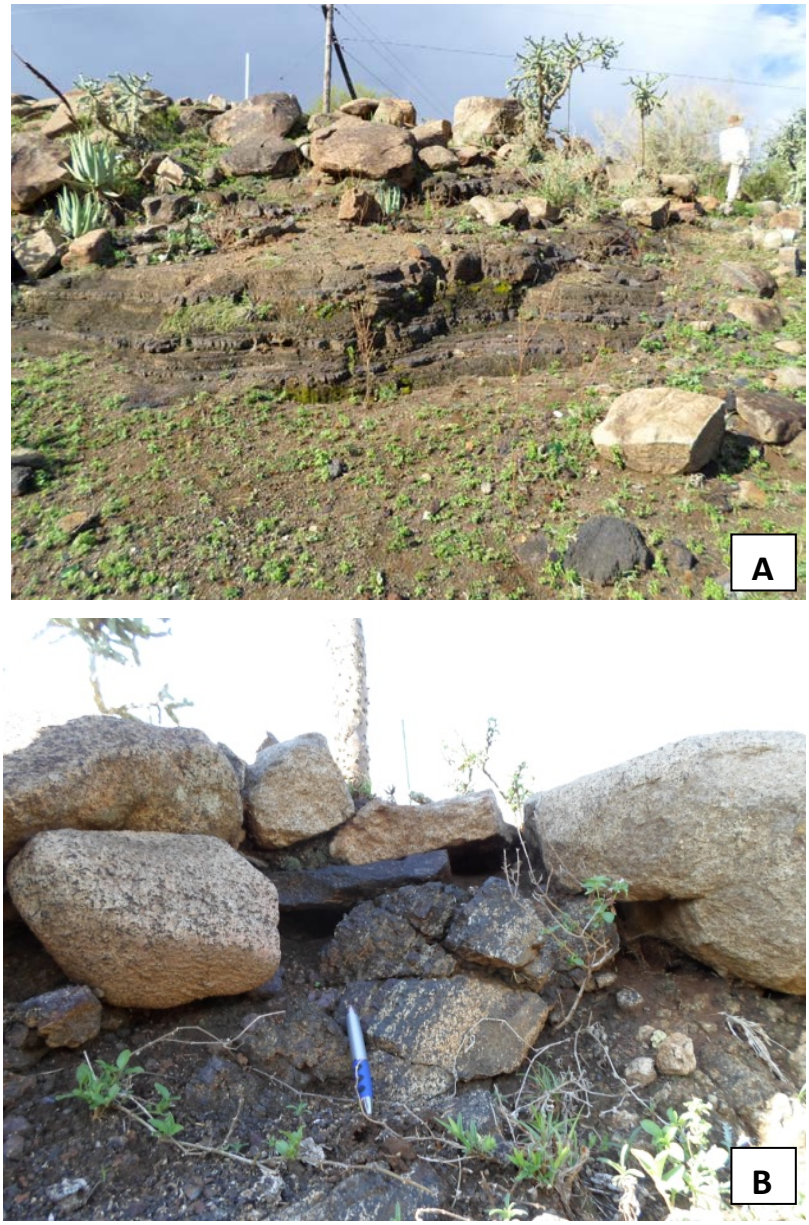

Fig.2.3. Lower layer in the Magnet Heights area (Fig. 1.1). (A) Lower magnetitite layer -3. (B) Feldspar fabric in magnetitite layer showing evidence for rotation of layer.

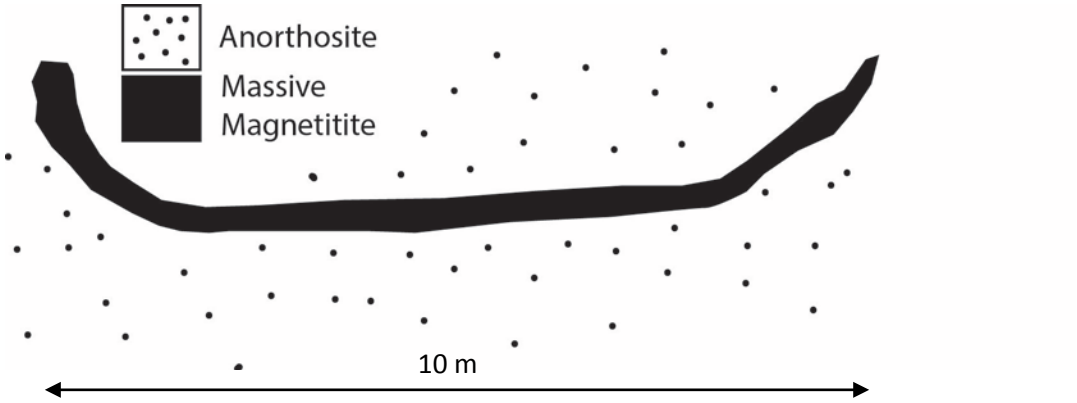

Fig. 2.4. Schematic diagram showing variation of dip of lower magnetitite layer -3 shown in Figure 2.3 creating a channel shape.

Chapter 3 – Sampling

The current study is the sum of a number of previously incomplete projects investigating the magnetitite layers of the UZ and additional material has been collected for this study. A number of data sets of analyses of magnetite mineral separates including data from previous projects, a few of which has been previously published, are used in the project. The source of previously published data is listed in Table 3.1 and it includes data from Magnet Heights (Cawthorn, 1994; Cawthorn and Street, 1994); Bierkraal drill cores, north of Rustenburg (BK1 and BK3) (Tegner et al., 2006); a 6 m drill core intersecting a magnetite-rich sequence from UCAR mine (east of Brits) (Cawthorn and McCarthy, 1981) and electron microprobe data published by Ashwal et al. (2005) of magnetite grains from the Bellevue drill core (BV-1) in the northern limb which intersects the entire UZ and half of the MZ. Unpublished Cr data from BK1 and BK3 drill cores collected by Cawthorn and McCarthy (1980, 1981) is included. Previously analyzed samples, but not published data, of the MML from the Magnet Heights river section area were acquired by Cawthorn and McCarthy (1980, 1981), McCarthy and Cawthorn (1983) and Cawthorn (1994) as part their research on the MML. Data of magnetite separates from layer 1 in Magnet Heights were collected by Cawthorn and Street (1994). Additional material collected for this study includes new vertical and lateral profiles taken through the MML in Magnet Heights. Along with samples taken of the MML, layer 1 was also sampled in Magnet Heights. Samples were also collected from the MML and sub-layers in vicinity of bifurcations at Swartkop, north of Roossenekal. The samples collected in the current study have been categorized as follows and the samples are listed in Table 3.2.

3.1. Vertical Sections through Main Magnetitite Layer

Four vertical profiles (1-4) with a total of 59 samples were taken through the bottom half of the MML at ~10 cm intervals up to and including the feldspar parting. The lateral spacing of the profiles varies, covering a distance of ~35 m (Fig. 3.1).

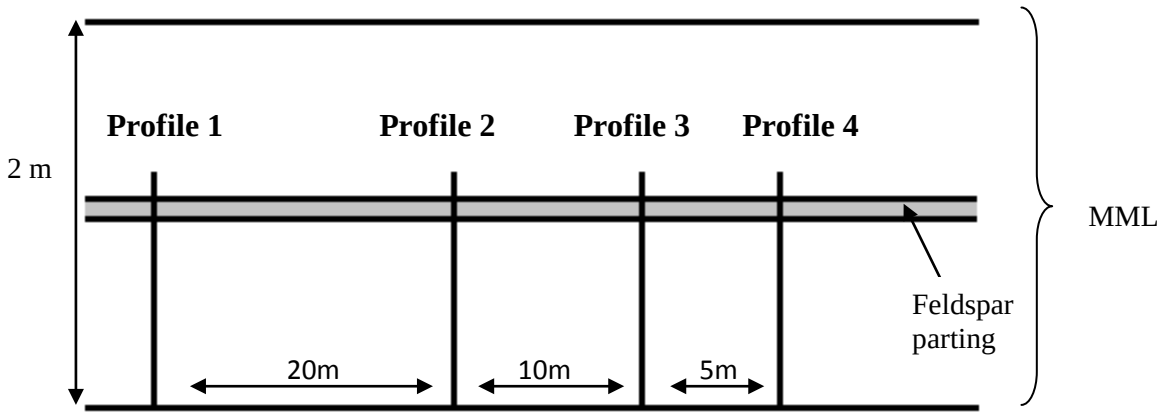

Fig. 3.1. Cross section sketch of profiles (1-4) collected through the bottom half of the MML in Magnet Heights.

3.2. Vertical Sections through Feldspar Parting of Main Magnetitite Layer

Seven detailed profiles were taken specifically to investigate the feldspar parting in the MML. Vertical profile P comprises seven samples, three (P1-P3) collected below the feldspar parting, one (P4) in the feldspar parting and three (P5-P7) taken above the feldspar parting (Fig. 3.2A). Six detailed vertical profiles (D1-D6) with a total of 42 samples were taken through the feldspar parting. The profiles are variably laterally spaced covering ~100 m in the Magnet Heights river section (Fig. 3.2B). In all six vertical profiles, one sample (A) was taken below the feldspar parting, one (B) at the base of the feldspar parting, three within the feldspar parting (C, D and E), one (F) at the top of the feldspar parting and, one above the feldspar parting (G).

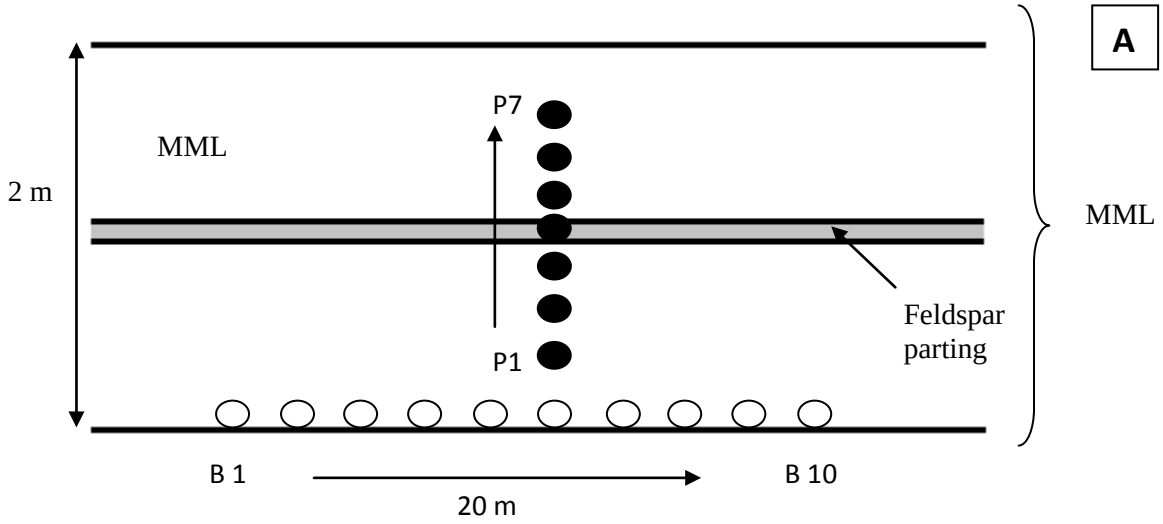

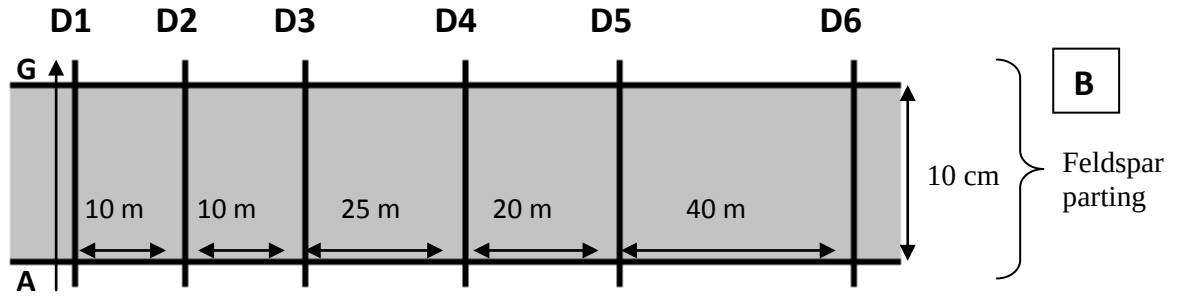

Fig. 3.2. Cross section sketch of profiles through feldspar parting of the MML (A) Profile along the base B1-B10 (open circles) and profile through feldspar parting P1-P7. (B) Detailed profiles (D1-D6) through the feldspar parting.

3.3. Vertical Sections through Main Magnetitite Layer at the Dome Structure

Another four vertical profiles, comprising 85 samples, through the MML (G, H, I and J) were collected where the dome structure truncates the feldspar parting. The profiles are variably laterally spaced covering a distance of ~1.6 m. Vertical sampling in each profile is ~5 cm (Fig. 3.3).

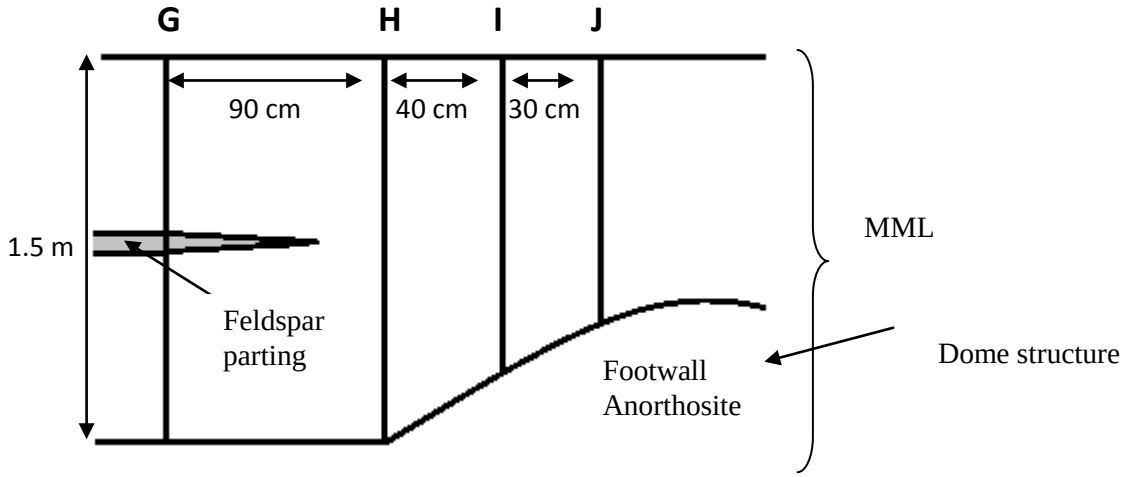

Fig. 3.3. Cross section sketch of Profiles G-J collected above the dome structure.

3.4. Lateral Sampling along Base of Main Magnetitite Layer

Nineteen samples (CM1-19) (Cawthorn, 1994) with a lateral spacing of ~10 m were collected along the base of the MML. The samples were taken on both sides of the river and cover a lateral distance of ~100 m. A more detailed lateral profile along the base of the MML was taken with ten samples B1-B10 (Fig. 3.2A) spaced at ~2 m covering a distance of ~20m. Sample B6 marks the base of vertical profile (P) taken through the feldspar parting. Three larger vertically oriented samples about 3 cm vertical length (B2, B7 and B9) were split in half obtaining a top piece (a) and a bottom piece (b) to evaluate small scale vertical Cr gradients at the base.

3.5. Magnetitite Bifurcations

Vertical profiles were taken in the vicinity of the MML bifurcations (Fig. 2.1.2A). Three vertical profiles (SL1-SL3) with a total of 33 samples were taken through the MML. Two more profiles (SL4 and SL5) with a total number of 11 samples were collected from midway, because the lower section was too weathered, to the top of the MML adjacent to the magnetitite sub-layers. Five vertical profiles (SL5-SL10) with a total of 20 samples were taken through magnetitite sub-layers 2-4. Samples (M1-M14) were collected along the base of the MML and sub-layer 1 at ~1 m spacing. Samples with disseminated magnetite (M18-M28) were collected from the magnetite-rich anorthosite separating the magnetitite sub-layers above profiles SL4, SL6 and SL7 (Fig. 3.4). Sub-layer 1 could not be sampled vertically because it was too weathered

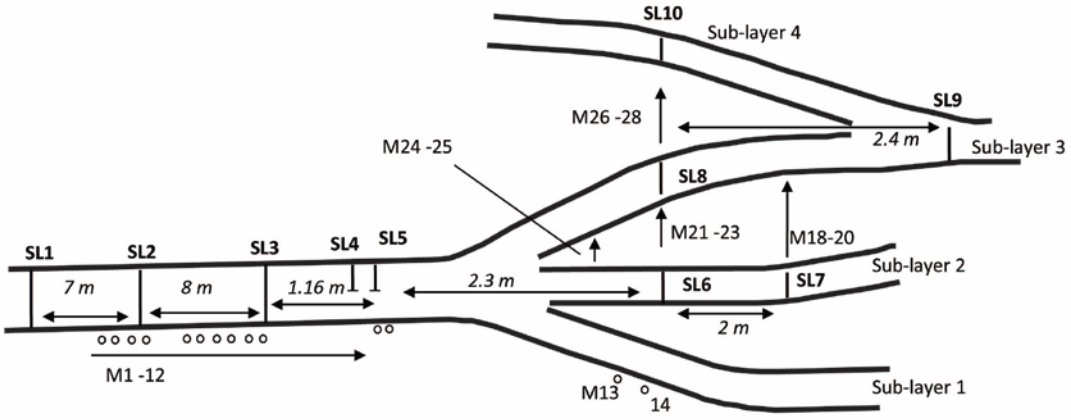

Fig.3.4. Cross section sketch profiles SL1-SL10 collected in vicinity of MML bifurcations north of Roossenekal.

3.6.Vertical Sections through Layer 1

A total of 96 samples (Cawthorn and Street, 1994) were collected from nine vertical profiles (L1/1-L1/9) through layer 1 in the Magnet Heights river section (Fig. 3.5). Sampling was done at 1 cm vertical sampling from the base to the top of layer 1. Three of the profiles (L1/1-L1/3) were taken in the normal section where layer 1 directly overlies anorthosite. The remaining seven profiles (L1/4-L1/9) were taken at ~1 m spacing where layer 1 directly overlies an impermeable basalt xenolith.

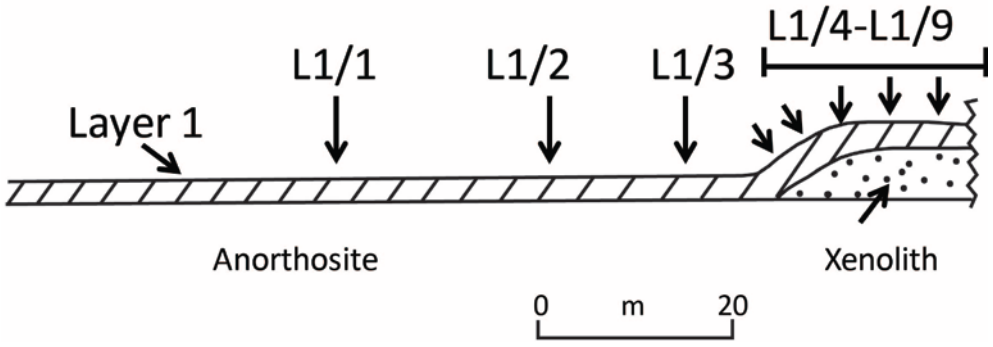

Fig. 3.5. Cross section sketch of vertical profiles through layer 1 in Magnet Heights. Profiles L1/1-L1/3 taken over the normal section. Profiles L1/ 4-L1/9 taken above xenolith.

3.7. Bierkraal (BK1 and BK3)

Bierkraal drill cores BK 1 and BK 3 were drilled through the UZ in the western limb by the Council for Geosciences. Magnetite mineral separates have been obtained from BK 1 and BK 3. A total number of 164 samples were collected from BK 1 with 28 collected from massive magnetitite layers and 136 disseminated magnetite from host lithology. A total of 126 samples were collected from BK 3 with 13 from massive magnetitite layers and 113 disseminated magnetite from host lithology.

3.8. Sample Processing

Samples were crushed and screened to 250µ (60 mesh) and magnetically separated by hand magnet. Samples P4, P5 and B2 were crushed and screened to three sizes (100µ, 250µ and 400µ) to study the effects of different crushing sizes on the analyses. The magnetite separates were milled to powder and pressed into pellets. Crushing to these sizes ensures that the coarse ilmenite, presumed to be primary, is removed but the exsolution products are carried into the magnetite separates.

Table 3.1. Previously Published Data included.

	Source	Technique
BK1 and BK3	Tegner et al. (2006)	Mineral separates analysed by XRF
BV-1	Ashwal et al. (2005)	Mineral grains analysed by electron microprobe
UCAR	Cawthron and McCarthy (1981)	Mineral separates analysed by XRF
Magnet Heights	Cawthron and McCarthy (1981); Cawthorn (1994); Cawthorn and Street (1994)	Mineral separates analysed by XRF

Table 3.2. List of Profiles Collected.

Vertical Sections through MML	Vertical Sections through Felspar parting	Lateral profile along base of MML	layer 1	Magnetitite Bifurcation
G	D1 A-G	B1-B10	L1/1-9	SL1/A-T
H	D2 A-G	CM 1-CM 19*		SL2/A-H
I	D3 A-G			SL3/A-E
J	D4 A-G			SL4/A-E
1	D5 A-G			SL5/A-5
2	D6 A-G			SL6/A-D
3	P1-P7			SL7/A-D
4				SL8/A-C
				SL9/A-D
				SL10/A-E
				M1-M28

Previously published data by Cawthorn (1994)

Chapter 4 – Magnetite Geochemistry

The focus of this study is the trace and minor elements of magnetite separates, primarily from the massive magnetitite layers. For some previous sets of samples only Cr content was reported. The Cr, V, TiO_2, Al_2O_3, MgO, Ni and Cu contents of the magnetite separates collected for this study are listed in Appendix C. The following results presented are chiefly focussed on Cr as this highly compatible trace element in magnetite with D>200 (Irving, 1978) is sensitive to differentiation processes during the crystallization of magnetitite (Cawthorn and McCarthy, 1980; 1981). Vanadium also has a high coefficient of D=20-25 (Irving, 1978) for magnetite; however shows little variation and thus will not be discussed in much detail. It should be noted importantly that the analyses of the magnetite separates include components of exsolved phases due to subsolidus exsolution of the magnetite grains (Buddington and Lindsley, 1964; Willemse, 1969; Von Gruenewaldt et al., 1985; Reynolds, 1985b; Butcher and Merkle 1987; Klemm et al., 1985).

4.1. Analytical Techniques

As this study focuses primarily on Cr, the detection limits and precision of electron microprobe (0.01-0.02 Cr_2O_3 wt%) are inadequate and thus X-ray fluorescence (XRF) was used. Elements analyzed for are Cr, V, Cu, Ni, TiO_2, Al_2O_3, MgO and SiO_2. SiO_2 was analyzed to test the purity of the magnetite separates. Standards used for calibration are listed in Appendix A.

4.1.1. Crushing Size

The size of the exsolution phases within magnetite grains are variable ranging from 5 to 100µm (Von Gruenewaldt et al., 1985). The variable size of the exsolution phases may present a problem when determining the size of separation used for the magnetite separates. Crushing to too coarse a size may result in some composite particles with both magnetite and other grains (silicates and primary ilmenite) being produced which would still be collected during the magnetic separation. In contrast, crushing to a finer size is likely to exclude the exsolution products. The presence or absence of exsolved phases within the magnetite separates is most likely to have an effect on MgO, TiO_2 and Al_2O_3 as these elements are the

major constituents of the exsolution phases (Von Gruenewaldt et al., 1985; Reynolds, 1985b; Butcher and Merkle, 1987).

Electron microbe analyses of individual magnetite grains from the UZ have revealed heterogeneity within individual grains. Von Gruenewaldt et al. (1985) and Butcher and Merkle (1987) noted compositional heterogeneity in the form of peaks and troughs in Mg and Al content along traverses through individual magnetite grains. Peak Mg and Al concentrations were found to be coincident with the positions of exsolved phases. Von Gruenewaldt et al. (1985) observed that within a single magnetite grain, the Mg and Al of magnetite located between spinel exsolution phases is lower compared to magnetite located in spinel-free areas. The compositional heterogeneity observed in individual grains is suggested to be a result of the exsolved phases depleting host magnetite of Al and Mg (Von Gruenewaldt et al., 1985; Butcher and Merkle, 1987)

Table 4.1 shows that the analyses of different crushing sizes for samples P4, P5 and B2 all show similar compositions. The highest relative standard deviation for major elements TiO_2, Al_2O_3, MgO and SiO_2 are 5.20; 25.47; 17.64 and 47.82 % respectively. The highest relative standard deviation recorded for V and Cr are 4.53 % (B2) and 4.72 % (P5) respectively. SiO_2 shows the highest relative standard deviation, however, there appears to be no correlation between crushing size and the composition of magnetite mineral separates. Hence it is concluded that the method used here gives reliable compositions for the primary magnetite and are not influenced by variable exsolution processes or inclusions of significant silicate material.

Table 4.1. Analyses of Different Separation Size (100µ, 250µ and 400µ) of Magnetite Mineral Separates

Sample	V wt%	TiO_2 wt%	Cr ppm	Cu ppm	Ni ppm	Al_2O_3 wt%	MgO wt%	SiO_2 wt%
B2 (a)	1.18	12.30	12896	BD	641	3.89	1.93	0.85
B2 (b)	1.08	11.55	12577	179	617	4.15	2.20	1.79
B2 (c)	1.15	11.95	12389	BD	665	3.97	2.09	0.82
Avg	**1.14**	**11.93**	**12621**		**641**	**4.00**	**2.07**	**1.15**
Stdev	**0.05**	**0.38**	**256**		**24**	**0.13**	**0.14**	**0.55**
Rel. Stdev %	**4.53**	**3.14**	**2.03**		**3.74**	**3.33**	**6.55**	**47.82**
P 4 (a)	1.12	11.25	1393	585	509	4.15	1.64	3.46
P 4 (b)	1.05	11.97	1310	564	515	2.66	1.48	2.03
P 4 (c)	1.07	10.80	1303	556	524	4.44	2.07	4.21
Avg	**1.08**	**11.34**	**1335**	**568**	**516**	**3.75**	**1.73**	**3.23**
Stdev	**0.04**	**0.59**	**50**	**15**	**8**	**0.96**	**0.31**	**1.11**
Rel. Stdev %	**3.34**	**5.20**	**3.75**	**2.64**	**1.46**	**25.47**	**17.64**	**34.25**
P 5 (a)	1.24	13.04	1453	149	309	3.72	0.94	0.97
P 5 (b)	1.24	12.83	1587	159	314	3.85	0.84	0.85
P 5 (c)	1.26	13.20	1479	140	310	3.29	0.91	0.53
Avg	**1.25**	**13.02**	**1506**	**149**	**311**	**3.62**	**0.90**	**0.78**
Stdev	**0.01**	**0.19**	**71**	**10**	**3**	**0.29**	**0.05**	**0.23**
Rel. Stdev %	**1.05**	**1.42**	**4.72**	**6.36**	**0.85**	**8.10**	**5.72**	**29.04**

(a) = 100µ (b) = 250µ (c) = 400µ BD = Below detection.

4.1.2. Magnetite Mineral Separation

Magnetite can form in a variety of conditions including crystallization from a silicate melt; hydrothermal fluids or sulfide liquids (Naldrett, 1969; Von Gruenewaldt, 1976; Dare et al., 2012; Nadoll et al., 2014; Dare et al., 2014). In order to investigate the differentiation processes resulting in the crystallization of the UZ, it is necessary to ensure that the magnetite separates analyzed are not a mixture of magnetite grains from different environments as this would lead to misinterpretation of the results. The environments in which magnetite can crystallize are reflected in the composition of the magnetite. Therefore, the magnetite composition provides a fingerprint of the environment in which magnetite may have formed (Dare et al., 2014; Nadoll et al., 2014).

Harney and Merkle (1992) observed minor amount of secondary magnetite in a sulfide assemblage above the MML commonly occurring in pockets or as veinlets in Ti-magnetite crystals. The secondary magnetite was found to contain no detectable amounts of Ti, V and Cr. From textural relations and the amount of secondary magnetite present in the sulfide assemblage, Harney and Merkle (1992) concluded that the secondary magnetite did not crystallize directly from a sulfide or silicate melt but rather crystallized from late-stage Fe-enriched hydrothermal fluids. Von Gruenewaldt et al. (1985) noted fracture fillings of magnetite in the massive magnetitite layers of the UZ. The fillings were found to be pure, containing 96 wt% Fe, low V content (0.07 wt%) and no detectable Cr and were suggested to be of hydrothermal origin. Furthermore, magnetite crystallized from hydrothermal fluids has been shown to contain low concentrations Ti (<2 wt%) and Al (<1 wt%) (Dare et al., 2014). Von Gruenewaldt (1976) suggested magnetite observed in association with sulfides in the UZ crystallized from immiscible sulfide liquids which were responsible for the formation of sulfides present in the UZ. Magnetite crystallized from sulfide melts has been shown to contain <2 wt% Ti and no detectable amounts of Cr (Dare et al., 2014). The magnetite separates collected from Magnet Heights, Swartkop, BK and UCAR drill cores all contain trace amounts of Cr therefore, it can be concluded that the magnetite separates studied here represent magnetite crystallized directly from the silicate magma.

Impurities intimately attached to magnetite grains in the massive magnetitite layers may have been incorporated into the magmatic fraction during magnetic separation. Subordinate feldspar has been documented to occur in magnetitite layers (Butcher and Merkle, 1987; Reynolds, 1985b). Magnetite separates from samples collected from profiles through the MML all show low SiO_2 content ranging between 0-4 wt%. Klemm et al. (1985) attributed the SiO_2 content (up to 6 wt%) of magnetite separates from magnetitite layers to submicroscopic inclusions of Fe-Al-Mg silicates. If submicroscopic inclusions of Fe-Al-Mg silicates (possibly plagioclase and pyroxene) are present, Al and Mg peaks along traverses through magnetite grains should not occur at the same place as plagioclase would show as peak in Al and pyroxene showing as a peak in Mg. However, Butcher and Merkle (1987) found peaks of Al and Mg to occur at the same point suggesting these anomalous peaks represent spinel and not silicate.

4.2. Vertical Sections through Main Magnetitite Layer

The vertical profiles (1-4) (Fig. 3.1) for Cr taken through the MML are presented in Figure 4.1. Three of the four profiles show an exponential upward depletion in Cr content from 12 000 ppm at the base to 700 ppm immediately above the feldspar parting. Between the basal sample and the second there is a decrease of ± 4 000 ppm, equivalent to a gradient of 400 ppm per vertical cm. Profile 1 however, shows an anomalously low basal value of 7 700 ppm. The second sample up has a value of 8 110 ppm, in the range for the second samples in the other three profiles, and thereafter shows a smooth gradual upward depletion in Cr content. Significant reversals in Cr content occur only in profile 1 above 70 cm (1 900-2 600 ppm) and profile 2 above 77 cm (1 300-2 400 ppm). However given the vertical accuracy with which samples could be collected on the outcrop, the two reversals could be considered to represent the same level and hence the same event. Both reversals occur within massive magnetite below the feldspar parting. All other elements, V, TiO_2, Al_2O_3, MgO, Ni and Cu show no systematic trends through the MML (Figs. 4.2A-F).

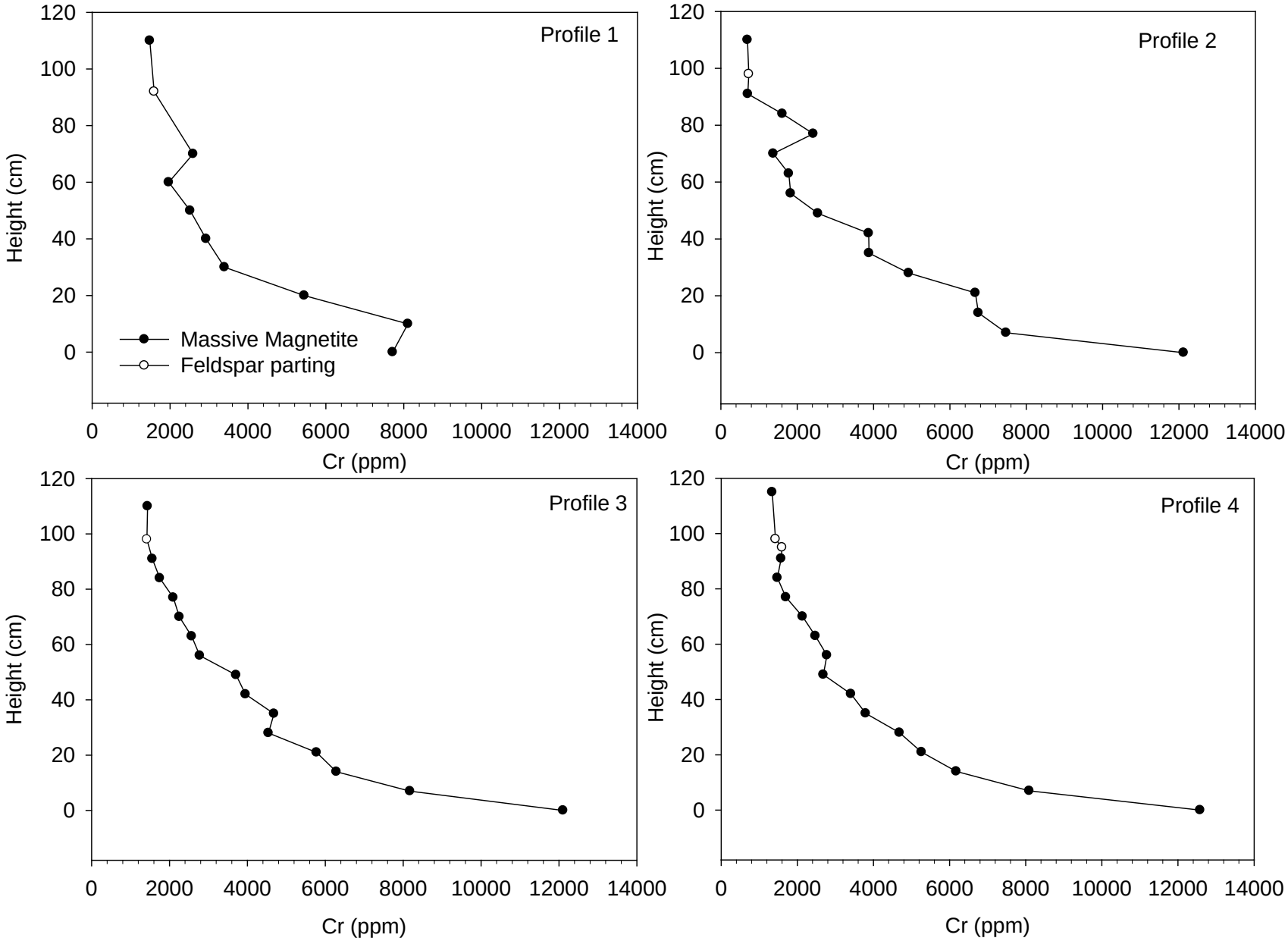

Fig. 4.1. Systematic upward decrease in Cr in magnetite for vertical profiles (1-4) through the MML.

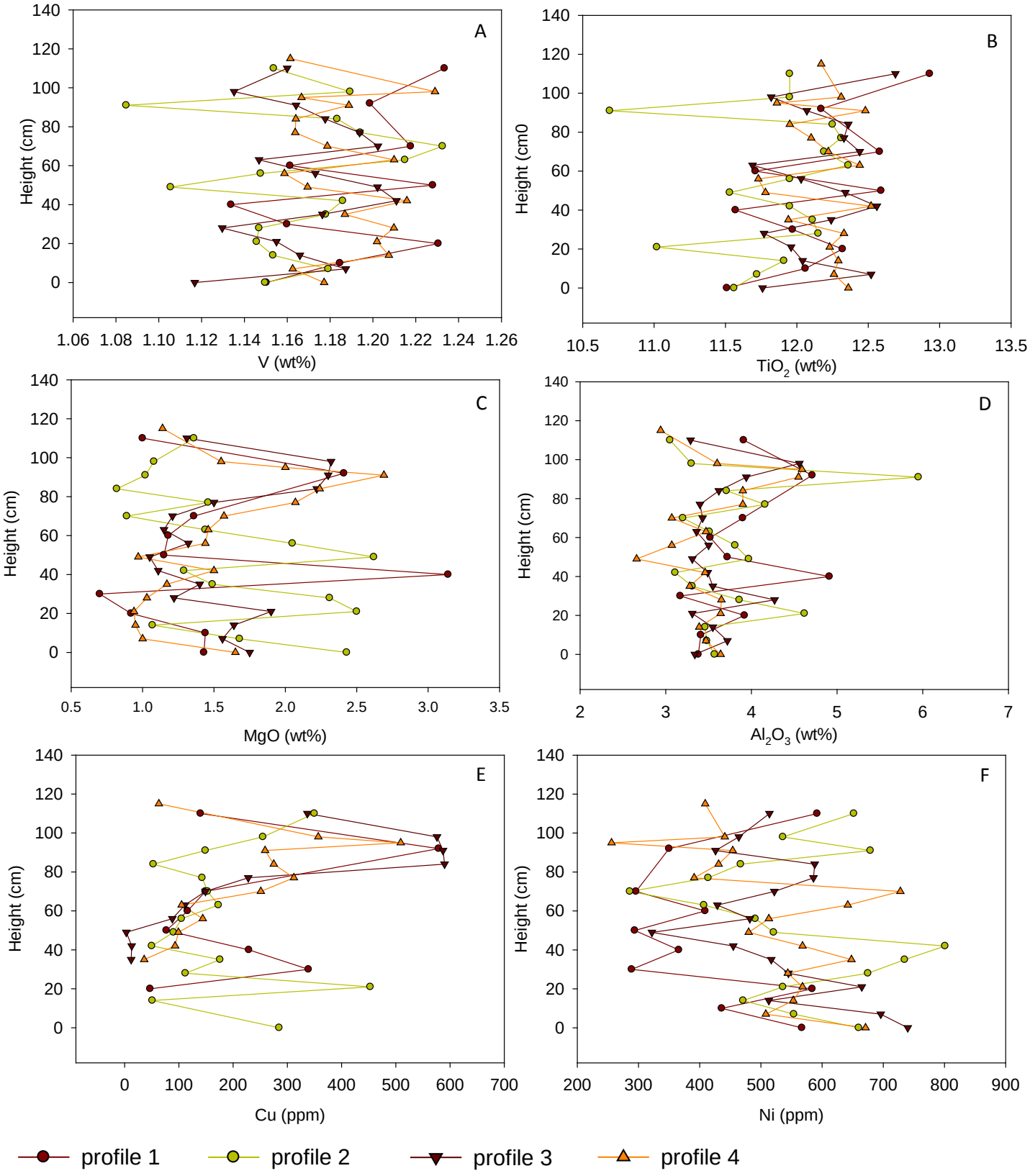

Fig. 4.2. Major and trace element concentrations in magnetite for profiles 1-4 through the MML.

4.3. Vertical Sections through Feldspar Parting of Main Magnetitite Layer

It could be suggested that the feldspar parting may represent the end of one cycle and that the overlying massive magnetite represents a second event. Profile P taken through the feldspar parting at relatively widely spaced vertical intervals shows a gradual decrease in Cr content. A trivial increase in Cr content (1 300-1 400 ppm) is noted above the feldspar parting and no other reversals are noted in this profile (Fig. 4.3A). Six more detailed vertical profiles (D1-D6) were then collected. Profiles D1-D6 typically show a slight upward but irregular decrease in Cr content through the feldspar parting (Fig. 4.3B). The range of variation of the samples collected within the feldspar parting is about 400 ppm.

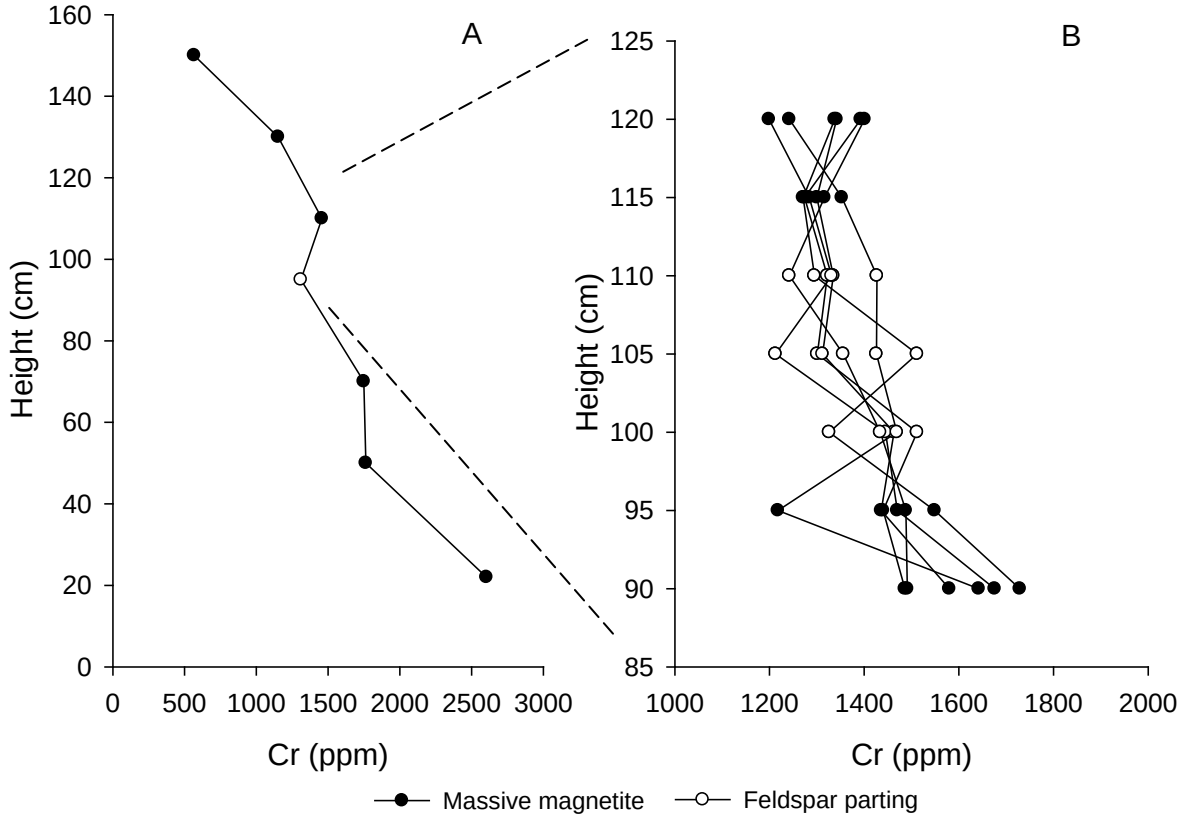

Fig. 4.3. Cr in magnetite for vertical profiles through the feldspar parting in the MML. (A) Widely spaced profile P. (B) Detailed profiles (D1-D6) through the feldspar parting. Note different horizontal and vertical scale.

4.4. Vertical Sections through Main Magnetitite Layer at Dome Structure

Figure 4.4 shows four profiles (G-J) in the vicinity of the dome structure which truncates the feldspar parting (Fig. 3.3). Only one profile (G) intersects the feldspar parting. Akin to profiles 1-4, profiles G-J typically show an exponential upward depletion in Cr content from 12 000 ppm at the base to 580 ppm at the top (Fig. 4.4). The upward depletion is however interrupted by reversals in Cr content in profiles G, H and I. Profile I shows the largest reversal in all of the profiles with one major reversal occurring above 25 cm (5 400-7 300 ppm) and another minor reversal above 70 cm (1 500-1 900 ppm). The reversals in profile G are minor occurring above 15 cm (5 500-5 800 ppm); 30 cm (2 700-3 000 ppm) and 110 cm (1 000-1 500 ppm). Only one reversal is noted in profile H occurring above 35 cm (4 300-5 100 ppm). The reversals occur within massive magnetite in the lower half of the MML with exception of one reversal in profile G (110 cm) which occurs in the upper half of the MML. There is no evidence for chemical significant breaks in Profiles H, I, and J at the levels where the feldspar parting might have been expected to occur. The Cr content decreases through the feldspar parting in profile G with no interruption to the trend.

Vanadium was analyzed for profile G and is constant, averaging 0.93 wt%, with the exception of one sample at the top of the profile showing an unusually high V content of 1.14 wt% (Fig. 4.5A). Other elements TiO_2, MgO, Al_2O_3, Ni and Cu were only analyzed for profile G and, show no systematic variation through the MML (Figs. 4.5B-F). Anomalous high and low values for a specific element do not correlate with anomalies recorded for other elements.

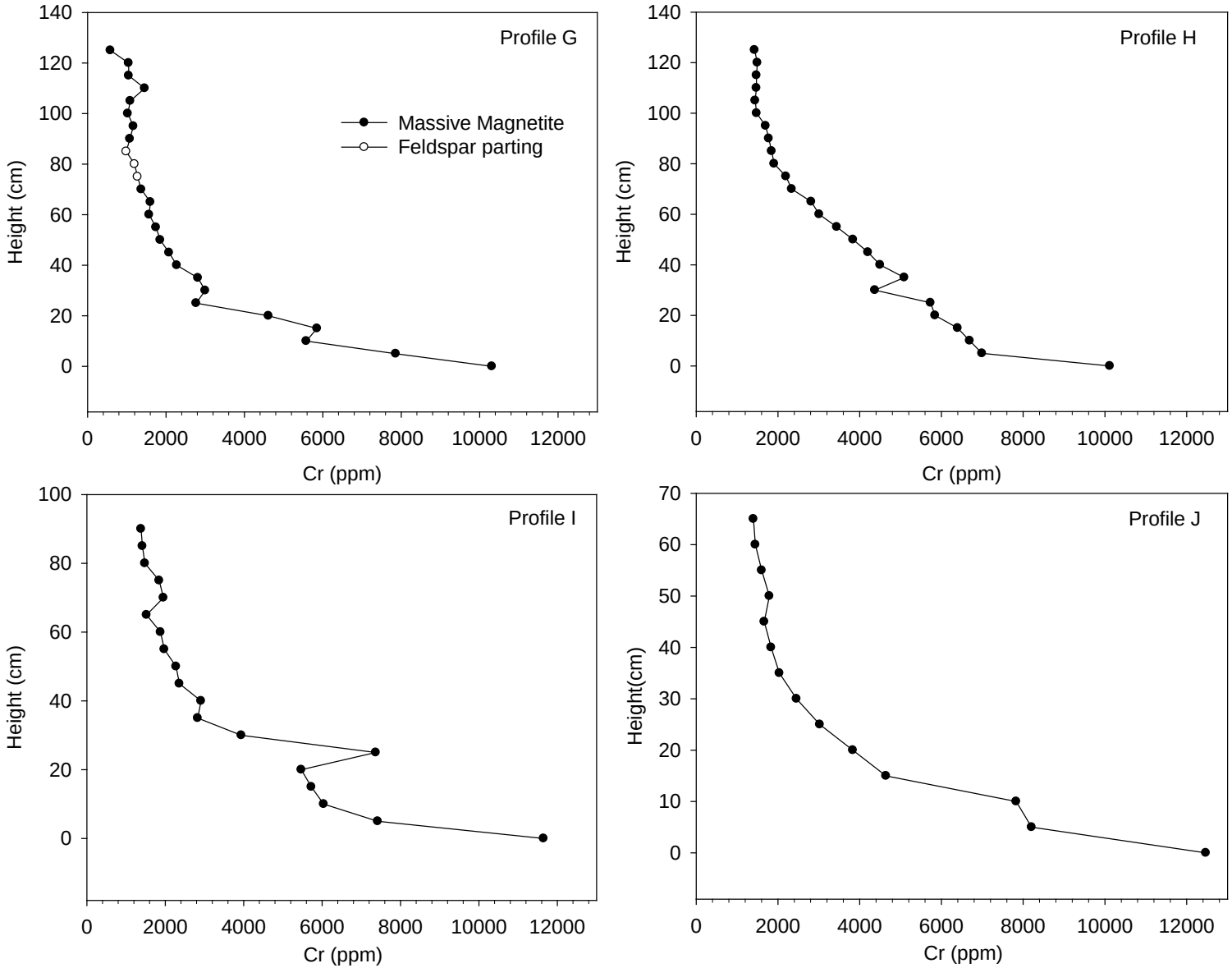

Fig. 4.4. Systematic upward decrease in Cr in magnetite for vertical profiles (G-J) through the MML near dome structure truncating feldspar parting. Only profile G intersects the feldspar parting.

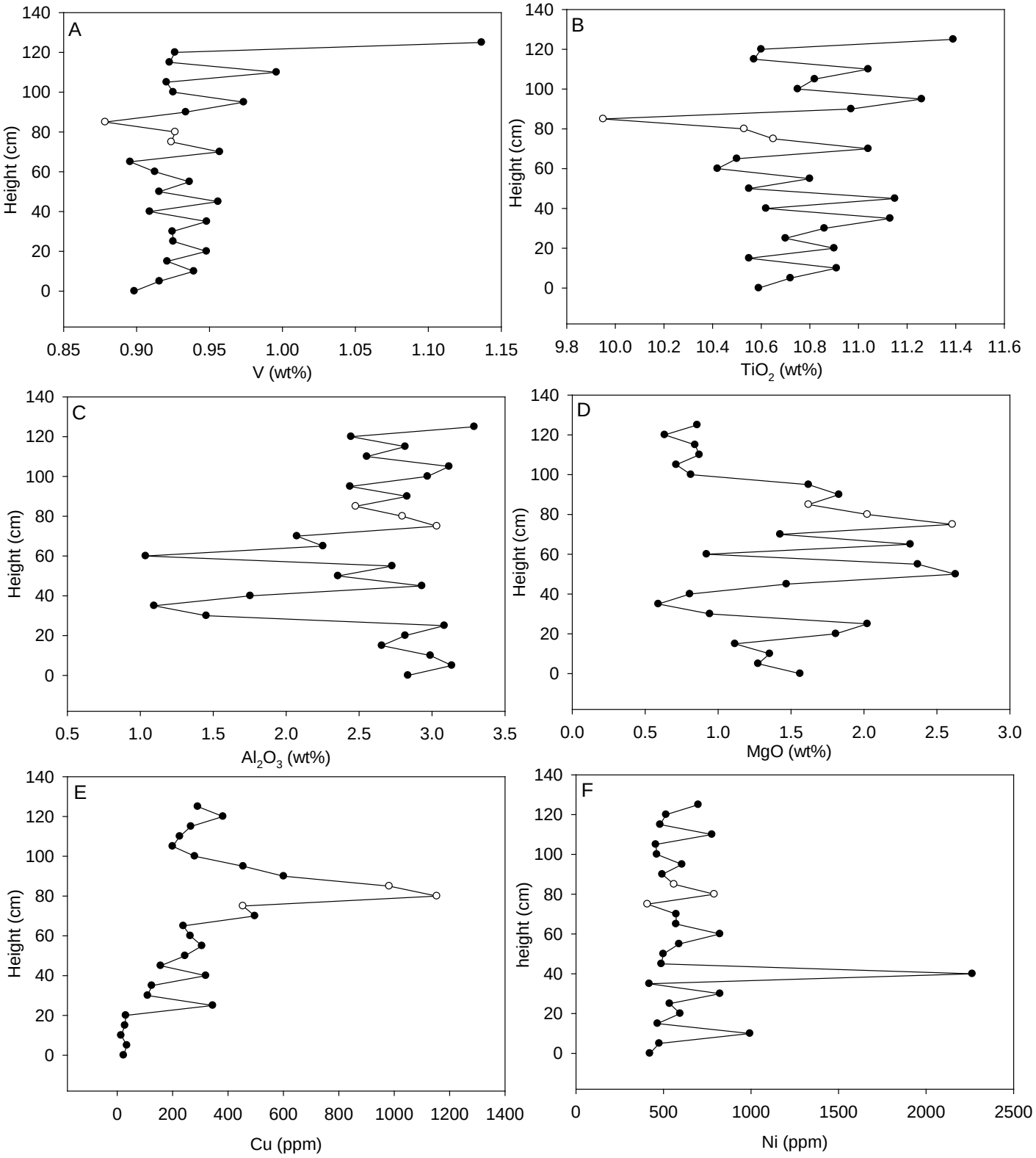

Fig. 4.5. Variation of major and trace element concentrations in magnetite through the MML in profile G.

4.5. Lateral Profiles along Base of Main Magnetitite Layer

Cawthorn (1994) presented data along basal profiles of the MML sampling both river banks (Fig. 4.6A). The samples show an average Cr content of 13 200 ppm, excluding one sample which has an unusually high Cr content of 28 800 ppm. Samples from both sides of the river do not show any co-variation even though they were taken at roughly the same position on both banks of the river about 6 m apart. Average V content is 1 wt% excluding one peak (1.09 wt%) and six low V concentrations (avg. 0.85 wt%) (Fig. 4.6B). There is some correlation in V content between samples collected on both banks. The V content however shows no correlation with Cr (Fig. 4.6).

The new data presented here are for samples more closely spaced (±2 m). The average Cr content (12 300 ppm) is comparable to the average basal samples in profiles 1-4 (12 000 ppm) (Fig. 4.7A). There are two samples, however, which deviate from the average Cr content. One sample shows an unusually high Cr content of 17 000 ppm. Another sample shows an unusually low Cr content of 9 200 ppm. The bottom halves of the three larger samples (B2, B7 and B9) split in two all show higher Cr content than the top halves (Appendix C). However, only one sample (B2) shows a significant difference between the bottom and top piece 13 200 and 10 416 ppm respectively. The more detailed 2 m spaced profile does not show any anomalous samples with either peak or low V content but rather V content is constant across the profile with an average V content of 1.04 wt% (Fig. 4.7B). Other elements TiO_2, Al_2O_3, MgO, Cu and Ni show an erratic trend across the basal profile (Fig. 4.7B).

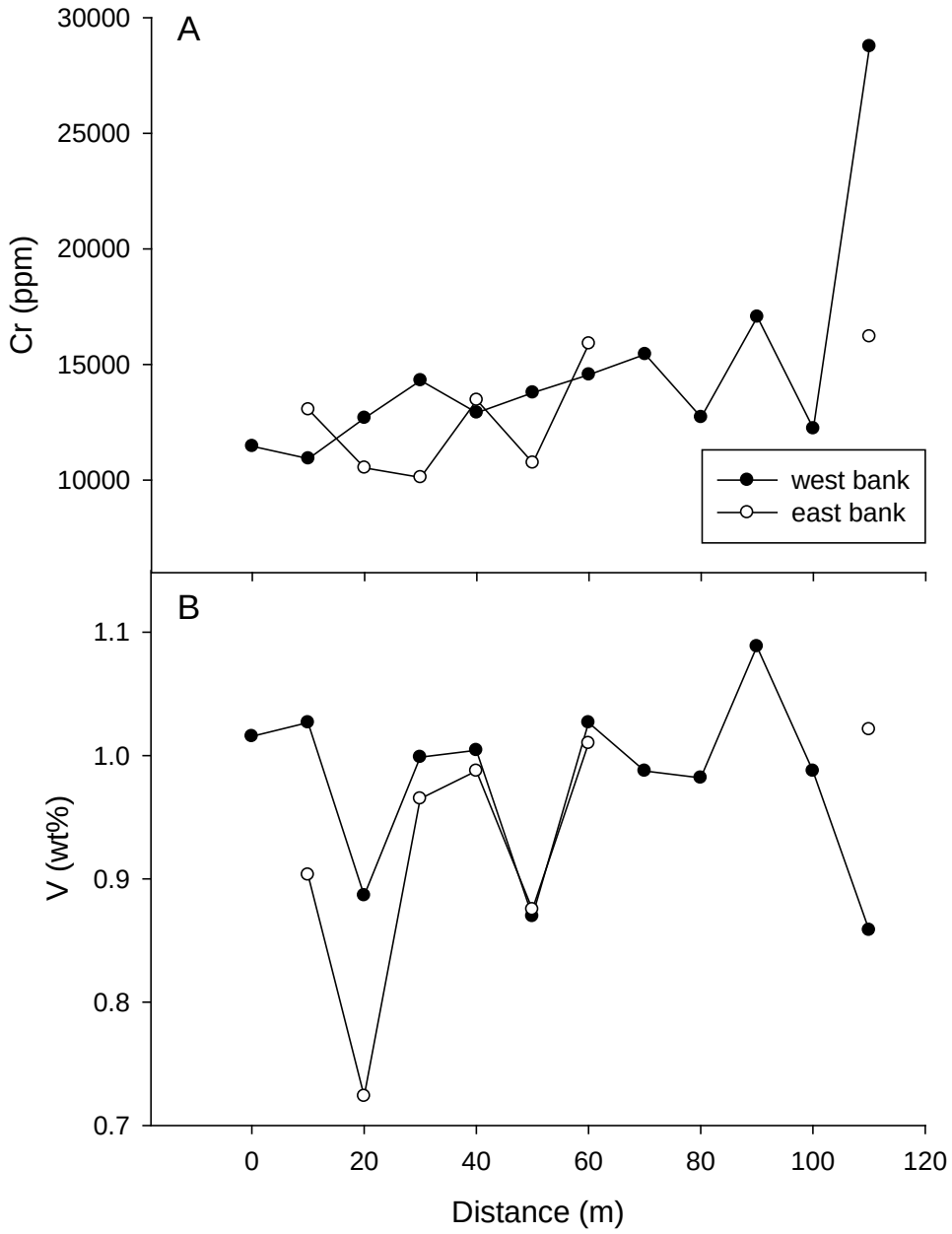

Fig. 4.6. 10 m spaced profile along base of the MML. (A) Cr and (B) V in magnetite. Data from Cawthorn (1994).

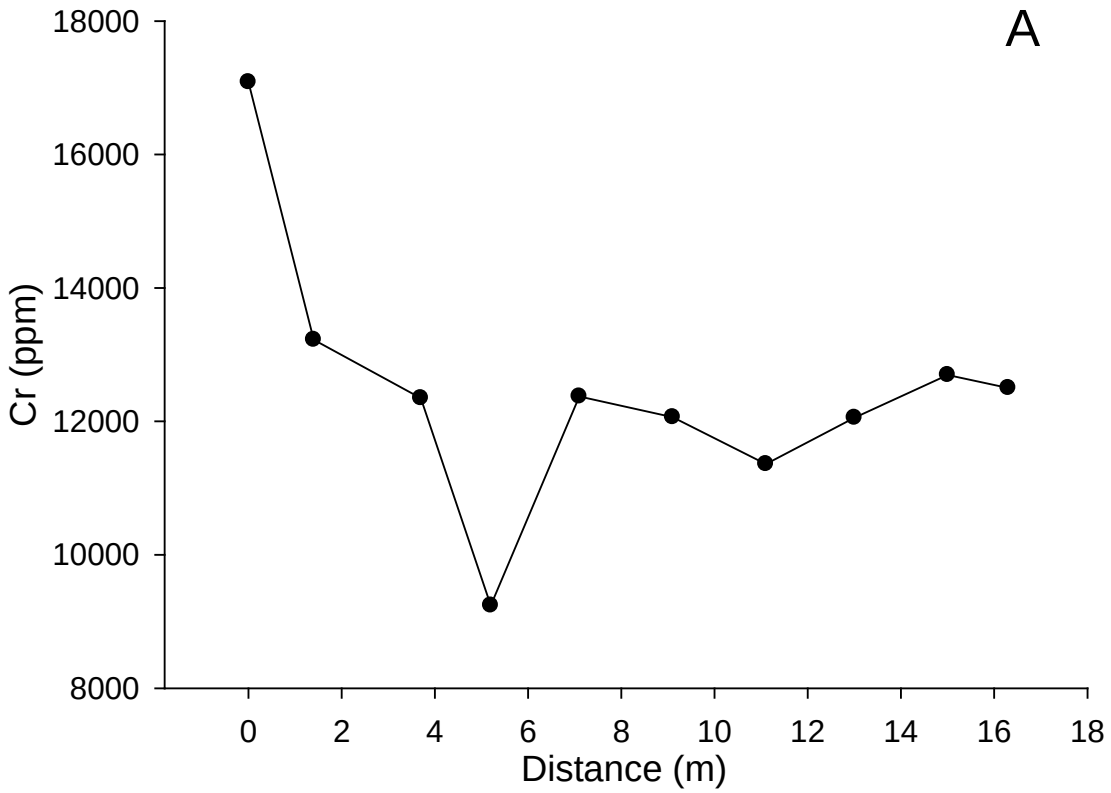
A
18000
16000
14000
12000
10000
8000
Cr (ppm)
0
2
4
6
8
10
12
14
16
18
Distance (m)

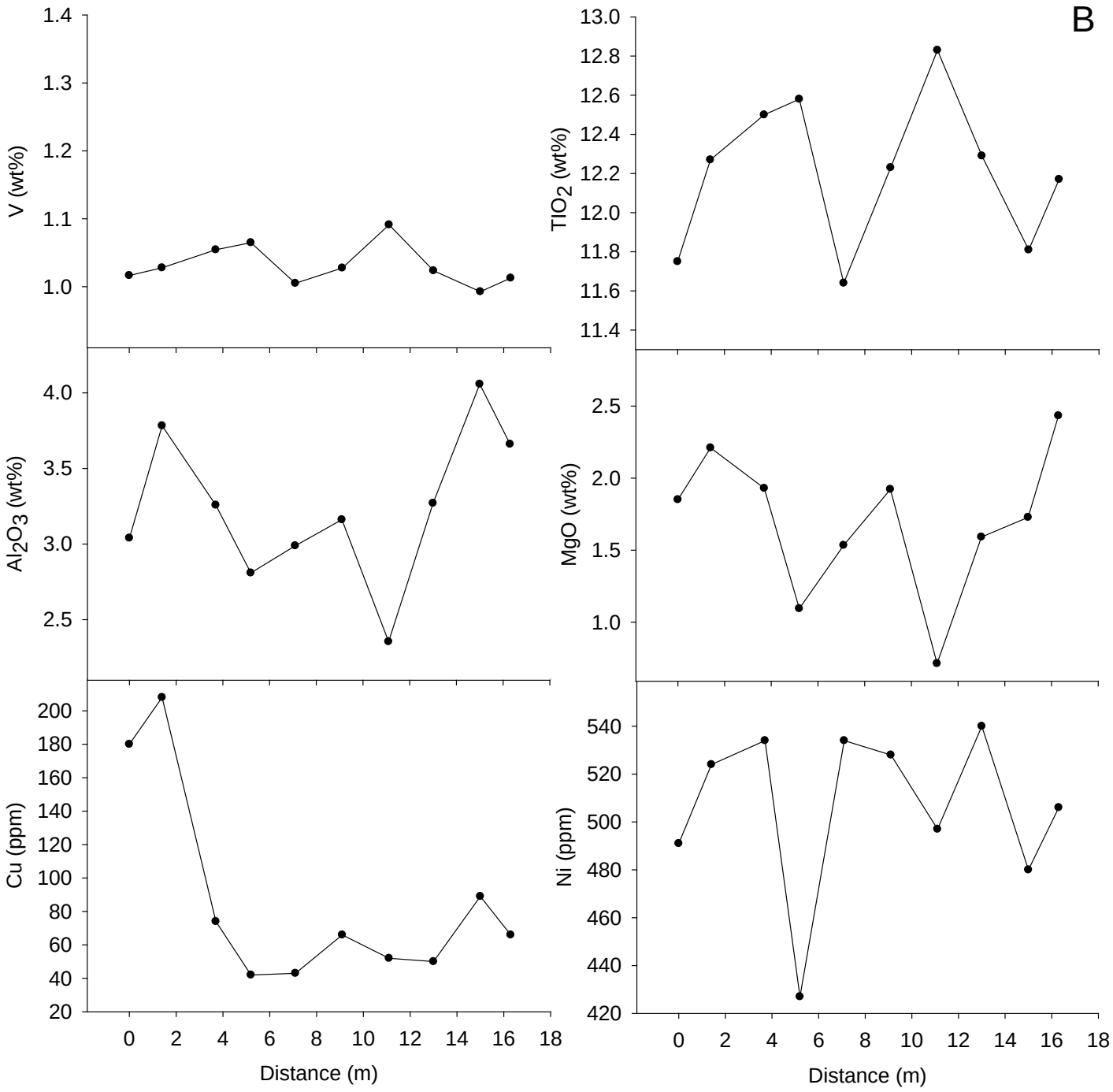

Fig. 4.7. Detailed 2 m spaced profile along the base of the MML. (A) Cr and (B) Major and trace element concentrations in magnetite.

4.6. Magnetitite Bifurcations

The Cr content at the base of the MML in the vicinity of the magnetitite bifurcations (sub-layers) (Fig. 2.1.2A) ranges between 7 800 and 5 300 ppm decreasing towards the magnetitite sub-layers (Fig.4.8). Hence the Cr content is almost half of that observed in the normal MML (12 000 ppm). Figure 4.9 shows vertical profiles through the MML in the vicinity of magnetitite sub-layers. Profile SL1 through the MML shows an upward decrease in Cr content (Fig. 4.9). Vertical profiles SL2 and SL3 typically show an upward decrease in Cr content, 6 400-1 500 ppm and 7 500-676 ppm respectively, from the base to the top of the MML with one reversal in Cr content occurring in profile SL3 at 30 cm (3 200-3 600 ppm) (Fig.4.9). Profiles SL4 and SL5 collected from midway through the MML also show an upward decrease in Cr with one reversal in Cr occurring at the top of profile SL4 (Fig. 4.9), Figure 4.10 shows vertical profiles for Cr through sub-layers 2-4. All vertical profiles taken through the sub-layers (SL6-SL10) typically show an upward decrease in Cr content with only one minor reversal in Cr content noted in profile SL9 at 12 cm (900-1 100 ppm) (Figs. 4.10A-C). Profile SL10, however shows an initial increase in Cr over the first 8 cm (932-1 300 ppm) and, thereafter decreases towards the top of sub-layer 4. A reversal in Cr content occurs at towards the bases of sub-layers with disseminated magnetite in the magnetitite-rich anorthosite separating the sub-layers typically having lower Cr contents (<1 000 ppm) than the magnetitite sub-layers (Fig. 4.10A).

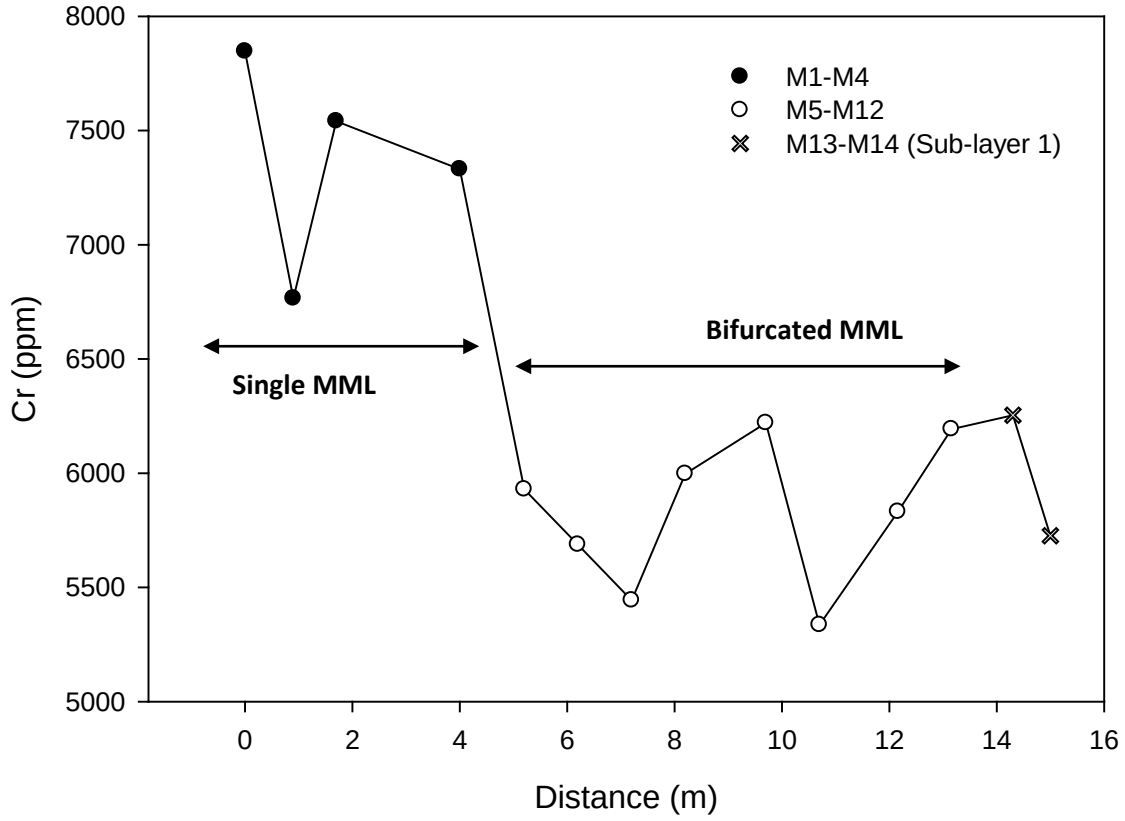

Fig. 4.8. Cr in magnetite along base of the MML in vicinity of magnetite bifurcations. Locations of samples M1-M14 are shown on Fig. 3.4.

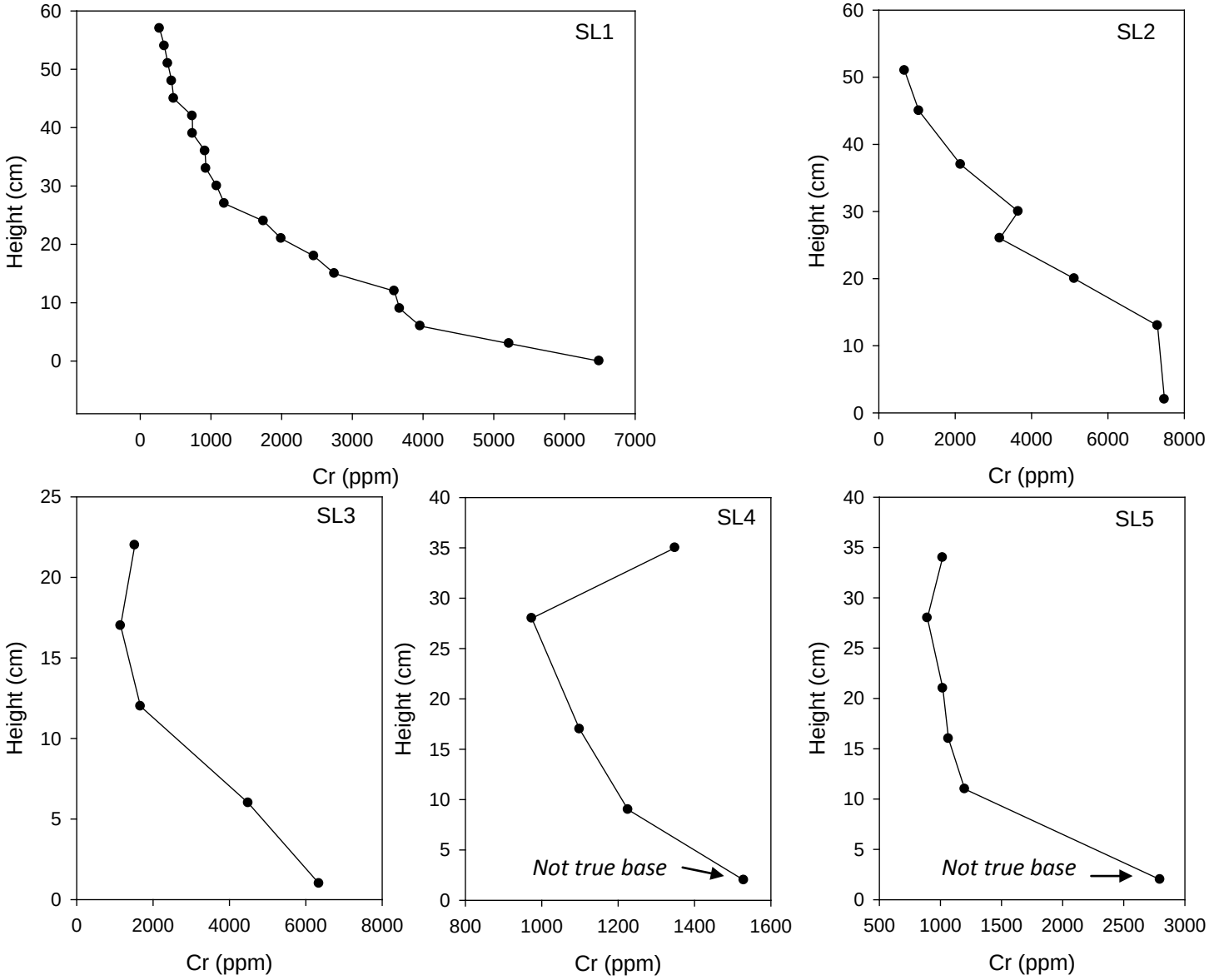

Fig. 4.9. Cr in magnetite in vertical profiles in normal MML in vicinity of bifurcations. Note profiles SL4 and SL5 were collected from halfway through the MML thus samples at base of the profiles do not represent the base of the MML.

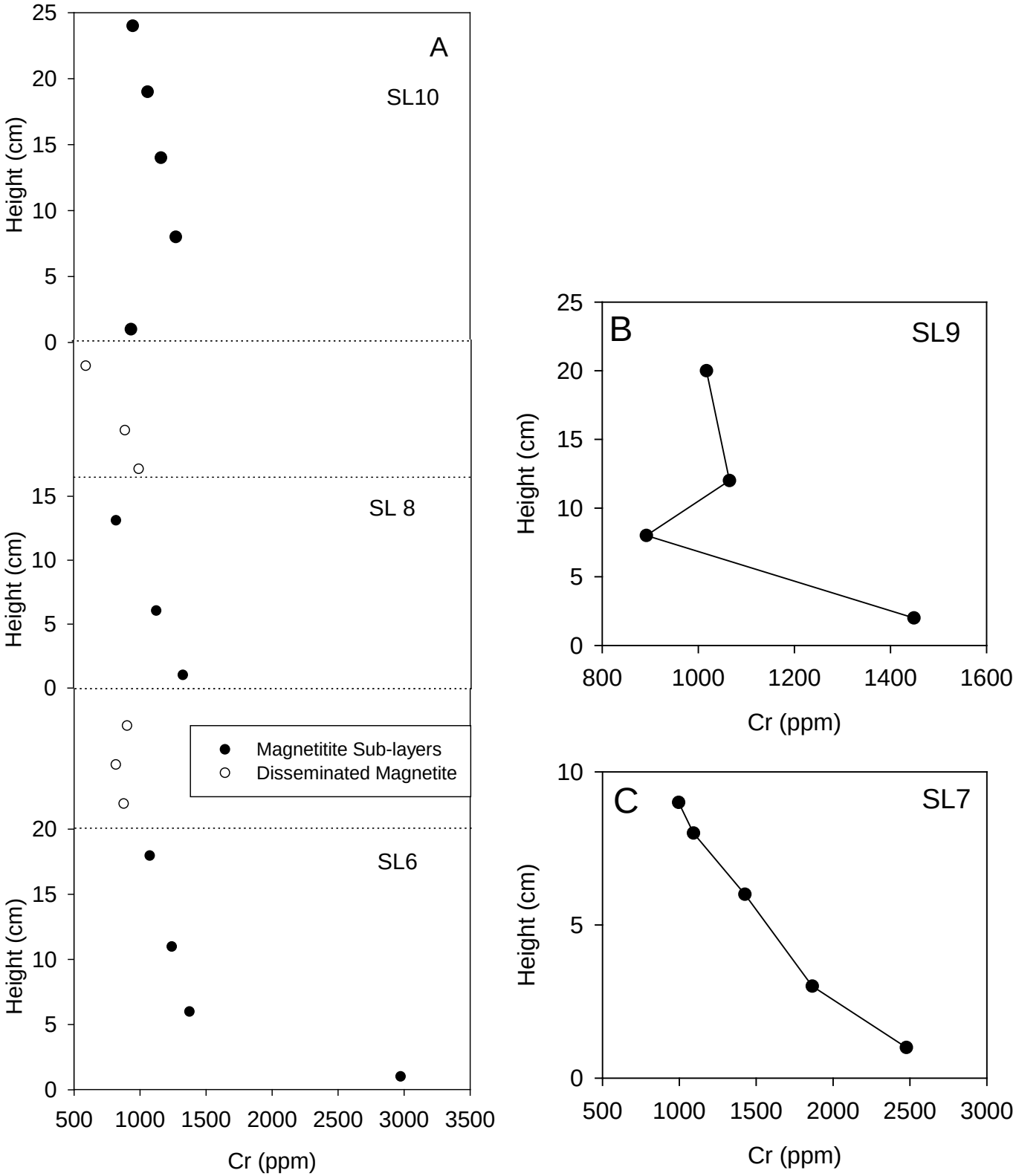

Fig. 4.10. Cr in magnetite through bifurcated sub-layers 2-4. (A) Composite vertical section through sub-layers 2-4. (B) Vertical profile through sub-layer 3. (C) Vertical profile through sub-layer 2.

4.7. Vertical Sections through Layer 1

The vertical profiles for Cr taken through layer 1 (Fig. 3.5) in the normal section (L1/1-L/3) and the section above the impermeable xenolith (L1/4-L1/9) are shown in Figures 4.11 and 4.12 respectively. Profiles through the normal section typically show an upward decrease in Cr content with minor reversals in Cr content (±50 ppm) occurring in profiles L1/1 (5, 8 and 10 cm); L1/2 (9 cm) and L1/3 (8 and 10 cm). Profiles taken above the xenolith also show an upward decrease in Cr with the largest reversals noted in profile L1/4 at 10 cm (2 000-2 100 ppm) and in L1/6 at 8 cm (2 100-2 400 ppm). Reversals in the other profiles are minor (±50 ppm). A minor initial increase in Cr content within the bottom 4 cm of layer 1 is noted in profiles L1/5 (2 100-2 300 ppm) and L1/9 (2 400-2 500 ppm).

The V content in the profiles through the normal section and above the xenolith do not show any systematic variation with V content ranging between (0.85-1.1 wt%) (Figs. 4.11; 4.12). An increase in V content is noted within the bottom 2 cm in profiles L1/2 (1.06-1.08 wt%); L1/3 (1.01-1.07 wt%); L1/4 (0.99-1.03 wt%); L1/7 (0.94-0.98) and L1/9 (0.94-1.01 wt%). There is a slight correlation in Cr and V in only profile L1/9 with the rest of the profiles showing poorer correlation.

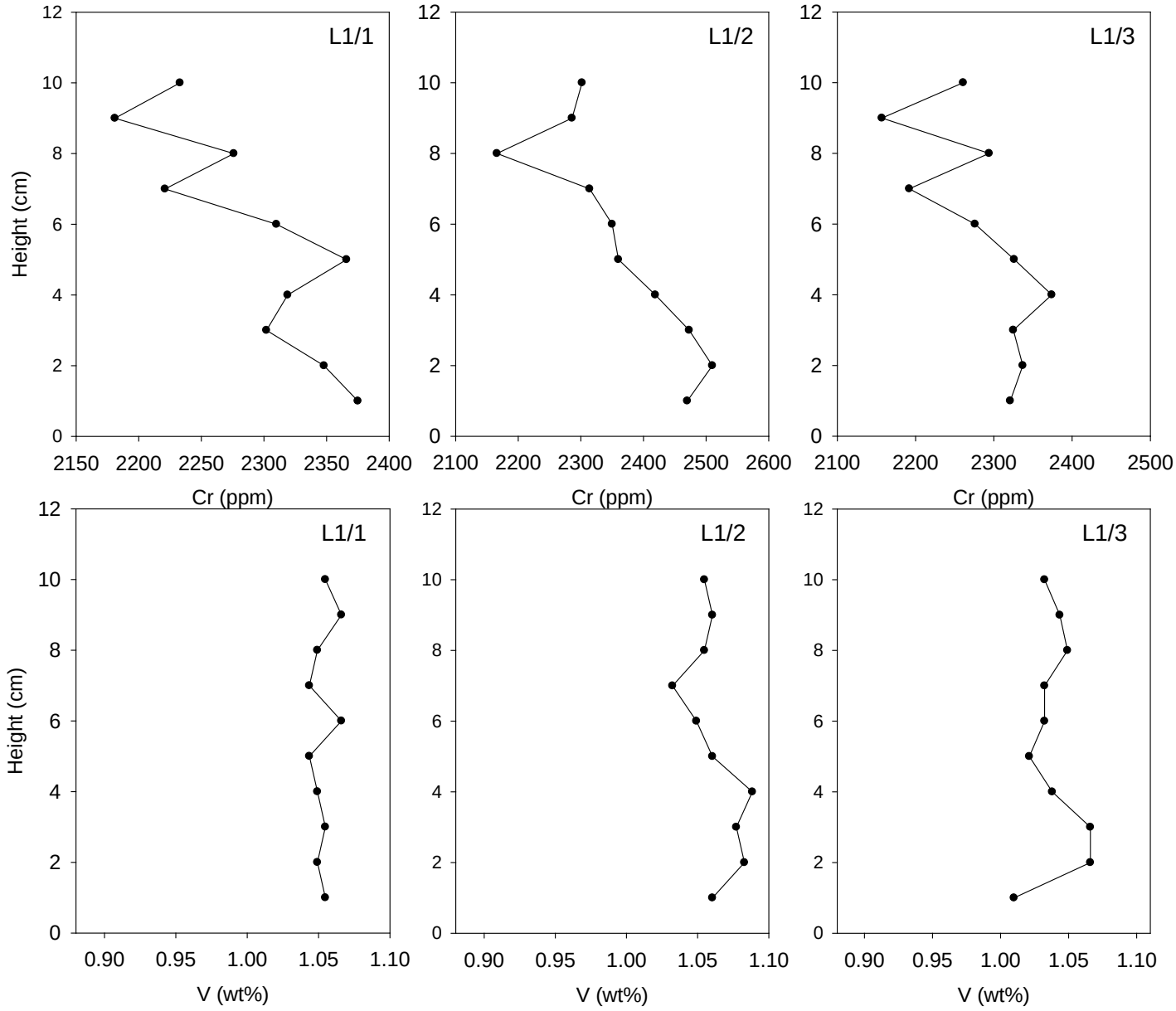

Fig. 4.11.Variatio of Cr and V in magnetite for profiles (L1/1-L1/3) taken through normal section of Layer 1.

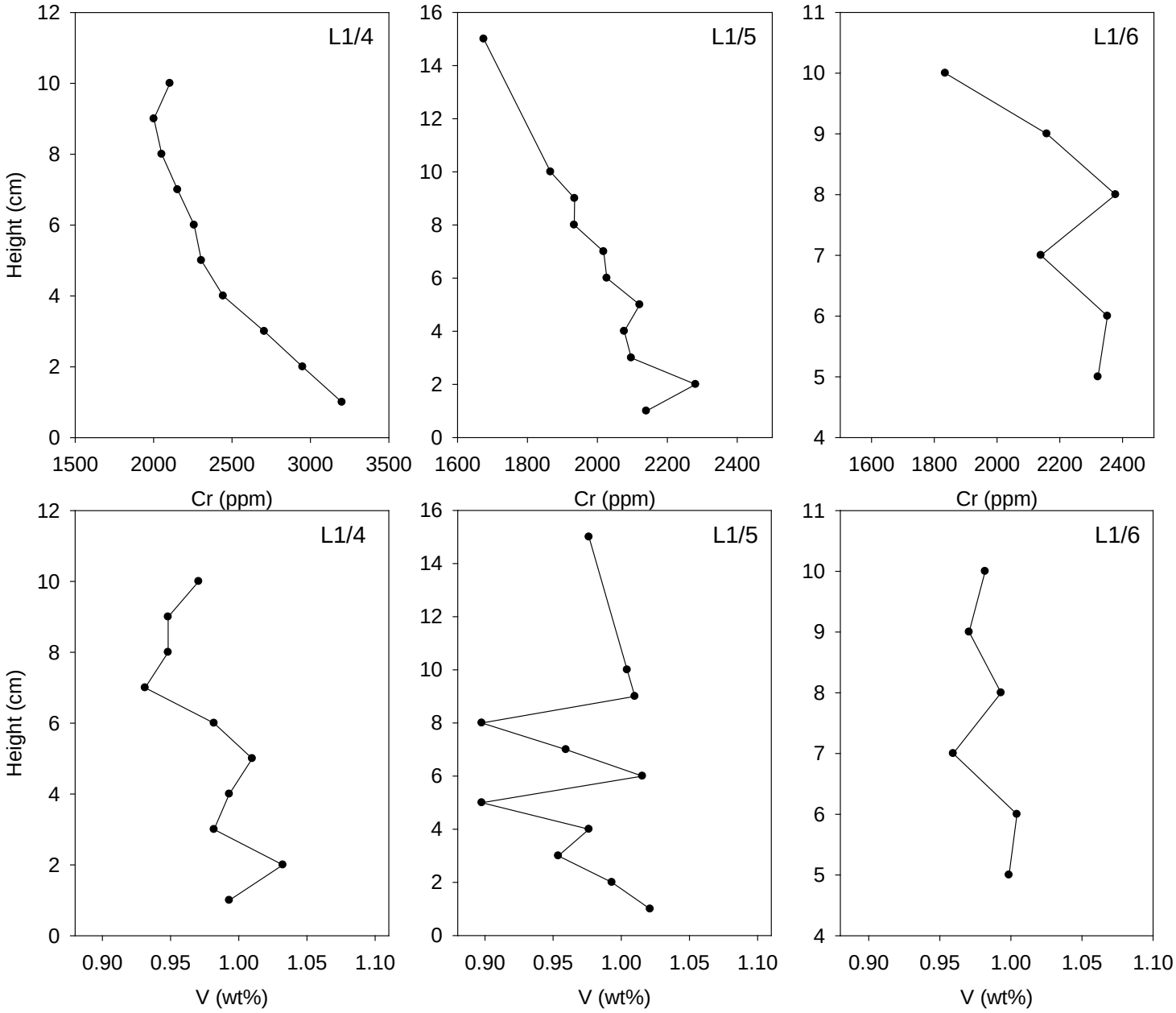
L1/4
L1/5
L1/6
Height (cm)
Cr (ppm)
V (wt%)

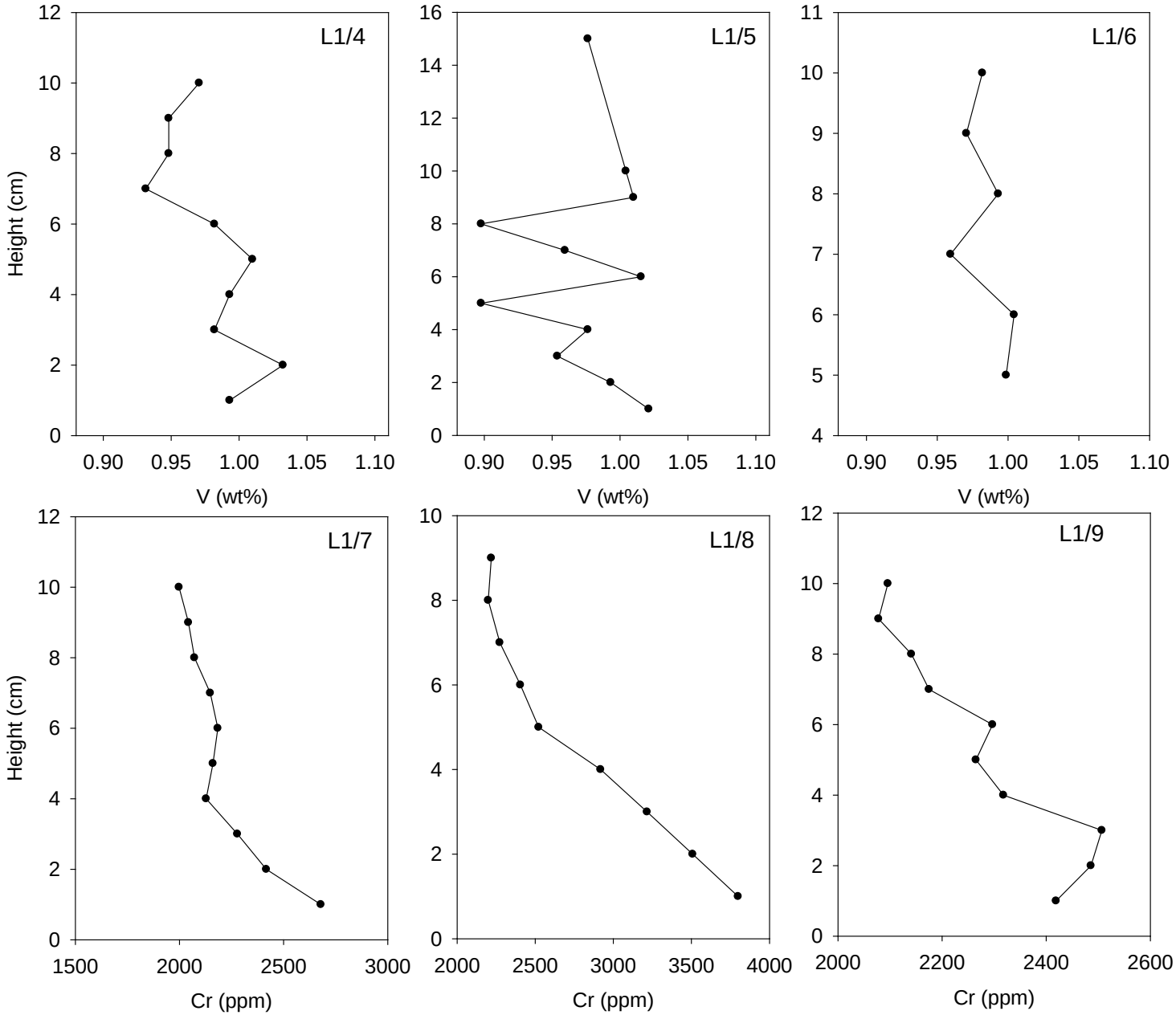

Fig. 4.12. Variation of Cr and V in magnetite for profiles (L1/4-L1/9) taken above impermeable xenolith in Layer 1.

Figure 4.13 shows the basal samples of vertical profiles taken through layer 1. The normal section of the base of layer 1 shows an average Cr content of 2 400 ppm. Samples taken above the xenolith show some irregularities. Four of the six samples are comparable with the samples collected from the normal section with Cr content ranging from 2 100 to 2 700 ppm. Two samples however show atypically high Cr content of 3 200 and 3 800 ppm respectively.

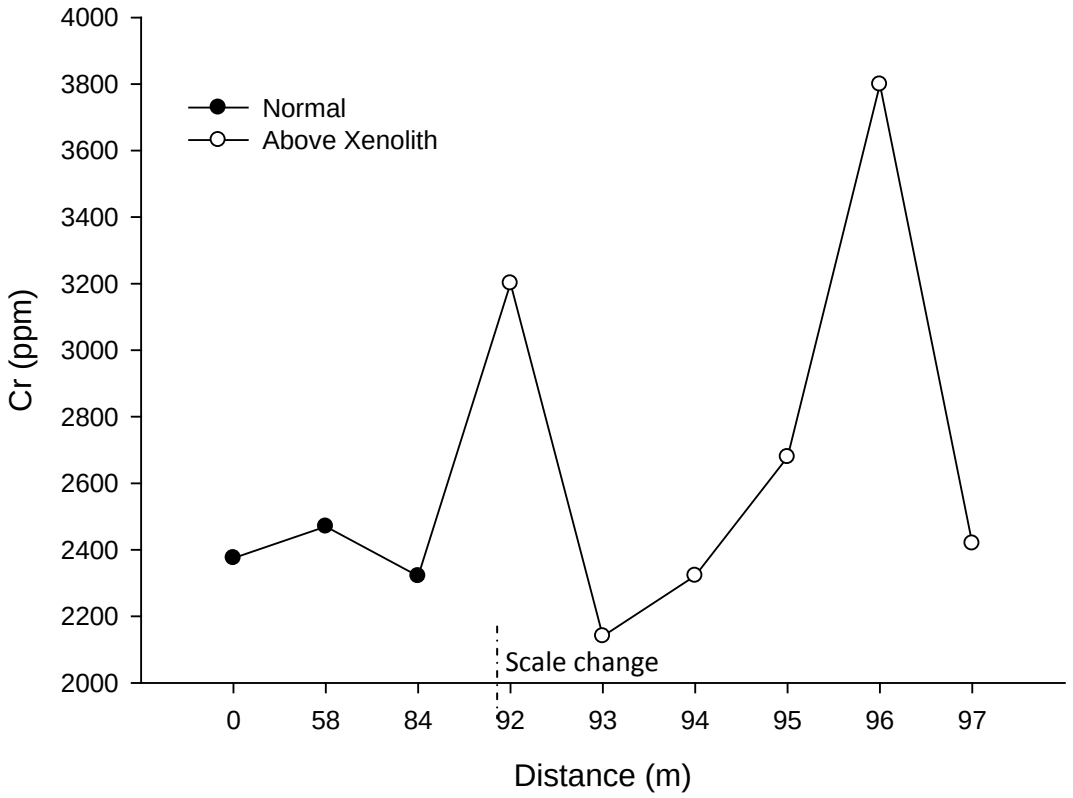

Fig. 4.13. Cr in magnetite along base of layer 1. Samples in the normal section (filled circles) and above an impermeable basalt xenolith (open circles) are shown. Note scale change between samples in the normal section and samples above the xenolith.

4.8. Vertical Section through Magnetite-rich Sequence, Brits (UCAR Mine Drill Core)

Figure 4.14 shows a drill core log from UCAR mine in the Brits area in the western limb. At the base of the drill core (662-506 cm) is a sequence of massive magnetitite, with a 19 cm intermediate zone characterized by the presence of cumulus feldspar crystals (possibly equivalent to the feldspar parting). Immediately above this section is a 2 cm thick anorthosite band, overlain by 44 cm thick massive magnetite with a 2 cm thick ‘feldspar parting’ toward the base. This section is followed by a 225 cm thick anorthosite with disseminated magnetite,

and another section of massive magnetite 53 cm thick. This section shows an upward decrease (over 30 cm) in modal plagioclase into anorthosite. The overlying section of anorthosite with disseminated magnetite is 172 cm thick and is the top section studied. The features outlined above, pertaining to the bottom section (662-450 cm) of the drill core, closely resemble those of the MML at Magnet Heights. The overlying massive magnetitite layer separated from the basal section of the MML by the 225 cm thick anorthosite can be correlated with magnetitite layer 1.

Magnetite separates from the drill core show that the base of MML in the Brits area has a Cr content of 13 000 ppm comparable to that noted by Cawthorn (1994) (Fig. 4.14A). The Cr content shows an upward depletion, however interrupted by a number of reversals. A sharp upward depletion in Cr (13 000-2 000 ppm) within a short interval (667-651 cm) is noted at the base of the MML. Three reversals in Cr content are present at 638 cm (2 000-2 700 ppm); 505 cm (500-2 000 ppm) and 226 cm (100-1 500 ppm). Two of the reversals (638 and 505 cm) occur in the massive magnetite section of the MML whereas the reversal at 226 cm occurs at the base of layer 1. Cr reversals do not attain the same Cr content recorded at the base of the MML. The Cr content at the base of layer 1 (1 500 ppm) in the drill core is slightly lower than that recorded at the base of layer 1 (2 400 ppm) in Magnet Heights. Disseminated magnetite within the anorthosite sections (445-225 and 174-0 m) show a constant Cr content with increasing height both averaging 560 ppm. An unusually sharp decrease in Cr (600-100 ppm) occurs within the disseminated magnetite section (253 cm) immediately below the base of layer 1. No reversals are observed in the disseminated magnetite sections.

Vanadium content through the drill core generally shows an upward decrease from 1.19 at the base to 0.69 V wt% at the top of the drill core (Fig. 4.14B). Vanadium content through the MML shows no systematic variation. One protracted reversal in V content through nearly 1 m occurs at the base of layer 1 (226 cm) and is coincidental with a reversal in Cr. The V content in the MML and layer 1 is higher (0.96 and 0.86 wt% respectively) than in the disseminated magnetite occurring in the 225 and 175 cm thick anorthosite sections having 0.78 and 0.74 V wt% respectively. There is no correlation between V and Cr, except immediately below layer 1.

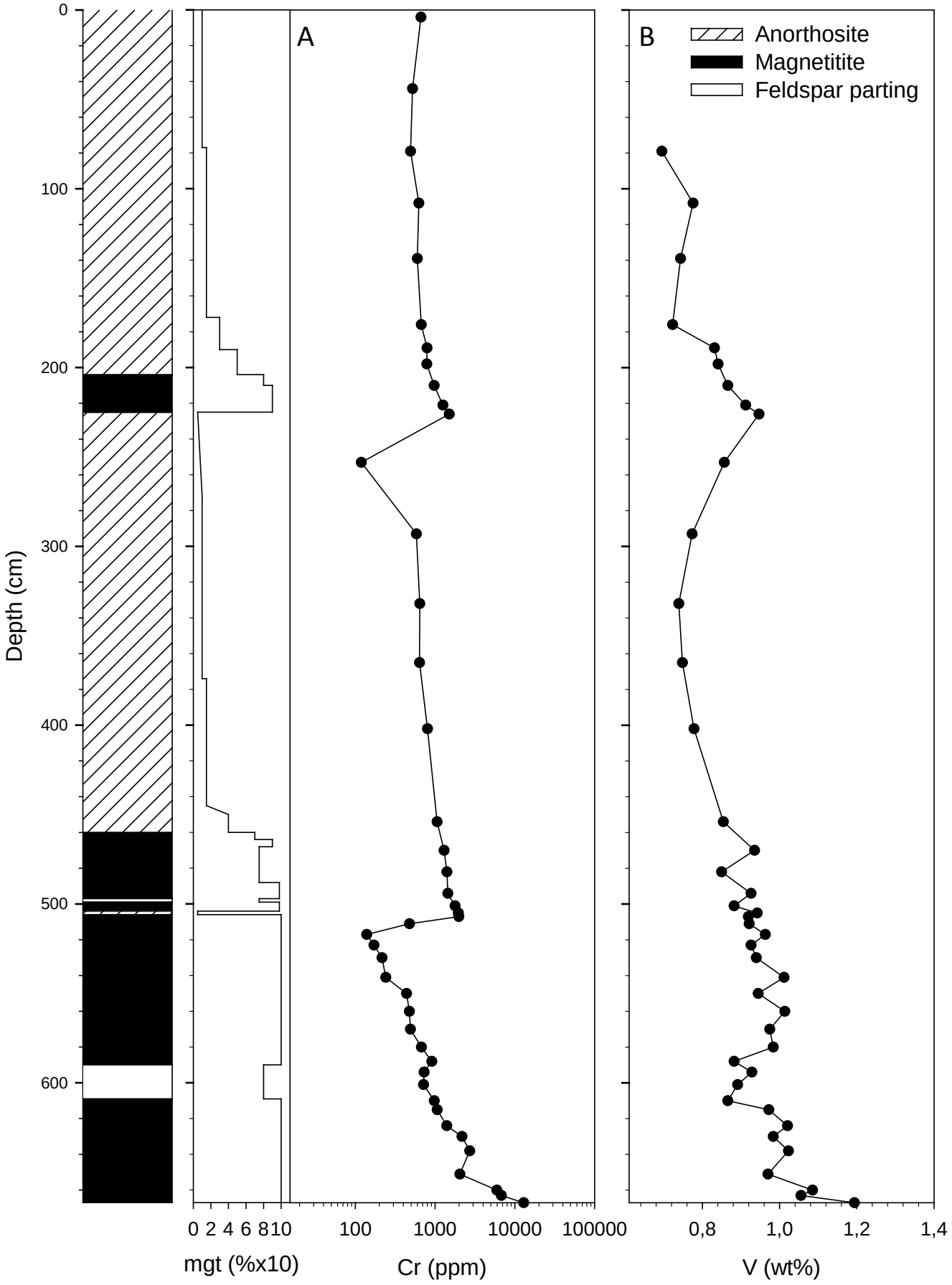

Fig. 4.14. Vertical profile of UCAR mine drill core. (A) Cr and (B) V contents in magnetite.

4.9. Vertical Section through the Upper Zone in the Western Limb (Bierkraal Drill Cores)

Drill cores BK 1 and BK 3 were drilled through the UZ in the western limb by the Council for Geosciences. BK 1 and BK 3 have previously been correlated by Tegner et al. (2006). The composite drill core presented in Figure 4.15 is composed of sections 0-1 600 m and 540-1 400 m of BK 1 and BK 3 respectively. Tegner et al. (2006) identified a total of twenty six magnetitite layers and six nelsonite (apatite-Fe-Ti oxide) layers present in drill cores BK 1 and BK 3. The Cr and V content of magnetite and plagioclase composition (An%) plotted against depth are presented in Figure 4.15. A constant Cr content typically <1 000 ppm is observed through most of the drill cores. This trend is however interrupted by several intervals of high Cr content (Fig. 4.15A) at 2 425, 2 343 (minor increase), 1 978, 1 488 and 1 117 m and are associated with some magnetitite layers. Two samples collected from the MML located at the base of the composite borehole (2 425.85 and 2 424.8 m) have Cr contents of 2 400 and 1 624 ppm respectively. Not all the samples taken from magnetitite layers have higher Cr content than adjacent samples. There are several samples from magnetitite layers which have low Cr content (<1 000 ppm). Conversely, there are some disseminated magnetite samples which show atypically high Cr content. These atypical disseminated magnetite samples occur adjacent to the magnetitite samples showing sharp increases in Cr with the exception of samples occurring at 1 640 and 880.5 m. The identified sharp increases in Cr differ in magnitude ranging from 2 000 to 6 300 ppm. The sharpest increase in Cr content occurs midway through the drill core at 1 488 m (just below layer 21) and is coincident with a cluster of magnetitite layers.

From the base up to midway through the composite drill core, V shows a decrease from 1.2 to 0.07 wt% with little interruption in the trend. The upper half of the composite drill core however, shows a cyclic trend characterised by several reversals in V content (Fig. 4.15B), but low concentration. Two of the reversals in V are coincident with sharp increases in Cr (Figs. 4.16E-F and I-J). One protracted reversal in V content is offset about 16 m above the adjacent sharp increase in Cr (Fig. 4.16G-H) but the base of the reversal in V corresponds in height with the adjacent abrupt increase in Cr. The other sharp increase in Cr is not coincidental with reversals in V (Fig. 4.16C-D).

The An content of plagioclase is shown in Figure 4.16C. There are several reversals in An content with only one of the reversals, occurring at 1 488 m, coinciding with an increase in Cr content but is offset 16 m below the nearest reversal in V.

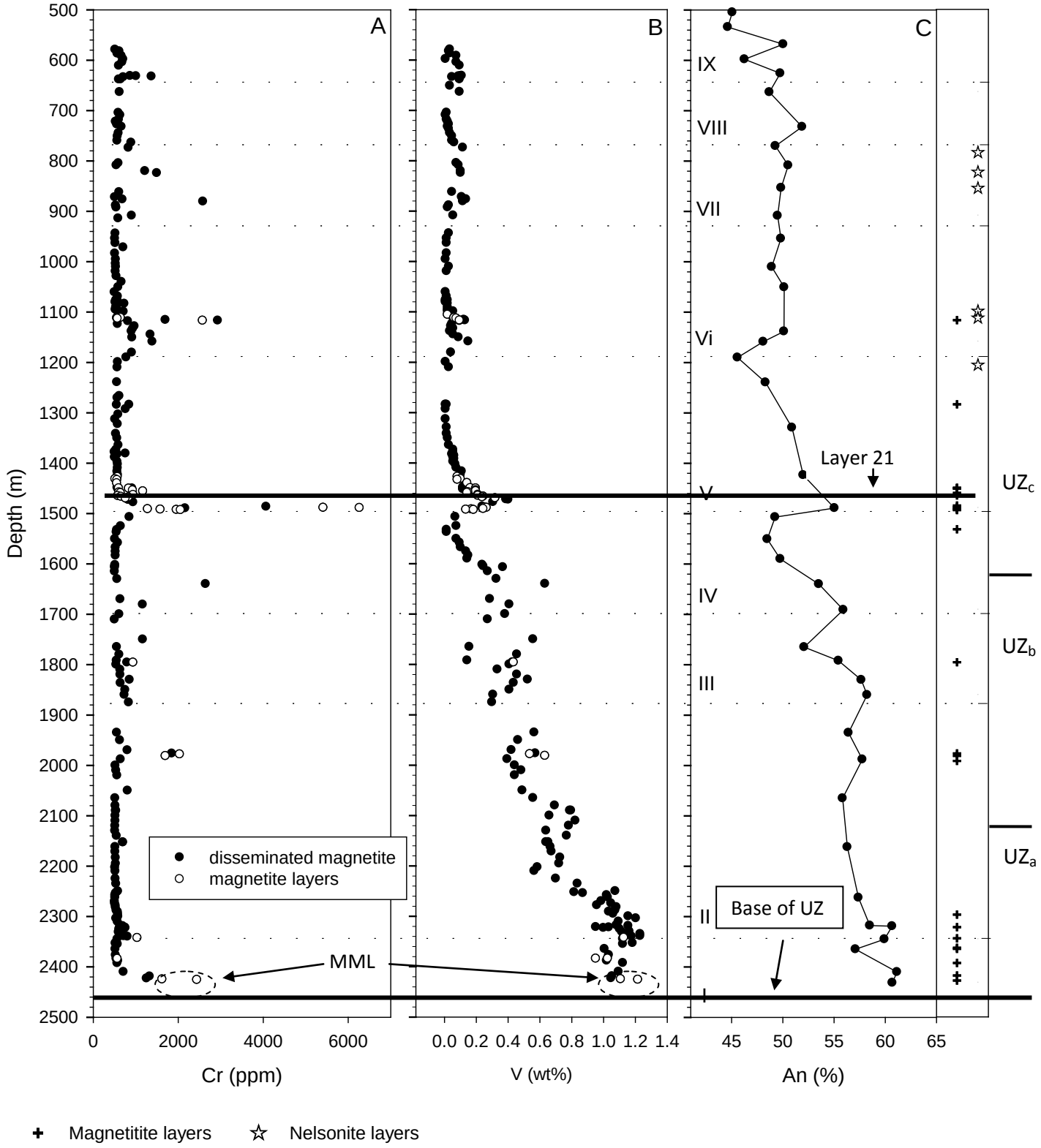

Fig. 4.15. Geochemistry of magnetite and plagioclase from BK drill cores. Variation in (A, B) Cr and V of magnetite and (C) plagioclase An% through the composite BK drill core. Stratigraphic positions of magnetitite layers (crosses), nelsonite (apatite-rich magnetitite) layers (stars) and postulated 'fractionation' cycles (dashed lines) by Tegner et al. (2006) are also shown. Cycles are numbered with roman numerals (I-IX). V and An % data from Tegner et al. (2006).

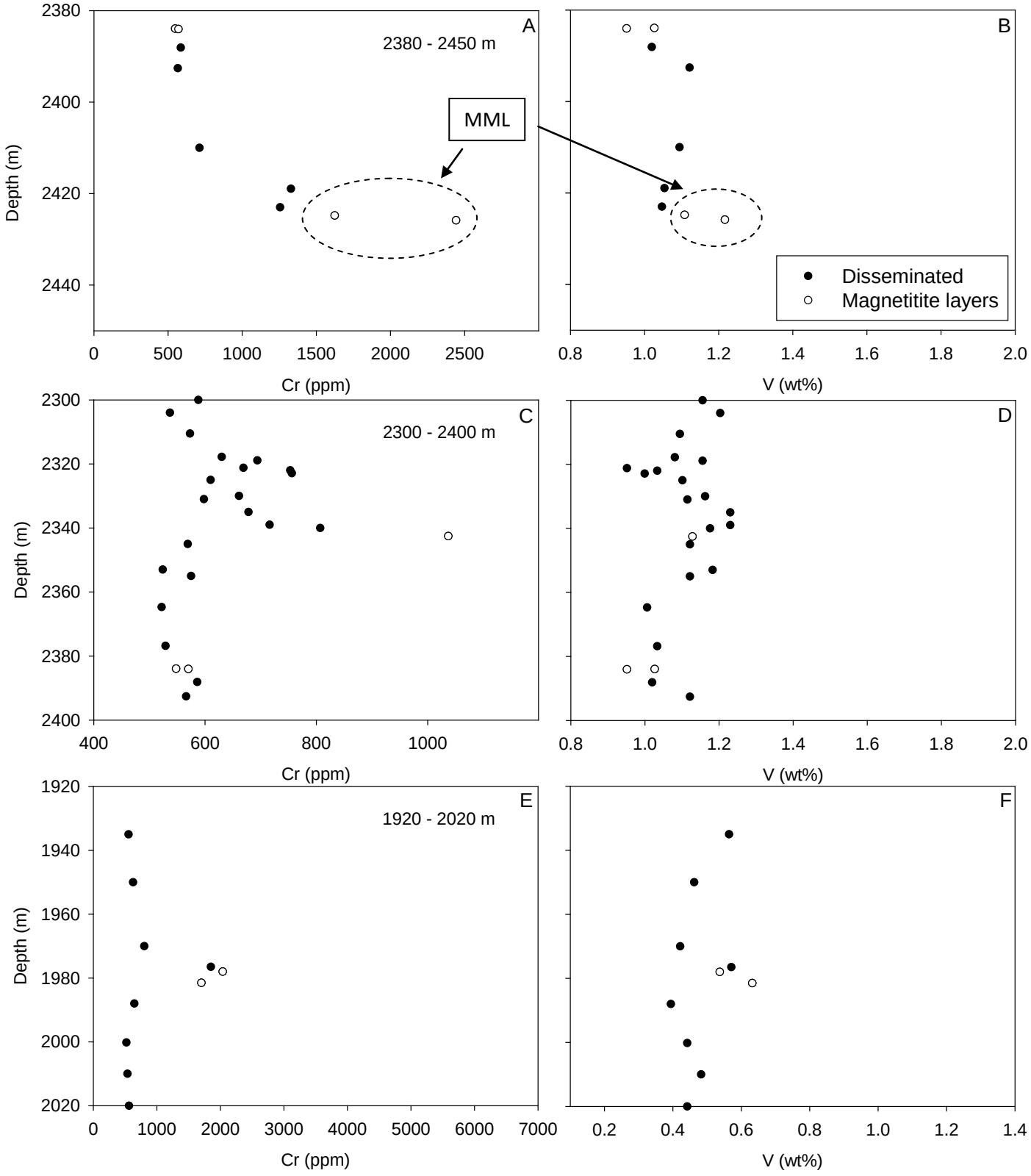
A
2380 - 2450 m
MML
B
Disseminated
Magnetitite layers
Depth (m)
Cr (ppm)
V (wt%)
C
2300 - 2400 m
D
E
1920 - 2020 m
F

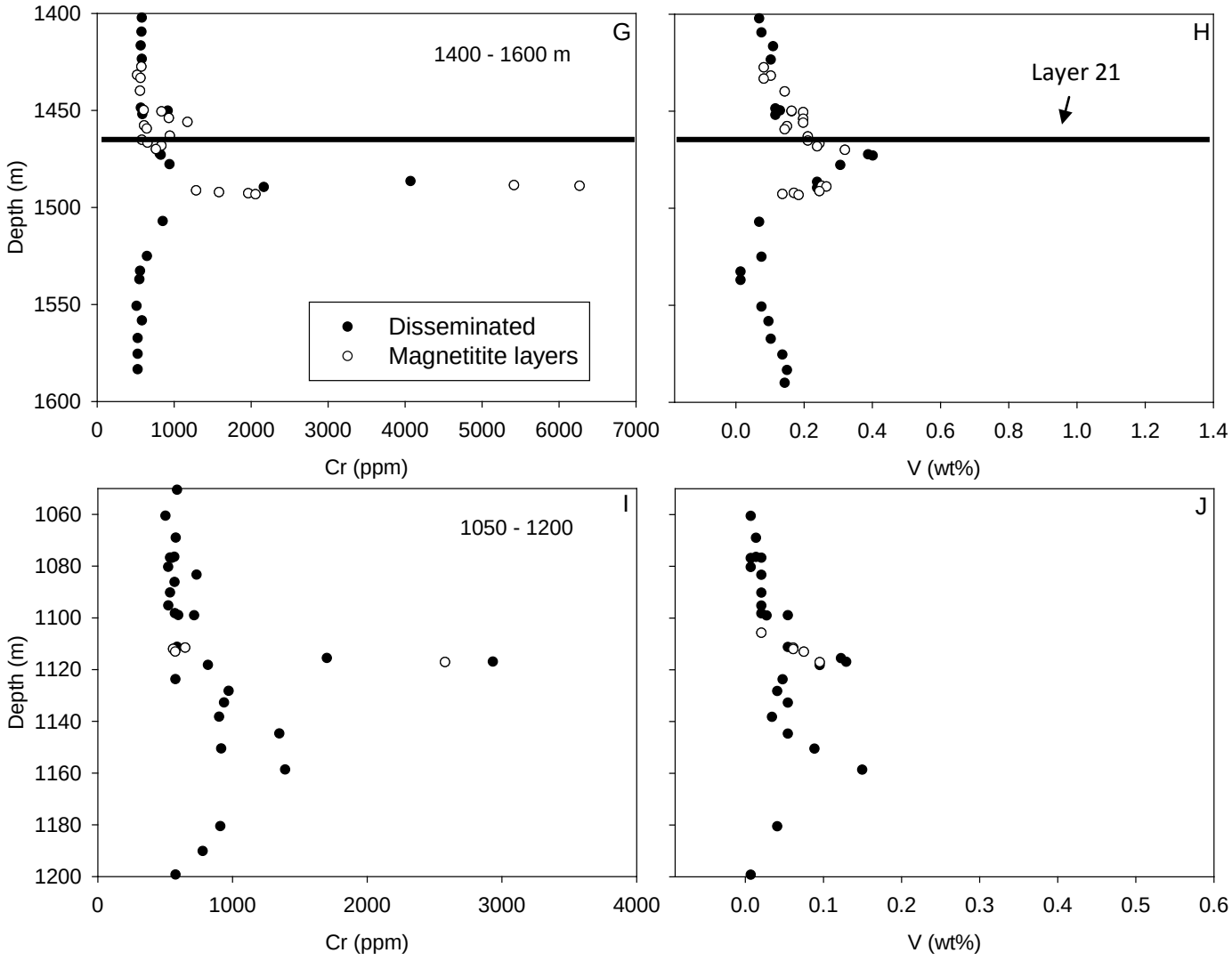

Fig.4.16. Details of sections showing sharp increases in Cr content from composite BK drill core.

Table 4.2 shows a comparison of compositions between the magnetitite layers and the disseminated magnetite. The magnetitite layers in subzones B and C have a similar MgO content to that of the disseminated magnetitite. The magnetitite layers at the base in subzone A, however, have higher MgO content than the adjacent disseminated magnetite. In all subzones, the Al_2O_3 content is higher in the disseminated magnetite compared to the magnetitite layers. V content is slightly higher in the magnetitite layers, especially in subzone C, as compared to the disseminated magnetite in all the subzones. In all the subzones TiO_2 is higher in the magnetitite layers compared to the disseminated magnetite. The Cr contents of the magnetitite layers are very much higher than the disseminated sections.

Table 4.2 Average Composition (MgO, Al_2O_3 and V) of Magnetitite Layers and Disseminated Magnetite in Subzones UZa, UZb and UZc from the BK Drill Core

		UZa	UZb	UZc
MgO (wt%)	mgt layer	1,44	1,22	0,91
	disseminated	0,74	1,20	0,92
Al_2O_3 (wt%)	mgt layer	1,51	1,98	1,51
	disseminated	1,77	2,61	2,22
V (wt%)	mgt layer	1,09	0,53	0,16
	disseminated	1,02	0,51	0,07
Cr (ppm)	mgt layer	1244	1560	1348
	disseminated	619	724	755
TiO_2 (wt%)	mgt layer	12,06	11,67	15,61
	disseminated	10,93	10,63	12,43

4.10. Vertical Section through the Upper Zone in the Northern Limb (Bellevue Drill Core)

The Bellevue (BV-1) drill core is a ~2 950 m drill core which was drilled through the northern limb and has been documented by Ashwal et al. (2005) and Cawthorn and Ashwal (2009). This drill core intersects the entire UZ and half of the MZ. Cawthorn and Ashwal (2009) identified twenty magnetitite layers in the drill core. Data presented below has been collected by Ashwal et al. (2005).

Figure 4.17 shows the distribution of plagioclase, pyroxene (clinopyroxene + orthopyroxene) and olivine through the UZ. The modal amount of disseminated magnetite is typically <20 % in the host rocks however, there are several magnetite-rich samples with a maximum of 60 % magnetite. Some of the magnetite-rich samples are adjacent to magnetitite layers (1 410-1 316 m and 904-830 m) whereas other samples are not adjacent to magnetitite layers.

Electron microprobe analyses of magnetite from magnetitite layers and disseminated magnetite in the BV-1 drill core are presented in Figure 4.18. The magnetitite layers generally show a higher MgO content than the disseminated layers (Fig. 4.18A). There appears to be no

difference between the magnetitite layers and the disseminated magnetite in terms of V and Al_2O_3 content (Figs. 4.18B, C).Vanadium shows a uniform decrease (1.5-0.75 wt%) from the base of the UZ to midway through the UZ thereafter showing a pronounced decrease (0.75-0.08 wt%) over 182 m. The pronounced decrease in V is followed by a reversal in V (Fig. 4.18C). The upper half of the BV-1 drill core contains less data than the lower half and thus no pronounced cycles in V content as those observed in the BK drill cores are observed.

Plagioclase composition is constant, averaging 56 An%, for about 700 m from the base of the UZ up to midway through the drill core, thereafter decreases to 46 An%. The decrease is followed by one major protracted reversal in An% over 74 m (Fig. 4.18D). This reversal in An% coincides with the reversal noted in V and coincident with the stratigraphic position of a cluster of magnetitite layers identified by Cawthorn and Ashwal (2009).

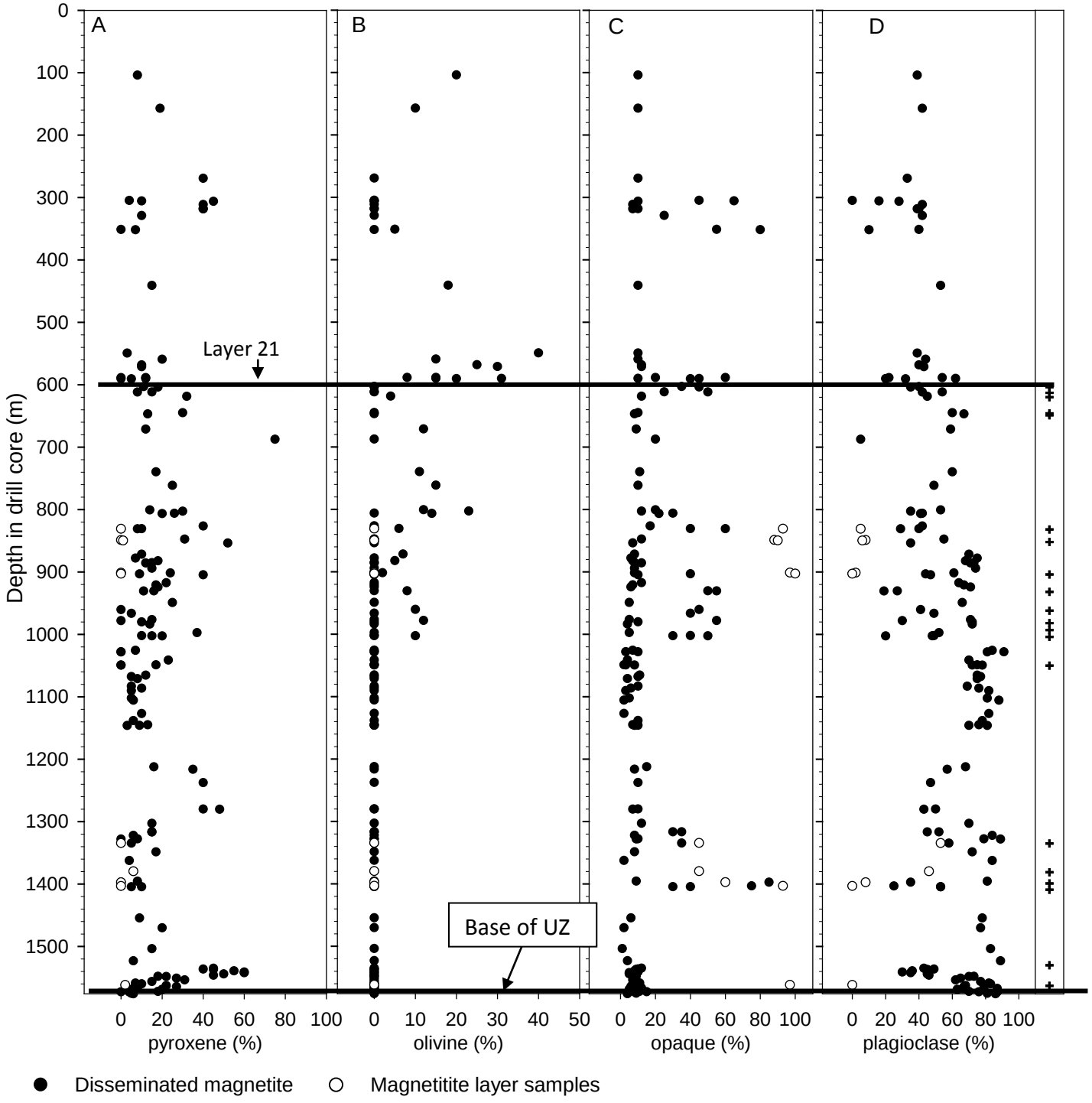

Fig. 4.17. Modal mineralogy (visually estimated percentage) in the BV-1 drill core. (A) pyroxene (clinopyroxene + orthopyroxene); (B) olivine; (C) magnetite and (D) plagioclase. Stratigraphic positions of magnetitite layers identified by Cawthorn and Ashwal (2009) are marked with crosses. Data from Ashwal et al. (2005).

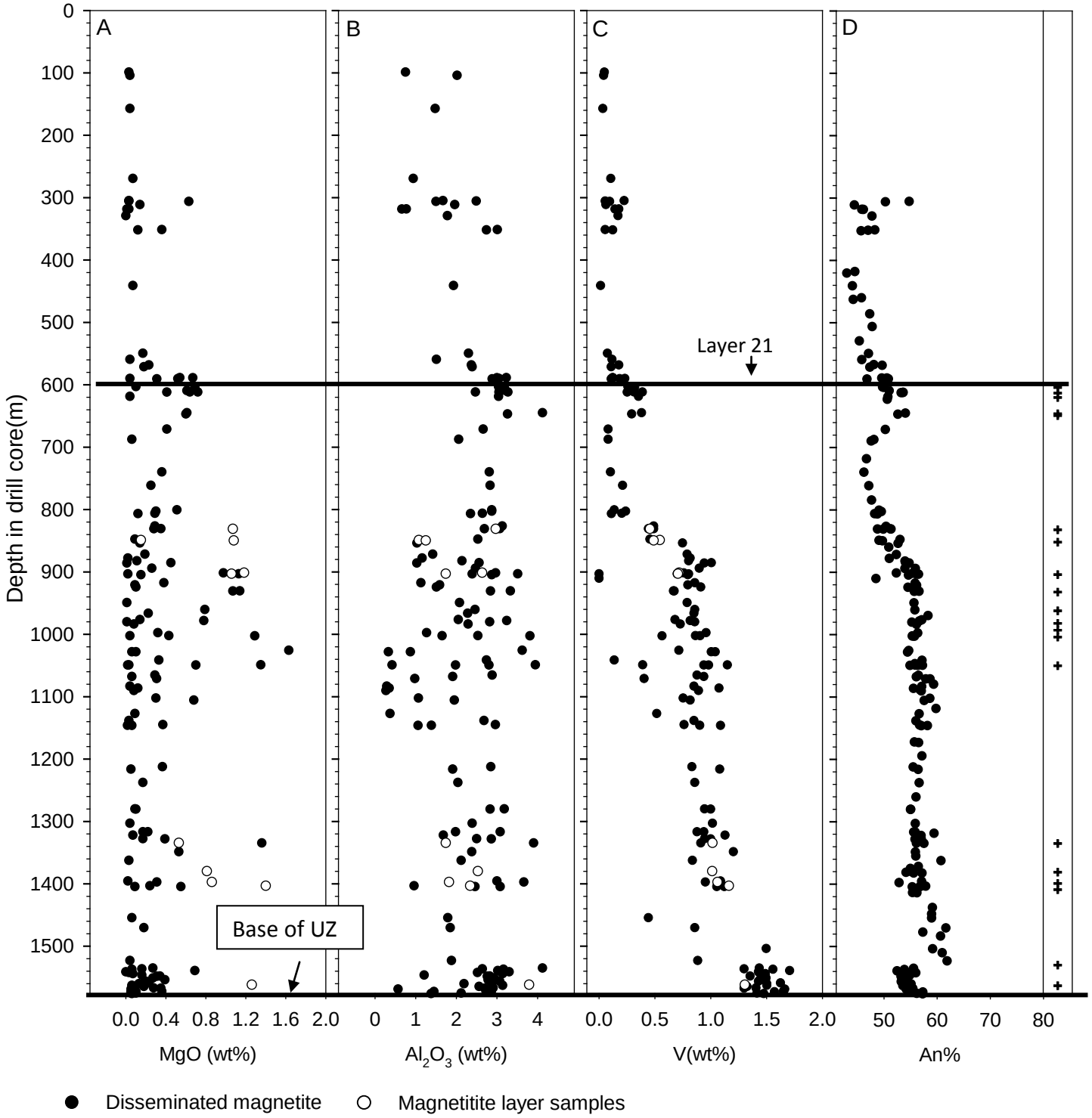

Fig. 4.18. Electron microprobe analyses of magnetite and plagioclase in BV-1 drill core. (A) MgO; (B) Al_2O_3 and (C) V in magnetite and (D) An% of plagioclase. Stratigraphic positions of magnetitite layers identified by Cawthorn and Ashwal (2009) are marked with crosses. Data from Ashwal et al. (2005).

Chapter 5 – Discussion

5.1. Disseminated Magnetite

Reynolds (1985b) documented small isolated olivine crystals within massive magnetitite layers of the UZ which were found to contain variable Mg-rich compositions reaching up to Fa_{46} and olivine within disseminated magnetite sections which were found to contain a lower Mg composition of Fa_{65}. He ascribed the differences in composition between the olivine in the massive magnetitite and disseminated magnetite to subsolidus re-equilibration. Subsolidus re-equilibration has been previously invoked by Hatton and Von Gruenewaldt (1985) to explain similar differences in composition between orthopyroxene and olivine hosted chromitite. They noted higher Mg content in massive chromitites compared to adjacent disseminated chromite. They suggested the difference to be a result of subsolidus re-equilibration of chromite with surrounding silicates. As the chromitite layers are essentially devoid of olivine and orthopyroxene, no subsolidus re-equilibration was possible. However, the adjacent disseminated chromite was able to re-equilibrate with surrounding silicates during subsolidus cooling.

Pyroxene and olivine are absent in the magnetitite layers investigated in the current study whereas the disseminated magnetite is in contact with these silicates. Figure 5.1 is a qualitative illustration of the behavior of Mg in magnetite during subsolidus cooling in the presence of pyroxene and olivine. The Quilf95 program developed by Andersen et al. (1993) is used to compute the values used to generate Figure 5.1. Traditionally, Quilf95 (using compositions of coexisting pyroxene, olivine, quartz and Fe-Ti oxides or pairs of these minerals from one specimen) is used to calculate temperature, fo_2 and pressure conditions under which minerals have formed. However, in this calculation Quilf95 is used to observe variations in Mg of magnetite as a function of temperature. Due to insufficient data from the BK drill core, no single specimen had all the required minerals therefore mineral data was collected from adjacent samples for the calculation. Quartz is absent in the UZ, however, using a phase assemblage olivine-pyroxene-magnetite-ilmenite QUILF geothero-oxybarometer can be used to calculate intensive parameters temperature, fo_2 and pressure (Lindsley et al., 1990; Andersen et al., 1993) and thus the absence of quartz need not affect the application of Quilf in this regard. The compositions of pyroxene, olivine and ilmentie are

kept constant and the composition magnetite is calculated for a range of temperatures (1 100-600°C) at 100°C increments. It can be seen in Figure 5.1 that the disseminated magnetite is progressively depleted in Mg with decreasing temperature. This serves to illustrate the possibility of re-equilibration as a mechanism to deplete the disseminated magnetite in Mg as compared to the magnetitite layers.

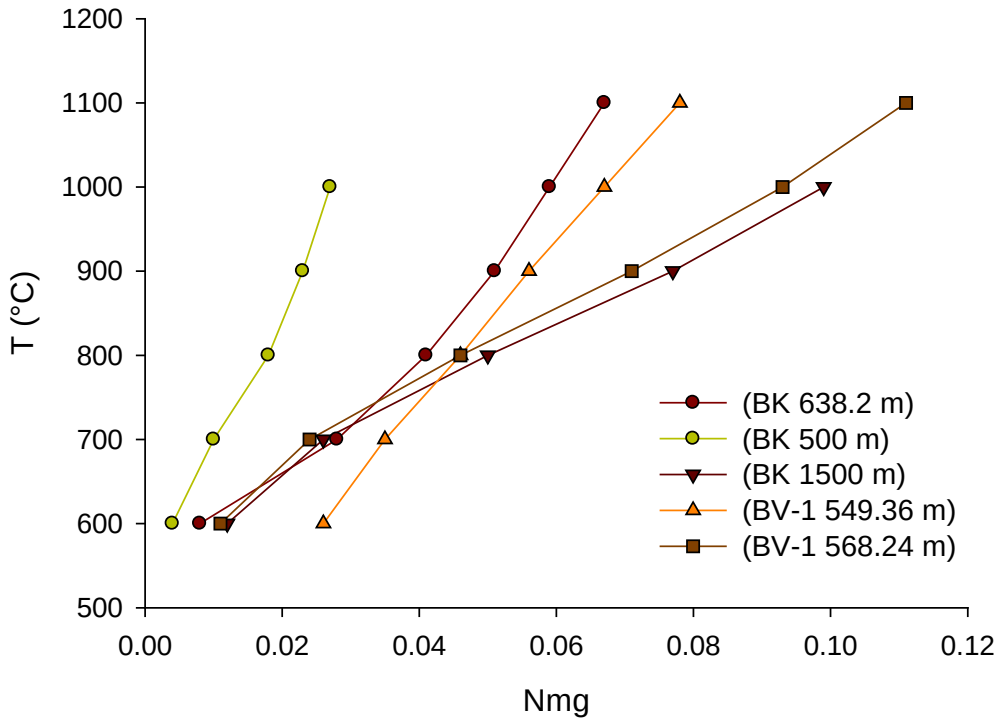

Fig. 5.1. Behavior of Mg in magnetite during subsolidus cooling with surrounding pyroxene. Nmg represents the mole% of Mg in magnetite. BK=Bierkraal drill core, BV-1=Bellevue drill core.

The MgO content of the lower magnetitite layers (UZ_a) in the BK drill core are higher than the adjacent disseminated magnetite. Al_2O_3 and V are higher in the magnetitite layers compared to disseminated magnetitite in the BK drill core (Table 4.2). Akin to the BK drill core, the magnetitite layers in the BV-1 drill core have a higher MgO content than adjacent disseminated magnetite. There is however, no difference between the magnetitite layers and adjacent disseminated magnetite in terms of V and Al_2O_3 (Fig. 4.18). It has been suggested that the degree of equilibration of both chromite and magnetite depends on the nature of the surrounding silicate and the modal amount of chromite and magnetite (Hatton and Von Gruenewaldt, 1985; Butcher and Merkle, 1987; Reynolds, 1985b). The proportion of mafics (pyroxene + olivine) and plagioclase to magnetite is plotted against MgO and Al_2O_3 for sections 800-1 000 m and 1 300-1 400 m in Figure 5.2. Magnetitite layers occur in these sections and thus were chosen to evaluate the effect of modal proportions on the composition

of the magnetite. The MgO content of magnetite decreases with increasing mafic/magnetite ratio with the magnetitite layers recording the highest MgO content along with a few disseminated magnetite samples (Figs. 5.2A, C). This trend is suggested to reflect the dependence of subsolidus re-equilibration on modal proportions of magnetite and surrounding mafic (pyroxene + olivine) minerals. The greater the amount of surrounding mafics to magnetite, the greater the degree of Mg-Fe exchange between magnetite and surrounding mafics. The Al_2O_3 content as well decreases with increasing plagioclase/magnetite ratio only in section 800-1 000 m. Section 1 300-1 400 m shows more of a scatter (Figs. 5.2B, D). Al_2O_3 content in the magnetitite layers shows a significant variation (1-3 wt%) and this could possibly be due to the amount of exsolved pleonaste in the magnetite. It is important to note the data discussed above, from the BV-1 drill core are from electron microprobe, not mineral separates. The effect of the exsolution phases on the composition of magnetite has been discussed in section 4.1.1. The Cr_2O_3 content of pyroxene through the BV-1 drill core are low ranging from 0-0.2 wt% and thus no significant variation caused by re-equilibration can be discerned. However, it is possible that some changes in Cr could have occurred, but it is unlikely to have been significant for the present database using mineral separates because there is almost no pyroxene in the magnetitite anorthosite associated with the MML. Therefore subsolidus re-equilibration with Mg-Fe exchange between disseminated magnetite and pyroxene and/or olivine is suggested to account for the difference in MgO between the magnetite from magnetitite layers and the disseminated magnetite.

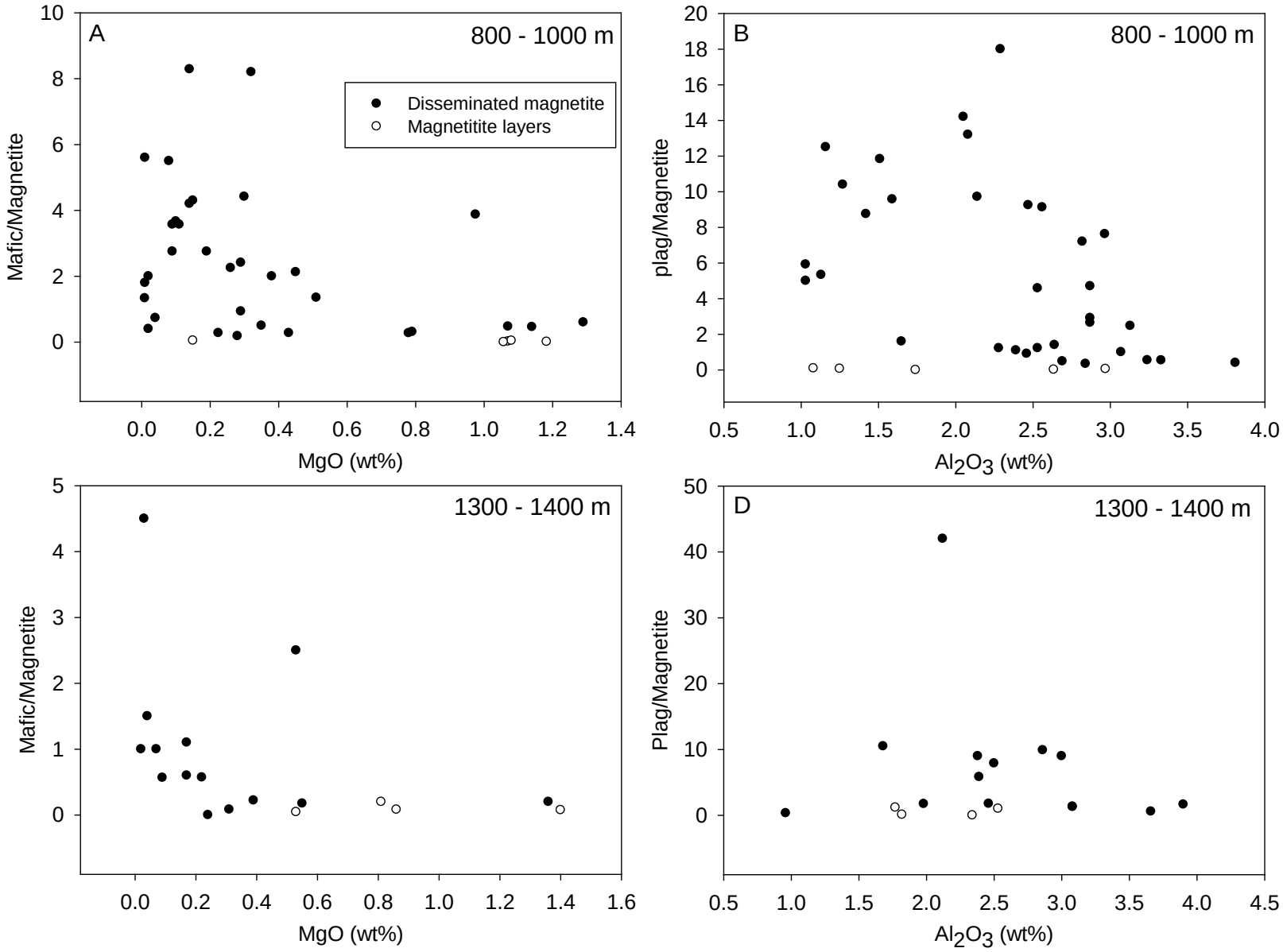

Fig. 5.2. Variation of MgO and Al_2O_3 content in magnetite against modal proportion of mafics (pyroxene + olivine) and plagioclase. Filled circles=disseminated magnetite, open circles=magnetitite layers samples. Data from Ashwal et al. (2005).

5.2. Possible Mechanisms of Formation for Fe-Ti Oxide Layers

The various proposed mechanisms by which magnetitite layers may have formed have been highlighted in chapter 1. The current data set allows some of the proposed mechanisms to be re-assessed along with some additional mechanisms.

5.2.1. Crystal Settling and Sorting

Crystal settling and gravity segregation involves the homogeneous crystallization of crystals in the magma chamber which subsequently settle to the floor of the magma chamber. The rate at which minerals settle to the floor in a Newtonian fluid as described by Stoke's Law (equation 5.1), chiefly depends on the size and density of the minerals as well as the magma viscosity.

Stoke's law is given by:

$$V = \frac{2gr^2(\rho_1 - \rho_2)}{9n} \qquad (5.1)$$

Where V is the velocity of a sphere,

r is the radius of the sphere,

ρ_1 is the density the sphere,

ρ_2 is the density of the Newtonian fluid,

n is the viscosity of the Newtonian fluid, and

g is the gravitational force.

For comparable size, the denser minerals will settle faster than less dense minerals resulting in a modally graded layer (Wager and Brown, 1968; Naslund and McBirney, 1996). The modal gradation from massive magnetitite into anorthosite observed in the MML and layer 1 (Fig. 2.1.1H) in Magnet Heights river section supports the contention that the magnetitite layers may have accumulated through crystal settling. Magnetite has a density of 5 g/cm^{-3} and grain sizes ranging between 0.1 and 2 mm whereas plagioclase has a lower density of 2.68 g/cm^{-3}. It is therefore possible that magnetite would have sunk more rapidly than plagioclase resulting in the observed gradational upper contacts. Moreover, the planar orientation of feldspar crystals toward the top of layer 1 (Fig. 2.1.1I) and the lower layers

(Fig. 2.3B) suggests that the feldspar accumulated through crystal settling (Brothers, 1964). During crystal settling the mixing of crystals homogenously nucleated at different times, may result in a randomly variable vertical Cr profile (Cawthorn, 1980). Cawthorn and McCarthy (1980, 1981) noted an upward depletion in Cr content in vertical profiles through the MML in Magnet Heights. Klemm et al. (1985) also noted a decrease in Cr content from 6 000 at the base to 200 ppm at the top of the MML in two of three vertical profiles through the MML collected north of Rossenekal. The vertical Cr profiles (Figs. 4.1; 4.4; 4.14) through the MML all show a systematic, exponential upward decrease in Cr and thus are unlikely to be produced by crystal settling. The magnetitite layers of the BC are essentially monomineralic with subordinate feldspar concentrated towards the top of the layers. Pyroxene has a density of 3.25 g/cm^{-3} intermediated between that of magnetite and plagioclase. If the magma was saturated in magnetite, pyroxene and plagioclase then, from a density point of view, the layers should be modally graded with magnetite at the base followed by pyroxene and plagioclase (Cawthorn and Ashwal, 2009). Therefore the absence of pyroxene in the magnetitite layers argues against crystal settling (Cawthorn et al. 2005, Cawthorn and Ashwal, 2009).

5.2.2. Magma Addition

As highlighted in Chapter 1, the introduction of a new magma into the magma chamber may result in the crystallization of magnetitite layers if the new magma was saturated in magnetite. Reversals in An% occur in the BK drill cores. If the reversals to higher An% represent the introduction of a new magma into the magma chamber which may result in the crystallization of magnetitite layers, magnetitite layers should be coincident with the reversals in An%. The most significant reversal in An%, just below layer 21, appears to be coincident with a cluster of magnetitite layers (Figs. 4.15C; 4.18D) suggesting magma addition may have played a role in the crystallization of the magnetitite layers. However, not all reversals in An% occur at the same stratigraphic positions of magnetitite layers (Fig. 4.15C). Furthermore, the An% through the first 700 m in the BV-1 drill core is fairly constant with no significant reversals and, magnetitite layers occur in this section of the drill core (Fig.4.18) showing no link between reversals in An% and positions of magnetitite layers. Moreover it has been documented that the An% below and above the MML and layer -3 remains constant (Cawthorn et al. 2005). Therefore magma addition as the main driving force for the crystallization of magnetitite layers seems unlikely.

5.2.3. Rhythmic Layering

Oscillatory crystallization about the cotectic of two minerals may result in rhythmic layering observed in LMI (Maaløe, 1978). A magma lying in the magnetite phase field may upon crystallization reach the magnetite-feldspar cotectic with a magnetite:feldspar ratio of 30:70 (Roeder and Osborn, 1966). McCarthy and Cawthorn (1983) documented four drill cores intersecting magnetite-rich sequence through the MML in Wapadskloof, south of Roossenekal. They observed magnetite to almost always be far in excess of the cotectic ratio with only a few sections approximating the 30:70 magnetite:feldspar ratio which led them to reject fractional crystallization as a mechanism to account for the plagioclase rich sections encountered in the sequence. Similarly, magnetite is always far in excess of the experimentally determined magnetite-feldspar cotectic ratio in the MML, particularly in the feldspar parting (Fig. 2.1.1D). Therefore a mechanism invoking oscillatory crystallization driven by fractional crystallization to account for the mineralogical changes observed in the MML seems unlikely.

5.2.4. Liquid Immiscibility

It has been highlighted in Chapter 1 that a magma may separate in to two conjugate liquids, one being Si-rich and the conjugate Fe-rich, if the composition of the magma is driven into the two liquid field (Philpotts, 1979; Charlier and Grove, 2012). It has been suggested that the magnetitite layers in the UZ may have crystallized from Fe-rich immiscible liquids which pond at the floor of the magma chamber (Bateman, 1951; Scoon and Mitchell, 1994). Channeled downward infiltration from the magnetitite layers along zones of weakness is suggested to account for discordant Fe-Ti oxide pipes located in the upper portions of the MZ and in the UZ (Scoon and Mitchell, 1994). The magnetitite layers are commonly underlain by anorthosite and thus downward percolation through the plagioclase mush would be expected as the Fe-rich immiscible liquid would have a low viscosity and high density (Cawthorn and Ashwal, 2009). The basal contacts of the MML and layer 1 with the underlying anorthosite are sharp and planar (Figs. 2.1.1B and H), arguing against the ponding such a liquid at the floor of the magma chamber. Thus the crystallization of magnetitite layers from an immiscible Fe-rich liquid seems unlikely.

5.2.5. Changes in Oxygen Fugacity

Klemm et al. (1985) noted differences in MgO, Al_2O_3, Cr_2O_3 and V_2O_3 between the disseminated magnetite and magnetitite layers and suggested that the magnetitite layers may have crystallized under higher fO_2 conditions than the adjacent disseminated magnetite. MgO, Al_2O_3, Cr_2O_3 were found to be higher in the magnetitite layers compared to the disseminated magnetite. The V_2O_3 content was however, found to be lower in the magnetitite layers compared to the disseminated magnetite. The partition coefficient of V into magnetite decreases with increasing fO_2 (Toplis and Corgne, 2002). Thus the lower V_2O_3 content observed in the magnetitite layers compared to the disseminated magnetite led Klemm et al. (1985) to the conclusion that the magnetitite layers crystallized under higher fO_2 compared to the disseminated magnetite. The BV-1, BK and UCAR mine drill cores comprise massive magnetitite layers as well as disseminated magnetite and thus provide suitable material to study processes affecting their compositions. Crystallization of the magnetitite layers under higher fO_2 conditions compared to the disseminated magnetite seems unlikely for the BV-1 drill core as no difference in V content between magnetitite layers and the disseminated magnetite is observed (Fig. 4.18C). The BK drill core (Table 4.2) also shows crystallization of magnetitite layers under higher fO_2 compared to disseminated magnetite to be an unlikely possibility as the V content of massive magnetitite layers is higher than the disseminated magnetite. Akin to the BK drill core, the UCAR mine drill core shows that the magnetitite layers have a higher V content than the disseminated magnetite (Fig. 4.14B) thus do not suggest higher fO_2 conditions during the crystallization of magnetitite layers. Howarth et al. (2013) suggested CO_2 degassing of the footwall carbonates as a mechanism to introduce oxygen into the magma chamber in order to change fO_2. The magnetitite layers of the BC are commonly underlain by anorthosite and thus a mechanism involving CO_2 degassing can be ruled out. Klemm et al. (1985) suggested volatile diffusion from underlying cumulates, however, the uniform introduction of oxygen into the magma chamber in order to produce such laterally extensive magnetitite layers seems implausible. The observed differences in MgO between magnetitite layers and disseminated magnetite may be attributed to modal mineralogy and re-equilibration as discussed in section 5.1 and not necessarily a change in fO_2.

5.2.6. In-situ Crystallization

A model for the in-situ crystallization of magnetitite layers in the UZ has been proposed by Cawthorn and McCarthy (1980, 1981). This model has been invoked to account for strong vertical Cr gradients of magnetite separates collected from several vertical profiles through the MML. Cr has a high partition coefficient for magnetite (D>200) (Irving, 1978) and thus the in-situ crystallization of magnetite from a thin boundary layer may deplete the boundary layer of Cr resulting in a upward decrease in the Cr content of crystallizing magnetite. *Intermittent* convection, however, may replenish the boundary layer bringing more primitive, undepleted magma from higher in the magma chamber into the crystallization zone resulting in higher Cr contents of newly crystallized magnetite. The magnitude of the reversal depends on the level from which the convection cell descends, with convection cells descending from higher levels in the magma chamber being more primitive than those descending from lower levels in the magma chamber. Moreover, a model involving in-situ crystallization has been proposed by Cawthorn (1994) who studied magnetite separates from several profiles along the base of the MML in Magnet Heights. Cawthorn (1994) noted several unusually high Cr concentrations and suggested these peak Cr concentrations to be the centers of growth nodes. In this model, magnetite is suggested to crystallize from a boundary layer initially as patches, randomly spaced out along the base of the magma chamber, which subsequently grow outwards along the base eventually creating the laterally continuous magnetitite layers. As the initial patches (growth nodes) are the first to crystallize, they crystallize from a fertile magma and locally deplete a boundary layer of magma in Cr. Later crystallizing magnetite forming the base of the magnetitite layer between the early growth nodes would subsequently crystallize from a partially depleted boundary layer of magma and thus have a lower Cr content than at the growth nodes. This would result in a profile along the base of magnetitite layers characterized by several peak concentrations in Cr at the growth nodes along with lower Cr content in between the growth nodes. The sample with an unusual high Cr content (17 000 ppm) observed along the 2 m spaced profile along the base of the MML (Fig. 4.7A) and the two samples with atypically high Cr content (3 200 and 3 800 ppm) at the base of layer 1 (Fig. 4.13) could possibly be accounted for by this in-situ crystallization model, with the high Cr content samples representing growth nodes. All the vertical profiles taken through the MML (Figs. 4.1; 4.4; 4.14) show an exponential upward decrease in Cr. This further suggests in-situ crystallization for the magnetitite layers.

However, this model does not obviously account for the modal upward increase in feldspar observed in the MML and layer 1 in Magnet Heights which is better explained by crystal settling. In-situ crystallization would result in randomly oriented crystal or crystals with crescumulate texture with crystals oriented perpendicular to the plane of layering.

Crystal settling and in-situ crystallization, however, need not be mutually exclusive (Morse, 1986; Campbell, 1978; Martin, 1990). Martin (1990) studied an aqueous solution of potassium nitrate and observed that upon cooling, the rate of cooling and viscosity of the liquid are the major factors controlling the type of crystallization i.e. homogenous or heterogeneous crystallization. Martin (1990) demonstrated that at slower cooling rates (low supercooling) in-situ crystallization is the only form of crystallization whereas at higher cooling rates (higher supercooling), in addition to in-situ crystallization, homogenous nucleation of crystals, which subsequently settle to the floor, also takes place. Possibly a change in supercooling conditions may account for in-situ crystallization (systematic upward decrease in Cr content of magnetite) and crystal settling (planar orientation of plagioclase crystals in the feldspar parting). A mechanism by which supercooling may be fluctuated as to induce both in-situ and homogeneous crystallization, however, cannot be discerned by the current data set.

5.2.7. Changes in Pressure

A change in pressure as a mechanism to produce magnetitite layers has been highlighted in Chapter 1. An increase in pressure may increase the stability fields of spinel and pyroxene fields at the expense of plagioclase and olivine (Osborn, 1978). A change in pressure would only change the stability fields of the respective minerals and not necessarily the chemistry of the crystallizing magma (Cawthorn and McCarthy, 1980). Therefore mineralogical changes need not be associated with reversals in Cr content in the massive magnetitite layers. Cawthorn and McCarthy (1980) documented vertical section with mineralogically heterogeneous sequence comprising five thin magnetitite layers and magnetite-rich anorthosite. They noted a systematic upward decrease, with no reversals, of Cr in magnetite mineral separates through the section. Moreover, Cawthorn and McCarthy (1981) observed that changes in Cr content and changes in mineralogy are not mutually influential in vertical sections through magnetitite layers in the UZ. The lack of chemical breaks in the vertical sections where thin magnetitite layers are present and the lack of correlation between changes

in mineralogy and reversals in Cr content led Cawthorn and McCarthy (1980, 1981) to conclude that the crystallization of magnetitite layers may be a result of a physical process such as a change in pressure rather than external chemical influence. None of the vertical profiles through the MML (1-4) show a reversal in Cr content immediately above the feldspar parting (Fig. 4.1). Furthermore, the detailed profiles taken through the feldspar parting (Fig. 4.3) show no discernible reversal in Cr content immediately above the feldspar parting. Tectonics as a mechanism to achieve changes in pressure has been suggested by Cawthorn and McCarthy (1980, 1981). It is therefore suggested that the change from the feldspar parting into massive magnetite above the feldspar paring may have been triggered by a physical process such as a change in pressure rather than a chemically controlled process.

5.2.8. Double-Diffusive Layer Mixing

As highlighted in chapter 1 the break down and mixing of discrete double-diffusive layers may result in reversals in Cr observed in the MML (Krugar and Smart, 1987). Harney et al. (1996) noted changes in Sr and Sr/Al_2O_3 ratio of plagioclase separates above and below the MML. Harney et al. (1996) suggested this to be evidence of double-diffusive layer mixing. The plagioclase analyses presented by Harney et al. (1996) are listed in Table 5.1. The average Al_2O_3 content of plagioclase up to 45 m below and above the MML is identical 29.76 and 29.50 wt% respectively. The average Sr content of plagioclase up to 45 m below the MML (427 ppm) is slightly lower than that up to 45 m above the MML (450 ppm). Sr is incompatible in magnetite and thus crystallization of the MML will result in an increase in Sr in the liquid. Crystallization of magnetite will not change the composition of the preceding and subsequent plagioclase and so its Al_2O_3 content would be constant. Once plagioclase crystallizes again above the MML this will result in the observed increase in Sr in plagioclase and thus a change in Sr/Al_2O_3 ratio. Therefore an increase in Sr and Sr/Al_2O_3 ratio at the level of the MML may be attributed to fractionation as opposed to mixing of double-diffusive layers proposed by Harney et al. (1996). If reversals in Cr content in the magnetitite layers are a result of the mixing of discrete double-diffusive layers, then reversals in Cr content ought to be present at about the same level in adjacent profiles. The correlation of the reversal in Cr above 70 cm in profile 1 and the reversal above 60 cm in the adjacent profile 2 (Fig. 4.1) may support the model proposed by Krugar and Smart (1987). The absence of Cr reversals in the other adjacent profiles 3-4 (Fig. 4.1) and profile J (Fig. 4.4) and the irregular

variation in Cr content in layer 1 (Figs. 4.11; 4.12), however, argues against the model presented by Krugar and Smart (1987).

Geochemical cycles in whole rock, olivine and pentlandite composition have been noted in the UZ (Merkle and Von Gruenewaldt, 1986). Some magnetitite layers were found to occur at the base of some of these compositional cycles and attributed to double-diffusive layer break down and mixing (Merkle and Von Gruenewaldt, 1986). Although it has not been shown that the mixing of magma may produce a magnetite saturated magma, Merkle and Von Gruenewaldt (1986) suggested that the magnetitite layers coincident with the base of the geochemical cycles may have a genetic link with magma mixing. Again the breakdown and mixing of double-diffusive layers should produce laterally homogeneous layers. The lateral heterogeneity marked by peak and trough concentrations in Cr observed in profiles along the base of the MML (Figs. 4.6; 4.7A) and layer 1 (Fig. 4.13) argue against the magnetitite layers having crystallized as a result of double-diffusive layer mixing. Only two of the eight fractionation cycle bases proposed by Tegner et al. (2006) are coincident with sharp increases in Cr content in magnetite (Fig. 4.15). As these postulated fractionation cycles represent the break down and mixing of double-diffusive layers, it can be concluded that the mixing of such layers is an unlikely mechanism for the crystallization of magnetitite layers as suggested by Harney et al. (1996). However, stratification and mixing within the magma chamber is not ruled out, merely not convincingly shown to be the main driving mechanism for magnetitite layer formation.

Table 5.1. Plagioclase Compositions Below and Above the Main Magnetitite Layer. Harney and Merkle (1996)

Sample	Height (m)	SiO_2	Al_2O_3	FeO	CaO	Na_2O	K_2O	Sr	Total
Z3/1	210	53.81	28.99	0.21	11.91	4.66	0.10	-	99.68
G566	210	-	-	-	-	-	-	440	-
G568	195	-	-	-	-	-	-	440	-
G649	125	53.68	28.36	0.33	11.97	4.45	0.47	448	99.26
25.91	61.64	54.48	28.81	0.24	11.07	5.04	0.15	-	99.79
56/57	44.2	55.23	28.61	0.30	11.37	4.89	0.31	-	100.71
G510	35	-	-	-	-	-	-	455	-
G509	10	-	-	-	-	-	-	451	-
G400	5	-	-	-	-	-	-	442	-
72/73	2.75	54.64	28.76	0.22	10.84	5.07	0.25	-	99.78
76/77	2.55	50.86	31.13	0.30	13.97	3.48	0.25	-	99.99
90/91	-1.55	53.69	29.19	0.41	12.15	4.54	0.11	-	100.09
G406	-10	-	-	-	-	-	-	431	-
U1A	-20	-	-	-	-	-	-	414	-
G612	-25	-	-	-	-	-	-	431	-
G407	-45	51.86	30.33	0.28	13.07	3.94	0.22	-	99.70
G407	-45	-	-	-	-	-	-	433	-
Z2	-80	-	-	-	-	-	-	387	-
G609	-110	-	-	-	-	-	-	458	-
G608	-125	52.33	30.14	0.32	13.07	3.95	0.12	234	99.93
G600	-295	-	-	-	-	-	-	432	-
G426	-825	-	-	-	-	-	-	437	-

Highlighted cells plagioclase composition up to 45 m below and above the MML

5.2.9. Magma Currents

As it has been highlighted in Chapter 1, unmixing of crystal slurries flowing from the margins to the centre of the BC has been suggested to account for the layering observed, with denser pyroxene and oxide primarily accumulated at the base of the crystal slurries and plagioclase separated to the top (Maier et al., 2013). The sorting of crystals during the flow of a turbidity current is controlled by the physical properties of the suspended material rather than chemistry of the particles being transported (Middleton, 1993). Therefore, sequences deposited as a result of unmixing and sorting during flow should show random variation in chemistry, as crystals nucleated at different times may have been mixed and subsequently deposited in the same location. The regular upward depletion in Cr content in vertical profiles through the MML (Figs. 4.1; 4.4; 4.14) is unlikely to be produced by any mechanism

involving crystal sorting. Therefore the formation of magnetitite layers as a result of unmixing form a crystal-laden slurry seems unlikely.

5.3.Feldspar Parting

5.3.1. Composite Magnetitite Layers

Magnetitite layer 1 has a sharp bottom contact with the underlying anorthosite and a gradational top contact characterized by an upward modal increase in feldspar into anorthosite (Fig. 2.1.1H). The lower part of the MML (Fig. 2.1.1D) shows some similarity to layer 1 with massive magnetite at the base with an upward modal increase in feldspar at the feldspar parting. However, rather than grade entirely into anorthosite, the top of the feldspar parting terminates with the deposition of massive magnetite which then subsequently grades into anorthosite. The similarity of the lower and upper portions of the MML with layer 1 may suggest that the MML is a composite layer comprising two magnetitite layers stacked on top of one another with the feldspar parting marking the boundary between the two layers. Pyroxene-enriched partings observed in some sections of chromitite layers from the CZ observed by Naldret et al. (2012) have been suggested to be a consequence of intermittent convection as the chromitite layers were crystallizing. During the crystallization of a chromitite layer from the basal layer of a density stratified magma chamber, convection within this layer keeps fertilizing the magma from which the chromitite was crystallizing thus creating the massive chromitite. During periods of no convection, orthopyroxene may join the crystallizing assemblage thus creating the 'parting' observed. As convection resumes again, it will once again fertilize the magma driving composition back into the chromite field so that massive chromitite would continue to crystallize. Perhaps the model envisaged by Naldret et al. (2012) may also explain the feldspar parting observed in the MML. It has been shown that a liquid lying within the magnetite field may reach the magnetite-feldspar cotectic as a result of continued crystallization (Roeder and Osborn, 1966). As it has been discussed in section 5.2.6, it is suggested that during the crystallization of magnetite the resumption of convection will bring more primitive, undepleted magma into the crystallization front resulting in a reversal in Cr. If then the model envisaged by Naldret et al. (2012) is to be applied to the MML, one should expect a reversal at the top of the feldspar parting. Cawthorn and McCarthy (1980) observed a reversal some distance above the feldspar parting which may suggest the resumption of convection after a period of no convection when feldspar joined the

crystallizing assemblage with magnetite at the feldspar parting. The original sample spacing by Cawthorn and McCarthy (1980) was quite wide, so the exact level at which the reversal occurred was not accurately constrained. Hence, more closely spaced sampling was undertaken here. None of the closely spaced vertical profiles (1-4; P) for Cr taken through the MML show reversals in Cr content immediately above the feldspar parting (Figs. 4.1; 4.3A). Furthermore, the detailed profiles (D1-D6) taken through the feldspar parting (Fig. 4.3B) also show no discernible reversal in Cr content immediately above the feldspar parting. The absence of reversals in Cr content immediately above the feldspar parting argues against the feldspar parting being the boundary between two discrete magnetitite layers stacked on top of one another. The lack of a reversal immediately above the feldspar parting is thus suggested to reflect a physical process such as a change in pressure which has the advantage of changing mineralogy without affecting the chemistry of the magma as discussed in section 5.2.7.

5.3.2. Dome Structure: Speculative Model

The dome structure in Magnet Heights (Figs. 2.1.1E, F) is an anomalous feature which may provide important insight into the crystallization of the MML. It is necessary to determine whether the dome structure was present before or formed during or after the crystallization of the MML. Associated with the footwall anorthosite of the dome structure are basalt fragments (Figs. 2.1.1E, G). Basalt fragments may have sunk from the roof and accumulated during the crystallization of the footwall anorthosite creating a local high (dome structure) before the crystallization of the MML. Alternatively, the dome structure may be a relict diapir-like body. During the crystallization the MML, the less dense unconsolidated footwall anorthosite may have risen in a diapir-like fashion and was preserved as the dome structure. The feldspar parting is truncated by the dome structure (Fig. 2.1.1F). The feldspar parting may have initially been present in all profiles G-J with the vertical Cr content in magnetite as shown in Fig. 5.3A but later removed in profiles H-J from the protruding high point of the dome structure if the dome structure was created during the crystallization of the MML. McBirney and Noyes (1979) postulated that the boundary layer may comprise two layers; a static zone in which most crystallization takes place and an interior zone, in between the static zone and the main magma body, characterized by laminar flow. They suggested that an overlap between the two zones may result in the scouring of the partly crystallized zone by current activity. It may be possible that up-doming may have created an overlap between the

two with the protruding high point of the dome overlapping into the interior zone where current activity could have removed the feldspar parting. If the feldspar parting was removed as a result of up-doming and current activity, later crystallizing, more Cr depleted, magnetite should crystallize directly above where the bottom of the feldspar parting was before it was removed by current activity. This would result in an abrupt decrease in Cr content of magnetite to below 1 300 ppm in profiles H-J at the same height (75-85 cm) as the feldspar parting in profile G (Figs. 5.3A, B). An abrupt decrease in Cr content is, however not observed in profiles H-J at the same height (75-85 cm) as the feldspar parting in profile G (Fig. 4.4) and thus the absence of the feldspar parting as a result of up-doming and current activity seems unlikely. The fact that basalt fragments are only observed within the footwall anorthosite creating the dome, suggests that the dome is a primary feature which was present before the crystallization of the MML.

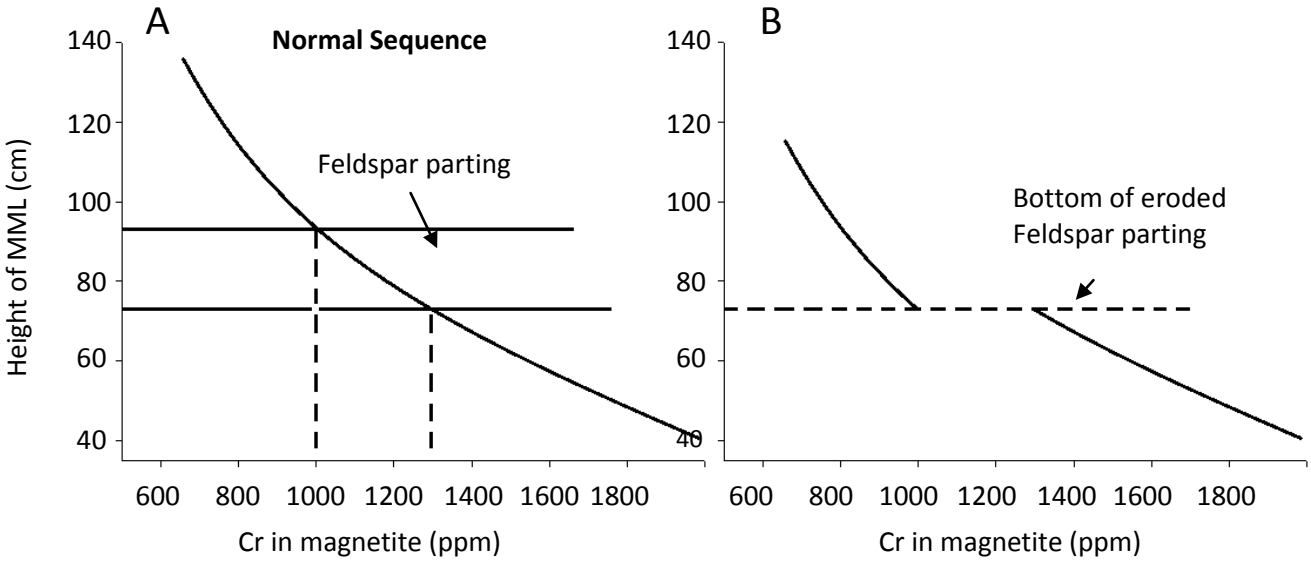

Fig. 5.3. Cr in magnetite as a result of feldspar parting removal. (A) Observed Cr concentration in magnetite from profile G. (B) Cr concentration in magnetite if parting was removed prior to accumulation of the upper succession.

Evidence for Small Scale Convection – The consequences for Cr in magnetite profiles G-J are now discussed within this context. The concept that there was intermittent convection on various scales was proposed by Cawthorn and McCarthy (1980, 1981) and further developed by Cawthorn et al. (1983); McCarthy et al. (1985) and Kruger and Smart (1987). The closely spaced (vertically and laterally) profiles G-J provide further evidence for this process. Within 10 cm vertically (25-35 cm) a reversal occurs in profile G (30 cm), H (35 cm) and I (25 cm) (Fig.4.4), because of vertical accuracy with which these samples have been taken these

reversals may possibly represent one event. A pronounced reversal of more than 1 000 ppm occurs at 25 cm in profile I. Profile G shows the smallest reversal, profile H shows a larger reversal than G and J no clear evidence of a reversal. This lateral variation can be attributed to a small convection cell having a width of chemical influence of only a few meters.

Absence of Feldspar Parting – The feldspar parting is only present in profile G and the Cr content of magnetite at the feldspar parting ranges from 1 300 ppm at the bottom to 1 000 ppm at the top of the feldspar parting (Fig. 4.4). The Cr content of magnetite in profiles H, I and J at same height (75-85 cm) as the feldspar parting in profile G, range from 1 800 ppm at the bottom to 1 300 ppm at the top (Fig. 4.4). It thus appears that in order for feldspar to crystallize, the Cr content of the magma must be such that the magnetite it produced contained only about 1 300 ppm. The absence of the feldspar parting in profiles H, I and J is suggested to be a consequence of magma not reaching the required composition for feldspar crystallization to occur above the dome (H, I, J) rather than the feldspar parting having been removed by up-doming and current activity.

Cr Content at the Base of the Crystallization Zone – Initially, a homogeneous magma will have a homogeneous concentration profile with no Cr gradient present in the liquid (Fig. 5.4). Diffusion controlled crystallization of 20-25 cm of magnetite from a thin boundary layer will deplete the boundary layer in Cr near the base resulting in a vertical Cr profile in the liquid and resultant magnetite as that depicted in Figure 5.4A (long dashed line). *Intermittent* convection cell activity on various scales and penetration depth can bring more primitive, undepleted magma from higher in the magma chamber into the crystallization zone to some level above the stagnant zone above the crystal-liquid interface resulting in a vertical Cr profile in the liquid such as Figure 5.4B (dashed line). Rapid diffusion of Cr, as a consequence of a very steep concentration profile, will occur resulting in a vertical Cr profile in the liquid and resultant Cr in magnetite such as Figure 5.4C (solid line). Magnetite crystallizing on the dome (H, I and J) will be closer to the penetration level (than at G) and will have higher Cr contents, as a consequence of higher diffusion rates of Cr, compared to magnetite crystallizing simultaneously off the dome and so further away from the level of penetration (slower diffusion rates). The irregularity created by the dome structure results in magnetite above the dome (H, I and J) crystallizing higher in the chemically zoned boundary layer than magnetite adjacent to the dome (at G) (Fig. 5.4D). Magnetite crystallization at different levels in this boundary zone should have different Cr contents as a result of different

diffusion rates of Cr with point J, closest to the level of penetration, recording the highest Cr concentration and greatest reversal; profile G, furthest away from height of penetration, recording the lowest Cr concentration and smallest reversal and profiles H and I recording intermediate Cr concentrations and reversals.

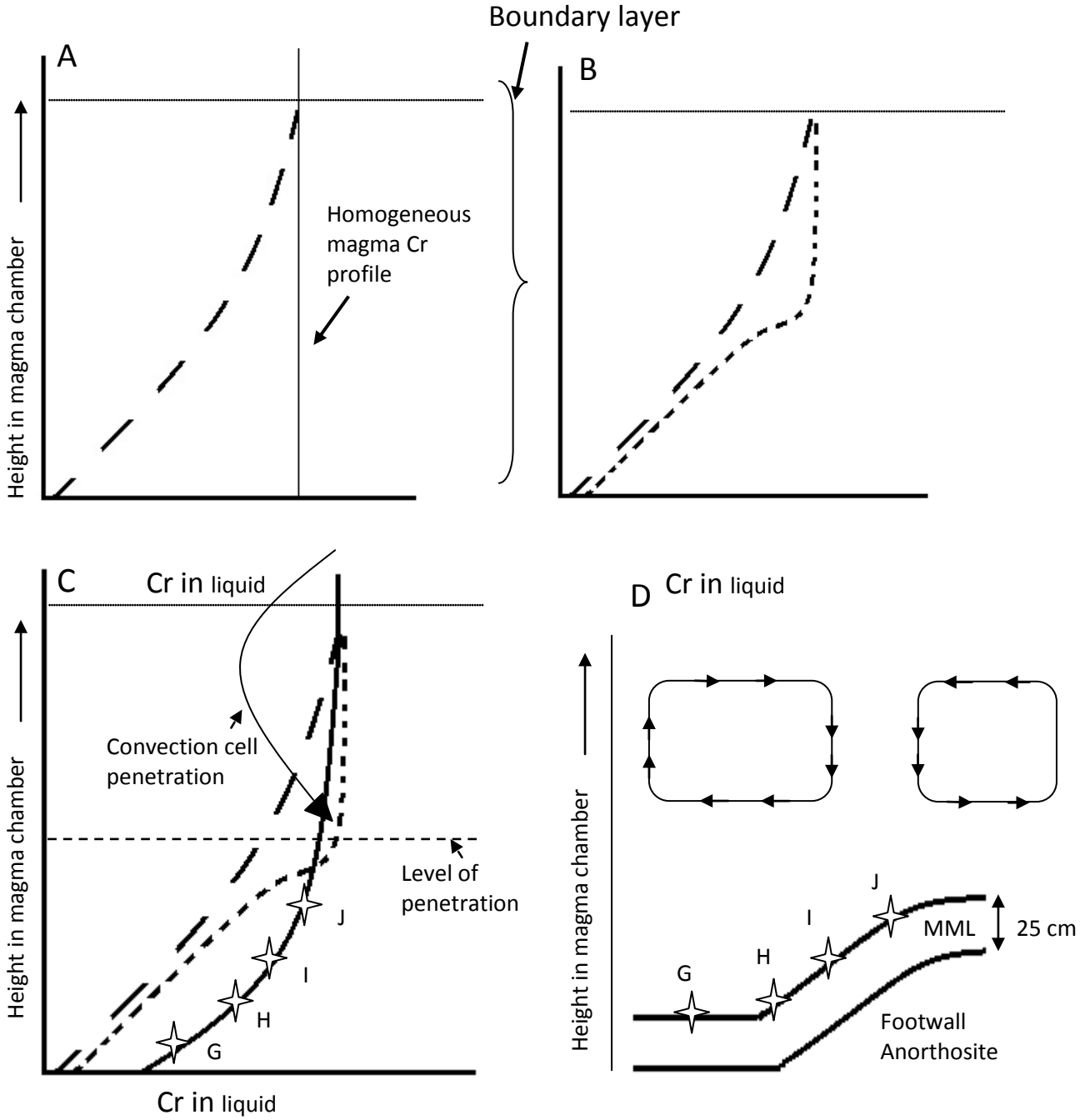

Fig. 5.4. Dome structure: speculative model. (A)Initial homogeneous Cr profile in liquid (thin solid line). After 20-25 cm of magnetite crystallization, Cr gradient (long dashed) develops in liquid prior to intermittent convection cell activity during the crystallization of the MML. (B) Cr concentration in liquid immediately after intermittent convection cell activity penetration (short dashed line). (C) Cr concentration in liquid after intermittent convection cell penetration as a result of rapid diffusion because of very steep concentration profile (bold solid line). (D) MML at dome structure doming up into boundary layer resulting in magnetite in profiles G, H, I and J crystallizing at different depths in boundary layer.

Profile I shows the largest reversal (5 500-7 400 ppm), profile H shows an intermediate reversal (4 400-5 100 ppm) and profile G shows the smallest reversal (2 800-3 000 ppm). The Cr content of profiles H and I, situated above the dome, are higher than that of profile G, situated adjacent to the dome (Fig. 5.5). This data fits well with the suggested model of diffusion controlled bottom crystallization and intermittent convection cells. Profile J, however, deviates from the suggested model, recording the lowest Cr content and no reversals are present in this profile (Fig. 5.5) and thus requires special attention. It may be possible that profile J is situated between two convection cells, an area which may not have been replenished in Cr by one of the intermittent convection cells (Fig. 5.4D) and thus the Cr content will not have been elevated.

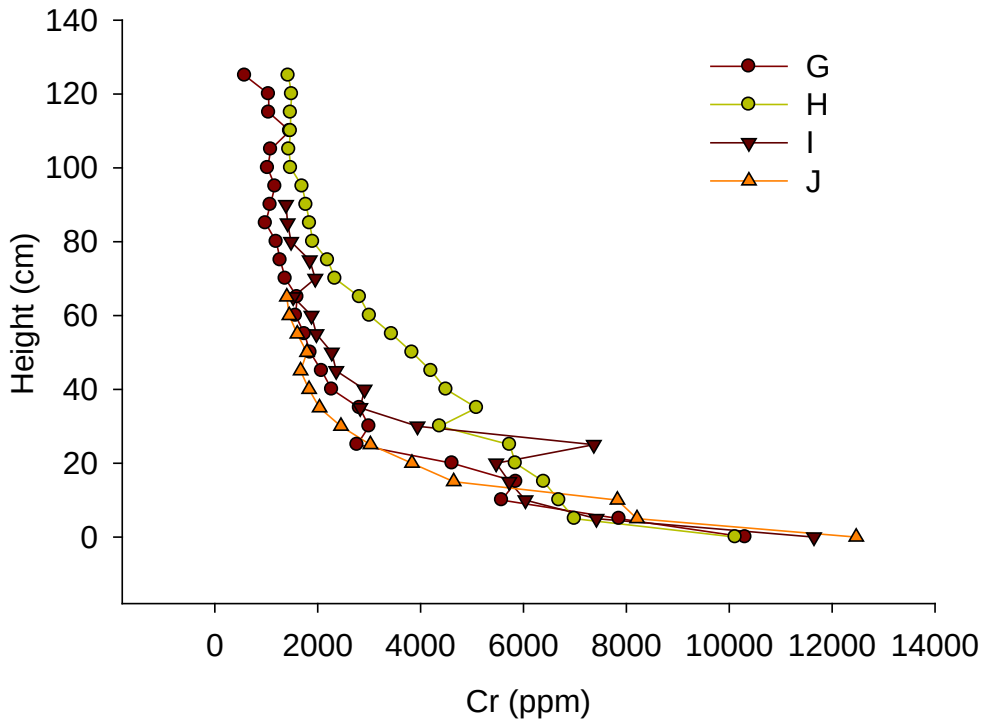

Fig. 5.5. Cr in magnetite for vertical profiles G, H, I and J at the dome structure.

5.4. Infiltration Metasomatism

The profiles taken in the normal section and above the impermeable xenolith (Fig. 3.5) show an upward increase in V content at the base of layer 1 (Figs. 4.11; 4.12). These observed trends are however opposite to normal fractionation processes. Infiltration metasomatism whereby interstitial liquid is pressed into the overlying cumulates during solidification of the underlying cumulates has been proposed as a mechanism that can alter the original composition of the overlying cumulates (Irvine, 1980). The overlying cumulates can react with the upward migrating liquid (Irvine, 1980). Irvine (1980) suggested the effects of infiltration metasomatism to be trends opposite from normal fractionation such as those observed at the base of layer 1. If there was an interaction between the basal samples and any upward migrating liquid, trends opposite to those of fractionation ought to be observed in the normal section only and not above the impermeable xenolith as the xenolith would locally prevent any upward migrating liquid from interacting with layer 1 (Cawthorn and Street, 1994). The observation that the profiles above the xenolith and the normal section show similar trends argues against infiltration metasomatism as a mechanism to account for the trends observed in layer 1 (Cawthorn and Street, 1994). Similarly upward migrating liquids can affect the composition of Cr. The basal samples from the normal section and the section above the xenolith show comparable compositions ranging between 2 100 to 2 700 ppm (Fig. 4.13). The current data also shows that a process of infiltration metasomatism is unlikely to have altered the composition of the basal samples in layer 1. An increase in Cr over the first 10 cm from the base of the MML is noted in one of the vertical profiles through the MML (profile 1) (Fig. 4.1). As mentioned such a trend opposite to normal fractionation is suggested to be an effect of infiltration metasomatism. Furthermore, one sample in the 2 m spaced profile along the base of the MML (profile B), shows an unusually low Cr content (Fig. 4.7A) which may suggest infiltration metasomatism. As there is no section along the MML which is underlain by an impermeable entity, a similar test for infiltration metasomatism applied to the MML is not possible. It is therefore possible that the upward increase in Cr observed in vertical profile 1 and the sample with unusually low Cr content in the 2 m spaced profile along the base may have been affected by infiltration metasomatism.

5.5. Magnetitite Bifurcations

Chromitite and magnetitite layers (Fig. 2.1.2) have been documented to split (bifurcate) into thinner layers (Hammerbeck, 1970; Maier and Brown, 1996; Nex, 2004; Cawthorn, 2003; Maier et al., 2013). One spectacular example of bifurcations can be observed in Dwars River locality where UG1 chromitite bifurcates into several thinner chromitite stringers. The mineralogy of the material separating the bifurcations is commonly the same mineralogy as that of the foot- and hangingwall of the oxide layers (Cawthorn, 2003). Nex (2004) observed a symmetrical disposition of chromitite bifurcations around several dome structures in Dwars River similar to textures observed around sand volcanoes. From these observations Nex (2004) suggested a mechanism analogous with the formation of sand volcanoes to explain the origin of chromitite bifurcations. It is suggested that liquefaction of the unconsolidated anorthosite footwall of UG1, as a consequence of seismic activity, resulted in the development of a plagioclase-rich slurry which was subsequently transported through the chromite 'sediment' and erupted at the crystal-liquid interface in a similar fashion as a sand volcano. The deposition of chromite crystals during the extrusion of the slurry resulted in the observed symmetrical disposition of chromitite bifurcations with respect to the dome structures. Possibly magnetitite bifurcations may have a similar origin. However, no dome structures occur in the vicinity of the observed magnetitite bifurcations and thus the model envisaged by Nex (2004) seems unlikely for the magnetitite bifurcations.

Cawthorn (2003) suggested silicate material may accumulate on a previously crystallized oxide layer in two possible processes. If the chief mechanism by which crystallization takes place is by in-situ crystallization, then silicate material may nucleate initially as growth nodes as suggested by Cawthorn (1994). However, instead of coalescing to form a continuous layer, the crystallization of the silicate layer is terminated by crystallization of a second oxide layer leaving a silicate lens in between two 'merged' oxide layers. Alternatively, if homogeneous nucleation is the dominant crystallization mechanism, convection may force low-density silicate material down to accumulate on top of a previously crystallized oxide layer. The silicate material will accumulate primarily at the locations which are beneath the descending limbs of convection cells thus creating localised accumulation of silicate material. Again the crystallization of an oxide layer terminates the accumulation of the silicate material trapping the silicate material within two oxide layers which may appear to be 'merged' where silicate material did not accumulate. Magnetitite layers are typically characterised by higher Cr

content than disseminated magnetite in the footwall and hanging wall anorthosite. If the model envisaged by Cawthorn (2003) is to be applied to magnetitite bifurcations, then a reversal in Cr should be expected at the base of magnetitite bifurcations overlying trapped silicate lenses and at some level within the 'merged' magnetitite layer. Reversals at the base of the MML sub-layers do occur (Fig. 4.10A). However, as no reversal in Cr occurs above the feldspar parting, the MML is unlikely to be a composite layer as discussed in section 5.3.1. Furthermore a reversals in Cr cannot be traced laterally along the 'merged' magnetitite layer with two (SL2; SL4) of the five vertical profiles (Fig. 4.9) through the MML in the vicinity of the bifurcations showing a reversal in Cr content thus suggesting the MML is not a composite 'merged' layer. Therefore the model suggested by Cawthorn (2003) seems unlikely as applied to magnetitite bifurcations. The upward increase in Cr content noted at the base of profile SL10 (Fig. 4.10) may be a result of infiltration metasomatism as discussed in section 5.4.

No tenable mechanism for the formation of the magnetitite bifurcations can be discerned through trends of Cr in magnetite. It is however, evident that the magma crystallizing the MML was laterally inhomogeneous as evidenced by the typical Cr content of the MML in the vicinity of the bifurcations (7 800-5 300 ppm) being half of that of the normal MML in Magnet Heights and the UCAR mine drill core (12 000 ppm).

5.6. Lateral Continuity of the Upper Zone Magnetitite Layers

Several similarities and differences between magnetitite layers in the eastern, western and northern lobes of the BC have been documented (Willemse, 1969; Von Gruenewaldt, 1973; Molyneux, 1974; van der Merwe, 1978; Ashwal et al., 2005; Tegner et al., 2006). Van der Merwe (1976) noted twenty magnetitite layers in the northern lobe with TiO_2 and V_2O_5 content comparable to those observed by Willemse (1969) in the eastern lobe. Based on field relations, the 32 magnetitite layers observed in the BV-1 drill core were correlated by Ashwal et al. (2005) with the magnetitite layers observed by van der Merwe (1976). The thickness of the MML in Magnet Heights and the UCAR mine drill core is comparable (±2 m) with the thickness noted by Tegner et al. (2006) in the BK drill core and Cawthorn and Ashwal (2009) in the BV-1 drill core (±2 m). There are, however notable differences particularly in the thickness of the thickest magnetitite layer, layer 21. Ashwal et al. (2005) documented layer 21 to be 13 m thick in the BV-1 drill core whereas Tegner et al. (2006) documented layer 21

to be 7 m in the BK drill core. Detailed vertical profiles through the MML in Magnet Heights and the UCAR drill core show comparable Cr contents (Figs 4.1; 4.14). Samples from the MML from Magnet Heights, Bierkraal, UCAR mine and Bellevue drill cores all show comparable V content values ranging between 1.16 and 1.3 wt%.

Both the BK and BV-1 drill cores show a decrease in V content in magnetite from base of the UZ to just below layer 21 with the BV-1 drill core having higher V content (1.5-0.75 wt%) than the Bk drill core (1.2-0.07 wt%) (Figs 4.15B; 4.18C). Above layer 21 the BK drill core shows reversals in V content whereas the BV-1 has less V content data above layer 21 and thus the possibility of such reversals occurring in the in this section of the BV-1 drill core cannot be ruled out. Throughout the BK drill core several reversals in plagioclase composition (An%) are observed (Fig. 4.15C), whereas in the BV-1 drill core reversals in An% are only observed above layer 21 with samples below layer 21 (first 700 m in BV-1) showing constant An% (Fig. 4.18D). One major reversal in An% of and V content occurs in both drill cores midway through the drill cores just below the layer 21. From the geochemical similarities discussed above it appears that the different lobes of the BC may be interconnected. Cawthorn and Webb (2001) noted petrological similarities in mafic sequences of the eastern and western lobes. Furthermore they showed that the geophysical gravity profile across the BC best fits a model involving the subsidence of a continuous BC as a result of isostatic readjustment as opposed to a model comprising two disconnected lobes suggested by Meyer and De Beer (1987). From the field relations and geophysical gravity profile, Cawthorn and Webb (2001) suggested that the eastern and western lobes of the BC may be connected. Therefore the geochemical similarities of magnetite between the different lobes mentioned above may support the suggestion that the lobes of the BC may be connected at depth.

Chapter 6 – Conclusions

The geochemistry, particularly Cr, of magnetite separates collected from the Main Magnetitite Layer (MML), Bierkraal, and UCAR mine drill cores and electron microprobe data from the BV-1 drill core allow for a comprehensive evaluation of the genesis of Fe-Ti oxides layers commonly found in large mafic intrusions (LMI).

Vertical Cr profiles through the MML all show exponential upward Cr depletion trends consistent with diffusion controlled bottom crystallization proposed by Cawthorn and McCarthy (1980, 1981). The MML is not completely homogeneous as shown by reversals, of different magnitudes in Cr content in five of the eight vertical profiles through the MML. The majority of the reversals cannot be correlated in adjacent profiles. Reversals of different magnitudes at the same level are noted in adjacent profiles at the dome structure. The reversals in Cr content are attributed to intermittent convection on varying scales bringing more primitive, undepleted magma into the crystallization front. Profiles taken at the dome structure suggest that the magnitude of the reversal depends upon both the level from which the convection cell is descending in the magma chamber and the level at which magnetite is crystallizing. Magnetite crystallizing closer to the level of penetration of the convection cell will record greater magnitude reversals whereas magnetite crystallizing further away from the level of penetration will record smaller Cr reversals. Heterogeneity is also noted along the base of the MML in the form of peak Cr concentrations variably spaced across the base of the MML. The peak Cr concentrations are attributed to heterogeneous nucleation of the MML along the base as suggested by Cawthorn (1994). The gradational tops of the magnetitite layers show preferentially oriented feldspar crystals oriented parallel to layering which may suggest crystal settling. Therefore, neither diffusion controlled bottom crystallization nor crystal settling, can account for all the features observed in the magnetitite layers of the UZ.

Profiles through the feldspar parting, a 10 cm thick horizon located midway through the MML, show no chemical break in Cr content immediately above the feldspar parting suggesting a physical process such as a change in pressure must have been involved to change the mineralogy from feldspar, in the feldspar parting, to massive magnetitite in the upper portion of the MML without altering the chemistry of the magma. Furthermore, the lack of a chemical break immediately above the feldspar parting argues against the MML

being a composite layer comprising two magnetitite layers with the feldspar parting as the boundary between the two layers as suggested by Naldret et al. (2012) for some chromitite layers in the Bushveld Complex. The absence of the feldspar parting in profiles above the dome structure compared to profiles adjacent to the dome structure may suggest a chemical control on the crystallization of the feldspar parting with the magma needing to attain a certain composition before feldspar can crystallize.

Massive magnetitite layers from the lower parts of the BK drill core (UZ_a) and magnetitite layers from the BV-1 drill core show higher MgO contents than adjacent disseminated magnetite. Quilf95 modelling qualitatively shows that Mg content of disseminated magnetite, in contact with pyroxene and/or olivine, is a function of temperature, decreasing with decreasing temperature. Modal mineralogy also has an effect on the composition of disseminated magnetite with an increase in mafic/magnetite ratio accompanied by a decrease in MgO content of disseminated magnetite. The similarity of V content of magnetitite layers and disseminated magnetite in the BK, UCAR and BV-1 drill cores is inconsistent with models involving a change in fo_2 as a mechanism to induce the crystallization of magnetitite layers. Therefore it can be concluded that differences in MgO in magnetite between the magnetitite layers and disseminated magnetite is a result of Fe-Mg exchange between magnetite and silicates (pyroxene and/or olivine) during subsolidus cooling rather than a change in fo_2.

The geochemical similarities between the MML (eastern lobe); UCAR mine (western lobe); Bierkraal (western lobe) and Bellevue (northern lobe) drill cores suggest that the different lobes of the BC may be connected.

References

Andersen, D.J., Lindsley, D.H. & Davidson, P.M. (1993). Quilf: A pascal program to assess equilibria among Fe-Mg-Mn-Ti oxides, pyroxenes, olivine and Quarts. *Computers & Geosciences*. 19, p1333-1350.

Ashwal, L. D., Webb, S.J. & Knoper, M.W. (2005). Magmatic stratigraphy in the Bushveld Northern lobe: continuous geophysical and mineralogical data from 2950m Bellevue drill core. *South African Journal of Geology*. 108, p199-232.

Bai, Z.J., Zhong, H., Naldrett, A.J., Zhu, W.G. & Xu, G.W. (2012). Whole-rock and mineral composition constraints on the genesis of the giant Hongge Fe-Ti-V oxide deposit in the Emeishan Large Igneous Province, Southwest China. *Economic Geology*. 107, p9507-524.

Balan, E., De Villiers, J.P.R., Eeckhout, S.G., Glatzel, P., Toplis, M.J., Fritsch E., Allard, T., Galoisy, L. & Calas, G. (2006). The oxidation state of vanadium in titanomagnetite from layered basic intrusions. *American Mineralogist*. 91, p953-956.

Bateman, A.M. (1951). The formation of late magmatic oxide ores. *Economic Geology*. 46, p404-426.

Boorman, S., Boudreau, A. & Kruger, F.J. (2004). The Lower zone – Critical zone transition of the Bushveld Complex: A quantitative textural study. *Journal of Petrology*. 45, p1209-1235.

Brothers, R.N. (1964). Petrofabric analyses of Rhum and Skaergaard Layered rocks. *Journal of Petrology*. 5, p225-274.

Buddington, A.F. & Lindsley, D.H. (1964). Iron-Titanium minerals and synthetic equivalents. *Journal of Petrology*. 5, p310-357.

Butcher, A.R. & Merkle, R.K.W. (1987). Postcumulus modification of magnetite grains in the Upper Zone of the Bushveld Complex, South Africa. *Lithos*. 20, p247-260.

Campbell, I.H. (1978). Some problems with the cumulus theory. *Lithos*. 11, p311-323.

Campbell, I.H., Naldrett, A.J. & Barnes, S.J. (1983). A model for the origin of the platinum-rich sulphide horizon in the Bushveld and Stillwater Complexes. *Journal of Petrology*. 24, p133-165.

Cameron, E.N. (1978). The Lower Zone of the eastern Bushveld Complex in the Olifants river trough. *Journal of Petrology*. 19, p437-462.

Carmichael, L.S.E. (1967). The iron-titanium oxides of salic volcanic rocks and their associated ferromagnesian silicates. *Contributions to Mineralogy and Petrology*. 14, p36-64.

Cawthorn, R.G, McCarthy, T.S. & Davis, G. (1983). Vertical gradients in a single grain of magnetite from the Bushveld Complex, South Africa. *Mineralogical Magazine*. 47, p27-34.

Cawthorn, R.G. & Ashwal, L.D. (2009). Origin of anorthosite and magnetitite layers in the Bushveld Complex, constrained by major element compositions of plagioclase. *Journal of Petrology*. 50, p1607-1637.

Cawthorn, R.G. & McCarthy, T.S. (1980). Variations in Cr content of magnetite from the Upper zone of the Bushveld Complex – Evidence for heterogeneity and convection currents in magma chambers. *Earth and planetary Science Letters*. 46, p335-343.

Cawthorn, R.G. & McCarthy, T.S. (1981). Bottom crystallization and diffusion control in layered complexes: Evidence from Cr distribution in magnetite from the Bushveld Complex. *Transactions Geological Society of South Africa*. 84, p41-50.

Cawthorn, R.G. & Street, J. (1994). Vertical migration of residual magma in the Upper Zone of the Bushveld Complex. *Mineralogy and Petrology*. 51, p345-354.

Cawthorn, R.G. & Walraven, F. (1998). Emplacement and crystallization time for the Bushveld Complex. *Journal of Petrology*. 39, p1669-1687.

Cawthorn, R.G. & Webb, S.J. (2001). Connectivity between the western and eastern limbs of the Bushveld Complex. *Tectonophysics*. 330, p195-209.

Cawthorn, R.G. (2003). Genesis of magmatic oxide deposits – A view from the Bushveld Complex. *Norges Geologiske Undersøkelse Special Publication*. 9, p11-21.

Cawthorn, R.G. (1994). Growth nodes at the base of magnetite layers in the Upper zone of the Bushveld Complex. *South African Journal of Geology*. 97, p455-461.

Cawthorn, R.G. (1999). The platinum and palladium resources of the Bushveld Complex. *South African Journal of Science*. 95, p481-489.

Cawthorn, R.G. (2007). Cr and Sr: Keys to parental magmas and processes in the Bushveld Complex, South Africa. *Lithos*. 95, p381-398.

Cawthorn, R.G. (2013). The residual or roof zone of the Bushveld Complex, South Africa. *Journal of Petrology*. 54, p1875-1900.

Cawthorn, R.G., Barnes, S.J., Balhaus, C. & Malich, K.N. (2005). Platinum-group element, chromium and vanadium deposits in mafic and ultramafic rocks. *Economic geology 100th anniversary volume*, p215-249.

Cawthorn, R.G., Eales, H.V., Walraven, F., Uken, R. & Watkeys, M.K. (2006). The Bushveld Complex. In: Johnson, M.R, Anhaeusser C.R, and Thomas, R.J. (eds). *The Geology of South Africa*. Geological Society of South Africa, Johannesburg/Council for Geoscience, p261-281.

Charlier, B. & Grove, T.L. (2012). Experiments on liquid immiscibility along tholeiitic liquid of descent. *Contributions to Mineralogy and Petrology*. 164, p27-44.

Chen, W.T., Zhou, M. & Zhao, T. (2013). Differentiation of nelsonitic magmas in the formation of the ~1.74 Ga Damio Fe-Ti-P ore deposit, North China. *Contributions to Mineralogy and Petrology*. 165, p1341-1362.

Dare, S.A.S., Barnes, S.J. Beaudoin, G. (2014). Trace elements in magnetite as petrogenetic indicators. *Mineralium Deposita*. 49, p785-796.

Dare, S.A.S., Barnes, S.J., Beaudoin, G. (2012). Variation in trace element content of magnetite crystallized from a fractionating sulfide liquid, Sudbury, Canada: Implications for provenance discrimination. *Geochimica et Cosmochimica Acta.* 88, p27-50.

Duchesne, J.C. (1972). Iron-Titanium oxide minerals in the Bjerkrem-Sogndal Massif, south-western Norway. *Journal of Petrology*. 13, p57-81.

Duchesne, J.C., Shumlyanskyy, L. & Charlier, B. (2006). The Fedorivka layered intrusion (Korosten Pluton, Ukraine): An example of highly differentiated ferrobasaltic evolution. *Lithos*. 89, p353-376.

Dymek, R.F. & Owens, B.E. (2001). Petrogenesis of apatite-rich rocks (nelsonites and oxide-apatite gabbronorites) associated with massif anorthosites. *Economic Geology*. 96, p797-815.

Hall, A.L. (1932). *The Bushveld Igneous Complex of the central Transvaal*, Pretoria: Geological Survey of South Africa, Government Printer, 560p.

Hammerbeck, E.C.I. (1970). The Steelpoort Granite, eastern part of the Bushveld Complex and the magnetitite in the gabbroic country rock. *Geological Society of South Africa Special Publication*. 1, p299-311.

Harney, D.M.W. & Merkle, R.K.W. (1992). Sulfide mineralogy at the main magnetitite layer, Upper Zone eastern Bushveld Complex, and the effect of hydrothermal processes on pentlandite composition. *European Journal of Mineralogy*. 4, p557-569.

Harney, D.M.W., Von Gruenewaldt, G. & Merkle, R.K.W. (1996). The use of plagioclase composition as an indicator of magmatic processes in the Upper zone of the Bushveld Complex. *Mineralogy and Petrology*. 56, p91-103.

Harney, M.W. & Von Gruenewaldt, G. (1995). Ore-forming processes in the upper part of the Bushveld Complex, South Africa. *Journal of African Earth Sciences*. 20, p77-89.

Hill, R.L. & Sack, R.O. (1987). Thermodynamic properties of Fe-Mg titaniferous magnetite spinels. *Canadian Mineralogist*. 25, p443-464.

Howarth, G.H., Prevec, S.A. & Zhou, M. (2013). Timing of Ti-magnetite crystallization and silicate disequilibrium in the Panzhihua Mafic Layered Intrusion: Implications for ore-forming processes. *Lithos*. 170, p73-89.

Huppert, H.E. (1984). Double-diffusive convection due to crystallization in magmas. *Annual Review of Earth and Planetary Sciences*. 12, p11-37.

Irvine, T.N. (1977) Origin of chromite layers in the Muskox intrusion and other stratiform intrusions: a new interpretation. *Geology*. 5, p273-277.

Irvine, T.N. (1980). Magmatic density currents and cumulus processes. *American Journal of Science*. 280, p1-58.

Irvine, T.N. (1980). Magmatic infiltration metasomatism, double-diffusive fractional crystallization and adcumulus growth in the Muskox intrusion and other layered intrusions. In: Hargraves, R.B. (ed.). *Physics of Magmatic Processes*. Princeton, NJ: Princeton University Press, p325-384.

Irvine, T.N., Keith, D.W. & Todd, S.C. (1983). The J-M platinum-palladium reef of the Stillwater Complex, Montana: II. Origin by double-diffusive convective magma mixing and implications for the Bushveld Complex. *Economic Geology*. 78, 1287-1334.

Irvine, T.N. (1987). Layering and related structures in the Duke Island and Skaergaard Intrusions: similarities, differences, and origins. In. Parsons, I. (ed.). *Origins of Igneous Layering*. Dordrecht: Reidel. p185-245.

Irving, A.J. (1978). A review of experimental studies of crystal/liquid trace element partitioning. *Geochimica et Cosmochimica Acta*. 42, p743-770.

Jensen, J.C., Nielsen, F.M., Duchesne, J.C., Demaiffe, D. & Wilson, J.R. (1993). Magma influx and mixing in the Bjerkreim-Sokndal layered intrusion, south Norway: evidence from the boundary between two megacyclic units at Storeknuten. *Lithos*. 29, p311-325.

Juliusz, S. (2000). Mineralogical and genetical aspects of the Smålands Taberg Fe-Ti-V ore, Protogine Zone of southern Sweden. *Geologiska Föreningens i Stockholm Förhandlingar*. 122, p351-358.

Klemm, D.D., Henchel, J. & Dehm, R. (1985). The geochemistry of titanomagnetite in magnetite layers and their host rocks of the eastern Bushveld Complex. *Economic geology*. 80, p1075-1088.

Kolker, A. (1982). Mineralogy and geochemistry of Fe-Ti oxide apatite (nelsonite) deposits and evaluation of the liquid immiscibility hypothesis. *Economic Geology*. 77, p1146-1158.

Krugar, F.J. & Smart, R. (1987). Diffusion of trace elements during bottom crystallization of double-diffusive convection systems: The magnetitite layers of the Bushveld Complex. *Journal of Volcanology and Geothermal Research*. 34, p133-142.

Lindh, A. (1973). Element distribution among silicate- and oxide minerals in a titano-magnetite ore body. *Contributions to Mineralogy and Petrology*. 39, p219-230.

Lindsley, D.H., Frost, B.R., Andersen, D.J. & Davidson, P.M. (1990). FeTi oxide-silicate equilibria: Assemblges with orthopyroxene. In: Spencer, R.J. & Chou, I.M. (eds). *Fluid mineral interactions: A tribute to H.P. Eugster, Special Publication no. 2*. The Geochemical Society, San Antonio, p103-119.

Lister, G.F. (1966). The composition and origin of selected iron-titanium deposits. *Economic Geology*. 61, p275-310.

Maaløe, S. (1978). The origin of rhythmic layering. *Mineralogical Magazine*. 42, p337-345.

Maier, W.D. & Brown, M.P. (1996). The UG2 – Merensky Reef interval of the Bushveld Complex north west of Pretoria. *Mineralium Deposita*. 31, p386-393.

Maier, W.D., Barnes, S.J., Groves, D.I. (2013). The Bushveld Complex, South Africa: formation of platinum-palladium, chrome- and vanadium-rich layers via hydrodynamic sorting of a mobilized cumulate slurry in a large, relatively slowly cooling, subsiding magma chamber. *Mineralium Deposita*. 48, p1-56.

Martin, D. (1990). Crystal settling and in-situ crystallization in aqueous and in magma chambers. *Earth and Planetary Science Letters*. 96, p336-348.

McBirney, A.R. & Noyes, R.M. (1979). Crystallization and layering of the Skaergaard intrusion. *Journal of Petrology*. 20, p487-554.

McCarthy T.S., Cawthorn, R.G., Wright, C.J. & McIver, J.R. (1985). Mineral layering in the Bushveld complex: Implications of Cr abundances in magnetite from closely spaced magnetitite and intervening silicate-rich layers. *Economic Geology*. 80, p1062-1074.

McCarthy, T.S., & Cawthorn, R.G. (1983). The geochemistry of vanadiferous magnetite in the Bushveld Complex: Implications for crystallization mechanisms in layered complexes. *Mineralium Deposita*. 18, p505-515.

Meyer, R. & De Beer, H. (1987). Structure of the Bushveld Complex from resistivity measurements. *Nature*. 325, p610-612.

Middleton, G.V. (1993). Sediment deposition from turbidity currents. *Annual Review of Earth and Planetary Sciences*. 21, p89-114.

Molyneux, T.C. (1972). X-ray data and chemical analyses of some titanomagnetite and ilmenite samples from the Bushveld Complex, South Africa. *Mineralogical Magazine*. 38, p9863-71.

Molyneux, T.G. (1974). A geological investigation of the Bushveld Complex in Sekhukuneland and part of the Steelpoort valley. *Transactions Geological Society South Africa*. 77, p329-338.

Nadoll, P., Angerer, T., Mauk, J.L., French, D. & Walshe, J. (2014). The chemistry of hydrothermal magnetite: A review. *Ore Geology Reviews*. 61, p1-32.

Naldrett, A.J. (1969). A portion of the system Fe-S-O between 900 and 1080 °C and its application to sulfide ore magmas. *Journal of Petrology*. 10, p171-201.

Naldrett, A.J., Wilson, A., Kinnaird, J., Yudovskaya, M. & Chunnett, G. (2012). The origin of chromitites and related PGE mineralization in the Bushveld Complex: new mineralogical and petrological constraints. *Mineralium Deposita*. 47, p209-232.

Namur, O., Charlier, B. & Holness, M.B. (2012). Dual origin of Fe-Ti-P gabbros by immiscibility and fractional crystallization of evolved tholeiitic basalts in the Sept Iles layered intrusion. *Lithos*. 154, p100-114.

Namur, O., Charlier, B., Toplis, M.J., Higgins. M.D., Liegeois, J. & van der Auwera, J. (2010). Crystallization sequence and magma chamber processes in the ferrobasaltic Sept Iles layered intrusion, Canada. *Journal of Petrology*. 51, p1203-1236.

Naslund, H.R. & McBirney, A.R. (1996). Mechanisms of formation of igneous layering. In: Cawthorn, R.G. (ed). *Layered Intrusions*. Amsterdam: Elsevier, p1-44.

Nex, P.A.M. (2004). Formation of bifurcating chromitite layers of the UG1 in the Bushveld Igneous Complex, an analogy with sand volcanoes. *Journal of the Geological Society*. 161, p903-909.

Osborn, E.F. (1978). Changes in phase relations in response to change in pressure from 1 atm to 10 kbar for the system Mg_2SiO_4-iorn oxide-$CaAl_2Si_2O_8$-SiO_2. *Carnegie Institution of Washington Yearbook*. 77, p784-90.

Pang, K., Zhou, M., Lindsley, D., Zhao, D. & Malpas, J. (2008). Origin of Fe-Ti oxide ores in mafic intrusions: Evidence from the Panzhihua Intrusion, SW China. *Journal of Petrology*. 49, p295-313.

Pearce, C.I., Michael, C., Henderson, B., Telling, N.D., Patric, R.A.D., Charnock, J.M., Coker,V.S., Arenholz, E., Tuna, F. & van der Laan, G. (2010). Fe site occupancy in magnetite-ulvospinel solid solutions: A new Approach using X-ray magnetic circular dichroism. *American Mineralogist*. 95, p425-439.

Philpotts, A.R. (1979). Silicate liquid immiscibility in tholeitic basalts. *Journal of Petrology*. 20, p99-118.

Philpotts, A.R. & Doyle, C.D. (1983). Effect of magma oxidation state on the extent of silicate liquid immiscibility in a tholeitic basalt. *American Journal of Science*. 283, p967-986.

Philpotts, A.R. (1967). Origin of certain iron-titanium oxide and apatite rocks. *Economic Geology*. 62, p303-315.

Radko, T. & Smith, D.P. (2012). Equilibrium transport in double-diffusive convection. *Journal of Fluid Mechanics*. 692, p5-27.

Reynolds, I.M. (1985a). The nature and origin of titaniferous magnetite-rich layers in the Upper zone of the Bushveld Complex: A review and synthesis. *Economic Geology*. 80, p1089-1108.

Reynolds, I.M. (1985b). Contrasted mineralogy and textural relationships in the uppermost titaniferous magnetite layers of the Bushveld Complex in the Bierkraal area north of Rustenburg. *Economic Geology*. 80, p1027-1048.

Roeder, P.L. & Osborn, E.F. (1966). Experimental data for the system MgO-FeO-Fe_2O_3-$CaAl_2SiO_2O_8$-SiO_2 and their petrologic implications. *American Journal of Science*. 264, p428-480.

Roy, S. (1956). Origin of the vanadium-bearing titaniferous magnetite ores of Mayurbhanj, India. *The Proceedings of the National Institute of Sciences India*. 22, p285-292.

Saha, A., Ganguly, S., Jyotisankar, R. & Dhang, A. (2010). Vanadium bearing titaniferous magnetite ore bodies of Ganjan, Karbi-Anglong District, north eastern India. *Journal Geological Society of India*. 76, p26-32.

Schuiling, R.D. & Feenstra, A. (1980). Geochemical behavior of vanadium in iron-titanium ores. *Chemical Geology*. 30, p143-150.

Scoon, R.N. & Mitchell, A.A. (1994). Discordant iron-rich ultramafic pegmatites in the Bushveld Complex and their relationship to iron-rich intercumulus and residual liquids. *Journal of Petrology*. 35, p881-917.

Scoon, R.N. & Mitchell, A.A. (2012). The Upper Zone of the Bushveld Complex at Rossenekal, South Africa: Geochemical stratigraphy and evidence of multiple episodes of replenishment. *South African Journal of Geology*. 115, p515-534.

Tegner, C., Cawthorn, R.G. & Kruger, F.J. (2006). Cyclicity in the Main and Upper Zones of the Bushveld Complex, South Africa: Crystallization from a zoned magma sheet. *Journal of Petrology*. 47, p2257-2279.

Toplis, M.J. & Carroll, M.R. (1995). An experimental study of the influence of oxygen fugacity on Fe-Ti oxide stability, phase relations, and mineral-melt equilibria in ferro-basaltic systems. *Journal of Petrology*. 36, p1137-1170.

Toplis, M.J. & Corgne, A. (2002). An experimental study of element partitioning between magnetite, clinopyroxene and iron-bearing silicate liquids with particular emphasis on vanadium. *Contributions to Mineralogy and Petrology*. 144, p22-37.

van der Merwe, M.J. (1976). The layered sequence of the Potgietersrus limb of the Bushveld complex. *Economic Geology*. 71, p1337-1351.

Veksler, I.V., Dorfman, A.M., Danyushevsky, L.V., Jakobsen, J.K. & Dingwel, D.B. (2006). Immiscible silicate liquid partition coefficient implications for crystal-melt element partitioning and basalt petrogenesis. *Contributions to Mineralogy and Petrology*. 152, p785-702.

Veksler, I.V., Dorfman, A.M. Borisov, A.A., Wirth, R. & Dingwell, D.B. (2007). Liquid immiscibility and the evolution of basaltic magma. *Journal of Petrology*. 48, p2187-2210

Vidyashankar, H.V. & Govidaiah, S. (2009). Ore petrology of the V-Ti magnetite (Lodestone) layers of the Kurihundi area of Sargur Schist Belt, Dharwar Craton. *Journal Geological Society of India*. 74, p8-68.

Von Gruenewaldt, G. (1973). The Main and Upper zones of the Bushveld Complex in the Roossenekal area, eastern Transvaal. *Transactions Geological Society of South Africa*. 76, p207-227.

Von Gruenewaldt, G. (1976). Sulfides in the Upper Zone of the Eastern Bushveld Complex. *Economic Geology*. 71, p1324-1336.

Von Gruenewaldt, G., Klemm, D.D., Henckel, J. & Dehm, R.M. (1985). Exsolution features in titanomagnetites from massive magnetite layers and their host rocks of the Upper Zone, Eastern Bushveld Complex. *Economic Geology*. 80, p1049-1061.

Willemse, J. (1969). The geology of the Bushveld Igneous Complex, the largest repository of magmatic ore deposits in the world. *Economic Geology Monograph*, 4, p1-22.

Zhou, M., Robinson, P.T., Lesher, C.M., Keays, R.R., Zhang, C. & Malpas, J. (2005). Geochemistry, petrogenesis and metallogenesis of the Panzhihua Gabbroic Layered Intrusion and associated Fe-Ti-V oxide Deposits, Sichuan Province, SW China. *Journal of Petrology*. 46, p2253-2280.

Appendix A – Analytical Techniques

Pressed pellets of pure finely pulverised magnetite were analysed by XRF by David Long at Sci-Ba Laboratories and Scientific Consultants. Detection limits for major and minor elements in magnetite are given in Table A1. The measurements were run in triplicate and the certified composition of the standards used for calibration and averages of their measured compositions are given in Table A2. The highest Cr content for a standard is 1416 ppm (AMIS0368). Many samples analyzed here contain up to 14 000 ppm, and hence the calibration equation was greatly extrapolated. Thus the accuracy for these high concentrations is not high. However, in view of the extreme changes recognised repeatedly in multiple profiles through the base of the MML, the trends can be confidently considered reliable. The high Cr content reported here for samples along the base of the MML are closely similar to those reported by Cawthorn and McCarthy (1980, 1981) and Cawthorn (1994). Thus the new and old data are internally consistent.

Table A1. Detection Limits for Major and Minor Elements on Pressed Pellets

V (ppm)	TiO_2 (wt%)	Cr (ppm)	Cu (ppm)	Ni (ppm)	Al_2O_3 (wt%)	MgO (wt%)
48	0.04	13	12	7	0.77	0.06

Table A2. Standards used for XRF Calibration

	AMIS0346				AMIS0347				AMIS0368			
	Certified	**Average**	**Stdev**	**%Diff**	**Certified**	**Average**	**Stdev**	**%Diff**	**Certified**	**Average**	**Stdev**	**%Diff**
V_2O_5 (ppm)	4820	4834	590	**-0.29**	12300	12421	169.8	**-0.98**	14996	14514	351.8	**3.21**
TiO_2 (wt%)	25.26	25.20	0.162	**0.24**	15.88	17.59	0.142	**-10.77**	13.91	13.56	0.245	**2.52**
Cr (ppm)	185	205	9.95	**-10.81**	349	339	6.28	**2.87**	1416	1613.2	42.49	**-13.93**
Cu (ppm)	137.9	127	5.68	**7.90**	111	108	3.96	**2.70**	220	225	9.33	**-2.27**
Ni (ppm)	30.6	53	8.02	**-73.20**	128	148	9.50	**-15.63**	392	309	10.27	**21.17**
Al_2O_3 (ppm)	2.86	2.86	0.073	**0.00**	3.86	4.49	0.139	**-16.32**	3.64	4.37	0.054	**-20.05**
MgO (ppm)	2.08	3.01	0.056	**-44.71**	0.96	1.01	0.026	**-5.21**	0.68	0.45	0.026	**33.82**

	AMIS0372				SARM-12			
	Certified	**Average**	**Stdev**	**%Diff**	**Certified**	**Average**	**Stdev**	**%Diff**
V_2O_5 (ppm)	86	71.6	17.6	**16.74**	928	1027	31.9	**-10.67**
TiO_2 (wt%)	0.18	0.19	0.004	**-5.56**	0.72	0.8	0.008	**-11.11**
Cr (ppm)	93.1	95.6	8.85	**-2.69**	21	37.8	7.95	**-80.00**
Cu (ppm)	20.7	16	2.65	**22.71**	502	483	19.3	**3.78**
Ni (ppm)	17	25	16.87	**-47.06**	281	287	21.4	**-2.14**
Al_2O_3 (wt%)	2.8	2.7	0.085	**3.57**	0.77	0.68	0.034	**11.69**
MgO (wt%)	0.07	0.1	0.011	**-42.86**	2.8	2.8	0.017	**0.00**

Average = Average for multiple analyses of reference samples run as unknown samples.
Stdev = Standard deviation between multiple measured analyses.
%Diff. = Percentage difference between certified composition of standards and average measured composition.

Appendix B – Re-Analyzed Samples

Samples from profile G from a previous incomplete project on the magnetitite layers of the Bushveld Complex were re-analyzed at Sci-Ba Laboratories and Scientific Consultants, in order to ensure a consistent data set to be used in the current study. They had previously been analyzed, but results not published, by XRF at the University of the Witwatersrand by the procedure described by Cawthorn and McCarthy (1980). Figure 1 is a plot of the composition of the re-analyses against the original compositions. It is important to note that samples with up to 12 000 ppm (for which standards were not available for this project) yield similar values.

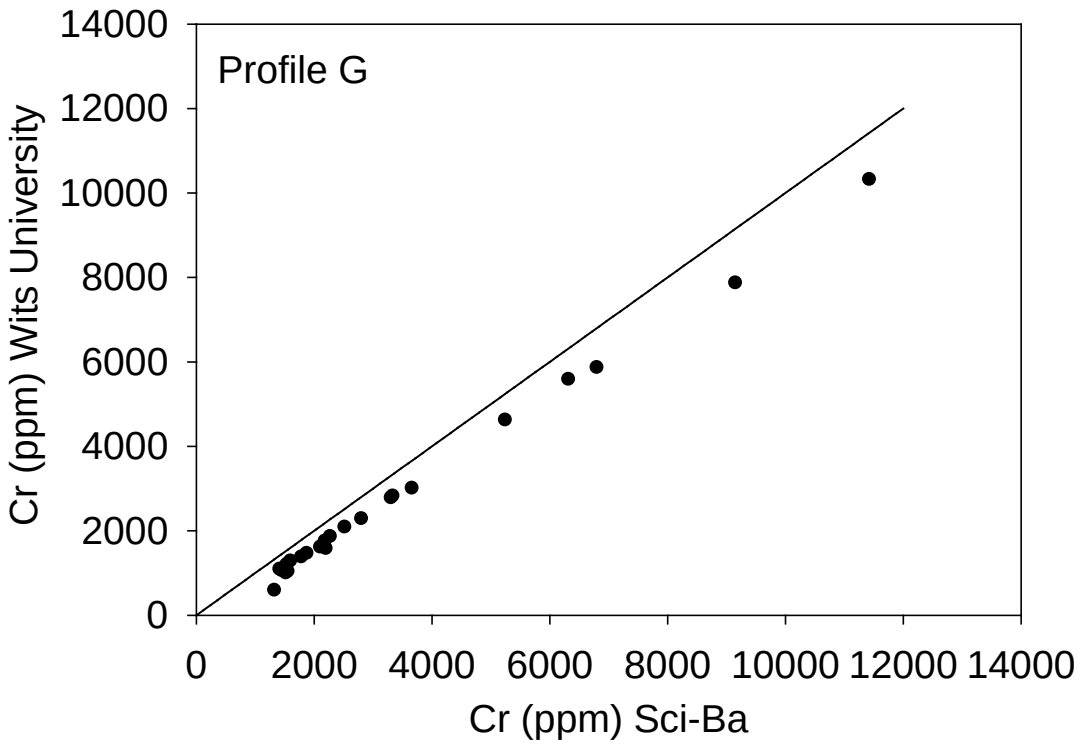

Fig. 1. Cr and V contents of magnetite of samples analyzed at Wits University and Sci-Ba (this project).

Appendix C – Major and Minor Elements in Magnetite.

C1. Vertical Profiles (1-4) through the Main Magnetitite Layer.

Sample	Height (cm)	V (wt%)	TiO_2 (wt%)	Cr (ppm)	Cu (ppm)	Ni (ppm)	$Al2O_3$ (wt%)	MgO (wt%)	SiO_2 (wt%)
1A	0	1.15	11.51	7716	BD	567	3.38	1.43	0.41
1B	10	1.18	12.06	8110	BD	436	3.41	1.44	0.30
1C	20	1.23	12.32	5447	47	584	3.92	0.92	0.20
1D	30	1.16	11.97	3398	339	289	3.17	0.70	0.95
1E	40	1.13	11.57	2925	229	366	4.91	3.14	3.69
1F	50	1.23	12.59	2517	77	294	3.72	1.15	0.96
1G	60	1.16	11.71	1968	116	409	3.52	1.18	0.43
1H	70	1.22	12.58	2593	149	296	3.90	1.36	0.71
1I	92	1.20	12.17	1591	579	350	4.71	2.41	3.77
1J	110	1.23	12.93	1482	140	592	3.91	1.00	0.27
2A	0	1.15	11.56	12122	285	660	3.57	2.43	0.79
2B	7	1.18	11.72	7473	BD	554	3.48	1.68	0.37
2C	14	1.15	11.91	6747	51	471	3.46	1.07	0.26
2D	21	1.15	11.02	6668	453	536	4.62	2.50	3.20
2E	28	1.15	12.15	4920	112	675	3.86	2.31	1.03
2F	35	1.18	12.11	3881	176	735	3.31	1.49	0.36
2G	42	1.19	11.95	3872	50	801	3.11	1.29	0.21
2H	49	1.11	11.53	2543	90	521	3.97	2.62	1.75
2I	56	1.15	11.95	1829	105	491	3.81	2.05	1.36
2J	63	1.21	12.36	1781	173	407	3.51	1.44	0.85
2K	70	1.23	12.19	1374	153	286	3.20	0.89	0.47
2L	77	1.19	12.31	2422	143	414	4.16	1.46	1.10
2M	84	1.18	12.25	1611	53	467	3.71	0.82	0.13
2N	91	1.08	10.69	708	149	679	5.95	1.02	0.31
2O	98	1.19	11.95	733	255	536	3.30	1.08	0.31
2P	110	1.15	11.95	699	350	652	3.05	1.36	0.90
3A	0	1.12	11.76	12106	BD	740	3.34	1.75	0.26
3B	7	1.19	12.52	8175	BD	696	3.72	1.56	0.33
3C	14	1.16	12.04	6287	BD	513	3.55	1.64	0.48
3D	21	1.15	11.96	5776	BD	665	3.31	1.90	0.18
3E	28	1.13	11.77	4541	BD	545	4.27	1.22	0.34
3F	35	1.17	12.24	4683	BD	517	3.55	1.40	0.49
3G	42	1.21	12.56	3952	BD	455	3.49	1.11	0.30
3H	49	1.20	12.34	3711	BD	322	3.31	1.05	0.46
3I	56	1.17	12.03	2777	88	482	3.50	1.32	0.35
3J	63	1.14	11.69	2569	111	429	3.36	1.15	0.09
3K	70	1.20	12.44	2254	149	522	3.43	1.21	0.09
3L	77	1.19	12.33	2099	228	586	3.40	1.50	0.09
3M	84	1.18	12.36	1751	590	588	3.62	2.22	1.36
3N	91	1.16	12.07	1560	587	426	3.94	2.30	2.45

3O	98	1.13	11.82	1420	576	464	4.56	2.32	3.55
3P	110	1.16	12.69	1439	337	514	3.29	1.31	0.45
4A	0	1.18	12.36	12582	BD	671	3.64	1.65	0.66
4B	7	1.16	12.26	8092	BD	508	3.47	1.00	0.23
4C	14	1.21	12.29	6176	BD	553	3.39	0.95	BD
4D	21	1.20	12.23	5265	BD	568	3.64	0.94	0.10
4E	28	1.21	12.33	4685	BD	544	3.65	1.03	0.18
4F	35	1.18	11.94	3797	BD	648	3.28	1.17	BD
4G	42	1.21	12.52	3410	93	568	3.46	1.50	0.36
4H	49	1.17	11.78	2685	99	480	2.66	0.97	BD
4I	56	1.16	11.73	2777	144	513	3.07	1.44	0.78
4J	63	1.21	12.44	2476	105	642	3.47	1.46	0.44
4K	70	1.18	12.22	2139	251	728	3.07	1.57	0.74
4L	77	1.16	12.1	1700	312	391	3.90	2.07	1.45
4M	84	1.16	11.95	1477	275	431	3.90	2.24	1.94
4N	91	1.19	12.48	1576	259	454	4.55	2.69	3.87
4O	95	1.16	11.86	1599	509	256	4.59	2.00	3.27
4P	98	1.23	12.31	1428	357	441	3.60	1.55	1.79
4Q	115	1.16	12.17	1341	63	409	2.94	1.14	0.46

BD = Below Detection Limit

Table C2. Cr in Magnetite Profiles D1-D6 through Feldspar Parting

Sample	Height (cm)	D1	D2	D3	D4	D5	D6
A	90	1486	1580	1676	1491	1642	1729
B	95	1440	1436	1470	1488	1218	1549
C	100	1512	1463	1445	1434	1469	1326
D	105	1301	1312	1213	1356	1426	1512
E	110	1322	1335	1331	1242	1427	1295
F	115	1274	1300	1284	1316	1353	1271
G	120	1393	1342	1199	1401	1242	1338

All data given in ppm

Highlighted cells = Feldspar parting

Table C3. Profile P through Feldspar Parting

Sample	Height (cm)	V (wt%)	TiO_2 (wt%)	Cr (ppm)	Cu (ppm)	Ni (ppm)	Al_2O_3 (wt%)	MgO (wt%)	SiO_2 (wt%)
P1	22	1.06	12.44	2604	180	466	3.65	2.31	0.88
P2	50	1.07	12.36	1763	386	521	3.45	1.22	0.66
P3	70	1.11	12.88	1749	237	472	2.77	1.04	0.76
P4	95	1.05	11.97	1310	564	515	2.66	1.48	2.03
P5	110	1.15	13.59	1457	164	391	2.98	0.39	0.55
P6	130	1.00	12.1	1152	260	503	0.94	0.77	1.19
P7	150	1.24	12.67	567	273	503	3.01	0.71	0.27

Highlighted cells = Feldspar parting

Table C4. Profiles (G-H) at Dome Structure

G			H			I			J		
Sample	**Height (cm)**	**Cr (ppm)**	**Sample**	**Height (cm)**	**Cr (ppm)**	**Sample**	**Height (cm)**	**Cr (ppm)**	**Sample**	**Height (cm)**	**Cr (ppm)**
G130	125	1336	H130	125	1429	I95	90	1383	J70	65	1401
G125	120	1462	H125	120	1497	I90	85	1416	J65	60	1449
G120	115	1517	H120	115	1475	I85	80	1482	J60	55	1604
G115	110	1885	H115	110	1473	I80	75	1844	J55	50	1790
G110	105	1475	H110	105	1442	I75	70	1953	J50	45	1666
G105	100	1564	H105	100	1478	I70	65	1524	J45	40	1833
G100	95	1536	H100	95	1700	I65	60	1879	J40	35	2035
G95	90	1424	H95	90	1776	I60	55	1975	J35	30	2454
G90	85	1530	H90	85	1847	I55	50	2275	J30	25	3024
G85	80	1553	H85	80	1907	I50	45	2361	J25	20	3832
G80	75	1607	H80	75	2195	I45	40	2912	J20	15	4645
G75	70	1794	H75	70	2338	I40	35	2828	J15	10	7828
G70	65	2115	H70	65	2815	I35	30	3941	J10	5	8207
G65	60	2210	H65	60	3010	I30	25	7369	J5	0	12468
G60	55	2194	H60	55	3440	I25	20	5469			
G55	50	2282	H55	50	3837	I20	15	5725			
G50	45	2527	H50	45	4204	I15	10	6040			
G45	40	2813	H45	40	4499	I10	5	7419			
G40	35	3344	H40	35	5093	I5	0	11648			
G35	30	3670	H35	30	4372						
G30	25	3314	H30	25	5733						
G25	20	5254	H25	20	5845						
G20	15	6810	H20	15	6397						
G15	10	6325	H15	10	6692						
G10	5	9162	H10	5	6994						
G5	0	11435	H5	0	10120						

Highlighted cells = Feldspar parting

Table C5. Re-Analyzed Profile G

Sample	Height (cm)	V (wt%)	TiO_2 (wt%)	Cr (ppm)	*Cr (Wits) (ppm)*	Cu (ppm)	Ni (ppm)	Al_2O_3 (wt%)	MgO (wt%)	SiO_2 (wt%)
G5	0	0.90	10.59	10311	*11435*	23	422	2.84	1.56	1.02
G10	5	0.92	10.72	7860	*9162*	35	476	3.14	1.27	1.08
G15	10	0.94	10.91	5578	*6325*	14	994	2.99	1.35	0.89
G20	15	0.92	10.55	5854	*6810*	28	466	2.66	1.12	0.57
G25	20	0.95	10.9	4614	*5254*	31	595	2.82	1.81	0.36
G30	25	0.93	10.7	2769	*3314*	345	535	3.08	2.02	1.71
G35	30	0.92	10.86	2999	*3670*	110	823	1.45	0.94	0.38
G40	35	0.95	11.13	2814	*3344*	125	419	1.09	0.59	0.26
G45	40	0.91	10.62	2275	*2813*	320	2264	1.75	0.81	1.16
G50	45	0.96	11.15	2078	*2527*	157	488	2.93	1.47	0.76
G55	50	0.92	10.55	1854	*2282*	245	499	2.36	2.63	2.24
G60	55	0.94	10.8	1744	*2194*	306	589	2.73	2.37	1.62
G65	60	0.91	10.42	1571	*2210*	264	822	1.04	0.92	0.29
G70	65	0.90	10.5	1602	*2115*	239	572	2.25	2.32	2.64
G75	70	0.96	11.04	1371	*1794*	497	573	2.07	1.43	1.03
G80	75	0.92	10.65	1274	*1607*	454	408	3.03	2.61	3.03
G85	80	0.93	10.53	1198	*1553*	1154	790	2.80	2.02	2.15
G90	85	0.88	9.95	988	*1530*	982	560	2.48	1.62	2.59
G95	90	0.93	10.97	1079	*1424*	601	493	2.83	1.83	1.29
G100	95	0.97	11.26	1170	*1536*	455	606	2.44	1.62	0.54
G105	100	0.93	10.75	1027	*1564*	280	462	2.97	0.81	0.69
G110	105	0.92	10.82	1090	*1475*	200	456	3.12	0.71	1.15
G115	110	1.00	11.04	1457	*1885*	226	777	2.55	0.87	1.77
G120	115	0.92	10.57	1050	*1517*	266	481	2.82	0.84	1.18
G125	120	0.93	10.6	1048	*1462*	382	515	2.44	0.63	1.73
G130	125	1.14	11.39	582	*1336*	291	699	3.29	0.86	1.15

Highlighted cells = Feldspar parting

Values in italics = Wits University original analyses

Table C6. Profile CM along Base of the Main Magnetitite Layer from Cawthorn (1994)

West bank				East bank			
sample	Distance (m)	V (wt%)	Cr (ppm)	sample	Distance (m)	V (wt%)	Cr (ppm)
CM1	**0**	1.02	11461		**0**		
CM2	**10**	1.03	10931	**CM13**	**10**	0.90	13047
CM3	**20**	0.89	12680	**CM14**	**20**	0.72	10530
CM4	**30**	1.00	14311	**CM15**	**30**	0.97	10117
CM5	**40**	1.00	12915	**CM16**	**40**	0.99	13459
CM6	**50**	0.87	13779	**CM17**	**50**	0.88	10742
CM7	**60**	1.03	14557	**CM18**	**60**	1.01	15899
CM8	**70**	0.99	15437	**CM19**	**110**	1.02	16206
CM9	**80**	0.98	12713				
CM10	**90**	1.09	17058				
CM11	**100**	0.99	12226				
CM12	**110**	0.86	28755				

Table C7. Profile B along Base of the Main Magnetitite Layer (east bank)

Sample	Distance (m)	V (wt%)	TiO_2 (wt%)	Cr (ppm)	Cu (ppm)	Ni (ppm)	Al_2O_3 (wt%)	MgO (wt%)	SiO_2 (wt%)
B1	**0**	1.02	11.75	17085	180	491	3.04	1.85	1.77
B2a	**1.4**	1.06	12.48	10416	96	548	3.56	1.58	0.69
B2b	**1.4**	1.03	12.27	13223	208	524	3.78	2.21	1.01
B3	**3.7**	1.05	12.5	12347	74	534	3.26	1.93	0.67
B4	**5.2**	1.06	12.58	9241	42	427	2.81	1.09	0.48
B5	**7.1**	1.01	11.64	12373	43	534	2.99	1.53	0.90
B6	**9.1**	1.03	12.23	12063	66	528	3.16	1.92	0.75
B7a	**11.1**	1.07	12.56	11222	7	447	2.29	0.74	BD
B7b	**11.1**	1.09	12.83	11361	52	497	2.36	0.71	BD
B8	**13**	1.02	12.29	12055	50	540	3.27	1.59	0.60
B9a	**15**	1.08	12.7	12684	71	441	3.68	1.33	1.08
B9b	**15**	0.99	11.81	12694	89	480	4.06	1.73	0.44
B10	**16.3**	1.01	12.17	12501	66	506	3.66	2.43	BD
B2 diff.		-0.03	-0.21	2807	112	-24	0.22	0.63	0.3276
B7 diff.		0.02	0.27	139	45	50	0.06	-0.03	BD
B9 diff.		-0.08	-0.89	10	18	39	0.38	0.40	-0.6396

diff. = difference between top and bottom of pieces typically less than 3 cm thick

Table C8.Vertical Profiles SL1-SL10 through the Main Magnetitite Layer, Sub-Layers and Disseminated Magnetite at Swartkop

Sample	Height (cm)	Cr (ppm)	Sample	Height (cm)	Cr (ppm)
SL1/A	0	6492	**SL6/A**	1	2974
SL1/B	3	5217	**SL6/B**	6	1374
SL1/C	6	3960	**SL6/C**	11	1240
SL1/D	9	3670	**SL6/D**	18	1073
SL1/E	12	3594	**M21**	22	876
SL1/F	15	2746	**M22**	25	817
SL1/G	18	2456	**M23**	28	902
SL1/H	21	1993	**SL7/A**	1	2477
SL1/I	24	1743	**SL7/B**	3	1865
SL1/J	27	1190	**SL7/C**	6	1426
SL1/K	30	1082	**SL7/D**	8	1092
SL1/L	33	929	**M17**	9	995
SL1/M	36	916	**M18**	12	817
SL1/N	39	740	**M19**	15	797
SL1/O	42	737	**M20**	20	828
SL1/P	45	473			
SL1/Q	48	444			
SL1/R	51	390			
SL1/S	54	342			
SL1/T	57	273			
SL2/A	2	7482	**SL8/A**	1	1325
SL2/B	13	7299	**SL8/B**	6	1124
SL2/C	20	5121	**SL8/C**	13	821
SL2/D	26	3170	**M26**	17	992
SL2/E	30	3654	**M27**	20	888
SL2/F	37	2143	**M28**	25	592
SL2/G	45	1050			
SL2/H	51	676			
SL3/A	1	6346	**SL9/A**	2	1449
SL3/B	6	4491	**SL9/B**	8	892
SL3/C	12	1672	**SL9/C**	12	1065
SL3/D	17	1151	**SL9/D**	20	1017
SL3/E	22	1522			
SL4/A	2	1529	**SL10/A**	1	932
SL4/B	9	1226	**SL10/B**	8	1272
SL4/C	17	1099	**SL10/C**	14	1159
SL4/D	28	974	**SL10/D**	19	1058
SL4/E	35	1349	**SL10/E**	24	946
SL5/A	2	2797			
SL5/B	11	1199			
SL5/C	16	1066			
SL5/D	21	1020			
SL5/E	28	893			
SL5/F	34	1018			

Table C9. Samples M1-M14 along Base of Main Magnetitite Layer adjacent to Bifurcations at Swartkop

Sample	Distance (m)	Cr (ppm)
M1	0.0	7846
M2	0.9	6765
M3	1.7	7541
M4	4.0	7331
M5	5.2	5929
M6	6.2	5687
M7	7.2	5443
M8	8.2	5997
M9	9.7	6220
M10	10.7	5336
M11	12.2	5831
M12	13.2	6193
M13	14.3	6254
M14	15.0	5726

Table C10. Vertical Profiles L/1-L/9 through Layer 1 at Magnet Heights

Sample	Height (cm)	Cr (ppm)	V (wt%)	Sample	Height (cm)	Cr (ppm)	V (wt%)
L1/1A	0	2375	0.10	**L1/5A**	0	2140	1.02
L1/1B	1	2348	0.11	**L1/5B**	1	2281	0.99
L1/1C	2	2302	0.10	**L1/5C**	2	2097	0.95
L1/1D	3	2319	0.10	**L1/5D**	3	2077	0.98
L1/1E	4	2366	0.11	**L1/5E**	4	2121	0.90
L1/1F	5	2310	0.10	**L1/5F**	5	2027	1.02
L1/1G	6	2221	0.10	**L1/5G**	6	2018	0.96
L1/1H	7	2276	0.11	**L1/5H**	7	1934	0.90
L1/1I	8	2181	0.11	**L1/5I**	8	1935	1.01
L1/1J	9	2233	0.11	**L1/5J**	9	1866	1.00
				L1/5K	10	1675	0.98
L1/2A	0	2470	1.06	**L1/6A**	4	2322	1.00
L1/2B	1	2510	1.08	**L1/6B**	5	2352	1.00
L1/2C	2	2473	1.08	**L1/6C**	6	2140	0.96
L1/2D	3	2419	1.09	**L1/6D**	7	2378	0.99
L1/2E	4	2360	1.06	**L1/6E**	8	2159	0.97
L1/2F	5	2350	1.05	**L1/6F**	9	1835	0.98
L1/2G	6	2314	1.03	**L1/7A**	0	2679	0.94
L1/2H	7	2166	1.05	**L1/7B**	1	2417	0.98
L1/2I	8	2286	1.06	**L1/7C**	2	2278	0.97
L1/2J	9	2302	1.05	**L1/7D**	3	2128	0.99
L1/3A	0	2321	1.01	**L1/7E**	4	2161	0.98
L1/3B	1	2337	1.07	**L1/7F**	5	2184	0.97
L1/3C	2	2325	1.07	**L1/7G**	6	2148	0.98
L1/3D	3	2374	1.04	**L1/7H**	7	2072	0.98
L1/3E	4	2326	1.02	**L1/7I**	8	2043	0.93
L1/3F	5	2276	1.03	**L1/7J**	9	1998	0.96
L1/3G	6	2192	1.03	**L1/8A**	0	3799	0.98
L1/3H	7	2294	1.05	**L1/8B**	1	3508	0.96
L1/3I	8	2157	1.04	**L1/8C**	2	3216	1.00
L1/3J	9	2261	1.03	**L1/8D**	3	2919	1.01
L1/4A	0	3201	0.99	**L1/8E**	4	2522	1.01
L1/4B	1	2950	1.03	**L1/8F**	5	2405	0.99
L1/4C	2	2706	0.98	**L1/8G**	6	2273	0.99
L1/4D	3	2444	0.99	**L1/8H**	7	2199	1.01
L1/4E	4	2305	1.01	**L1/8I**	8	2219	0.97
L1/4F	5	2259	0.98	**L1/9A**	0	2419	0.94
L1/4G	6	2153	0.93	**L1/9B**	1	2486	0.99
L1/4H	7	2052	0.95	**L1/9C**	2	2507	1.01
L1/4I	8	2002	0.95	**L1/9D**	3	2318	0.97
L1/4J	9	2104	0.97	**L1/9E**	4	2265	0.98
				L1/9F	5	2297	0.99
				L1/9G	6	2175	0.97
				L1/9H	7	2141	0.97
				L1/9I	8	2078	0.97
				L1/9J	9	2096	0.95

Table C11. UCAR Mine Drill Core

Sample	Height (cm)	Cr (ppm)	V (wt%)
1	4	664	
2	44	522	
3	79	492	0.69
4	108	625	0.78
5	139	599	0.74
6	176	672	0.72
7	189	793	0.83
8	198	788	0.84
9	210	972	0.87
10	221	1252	0.91
11	226	1504	0.95
12	253	119	0.86
13	293	582	0.77
14	332	643	0.74
15	365	639	0.75
16	402	804	0.78
17	454	1059	0.85
18	470	1295	0.94
19	482	1407	0.85
20	494	1445	0.93
21	501	1784	0.88
22	505	1955	0.94
23	507	1982	0.92
24	511	478	0.92
25	517	139	0.96
26	523	171	0.93
27	530	216	0.94
28	541	241	1.01
29	550	439	0.94
30	560	476	1.01
31	570	491	0.97
32	580	673	0.98
33	588	909	0.88
34	594	728	0.93
35	601	716	0.89
36	610	976	0.87
37	615	1063	0.97
38	624	1402	1.02
39	630	2173	0.98
40	638	2716	1.02
41	651	2046	0.97
42	660	5950	1.09
43	663	6778	1.06
44	667	12895	1.19

Table C12. Bierkraal Drill Cores (BK1 and BK3)

Sample	Composite drill core Depth (m)	Cr (ppm)	V (wt%)	TiO_2 (wt%)	Lithology
BK1/579	579	516	0.03	8.02	D
BK1/582,4	582.4	615	0.03	7.18	D
BK1/586,8	586.8	567	0.03	8.00	D
BK1/591,5	591.5	664	0.07	6.43	D
BK1/598	598	704	0.01	9.47	D
BK1/604	604	683	0.07	9.38	D
BK1/611	611	604	0.10	6.53	D
BK1/631,2	631.2	870	0.11	10.72	D
BK1/631,66	631.66	1007	0.10	11.20	D
BK1/632,18	632.18	1371	0.09	12.81	D
BK1/623,43	623.43			9.41	D
BK1/633,7	633.7	709	0.05	12.04	D
BK1/637,85	637.85			12.13	D
BK1/638,05	638.05	604	0.10	13.43	D
BK1/638,2	638.2	647	0.10		D
BK1/647,3	647.3			11.58	D
BK1/651	651		0.03		D
BK1/654,7	654.7			9.08	D
BK1/663,3	663.3	620	0.10		D
BK1/691,1	691.1			6.94	D
BK1/704,4	704.4	594	0.01	8.51	D
BK1/709	709	635	0.01	8.17	D
BK1/718	718	603	0.01	8.76	D
BK1/722	722	529	0.02	8.91	D
BK1/727,5	727.5	558	0.03	8.49	D
BK1/732	732	666	0.02	10.21	D
BK1/736,5	736.5		0.03	11.21	D
BK1/744,8	744.8	595	0.03	9.88	D
BK1/751,1	751.1	572	0.05	10.27	D
BK1/759,8	759.8	566	0.05	11.74	D
BK1/763,7	763.7	893	0.06	12.95	D
BK1/773,8	773.8	830	0.12	11.08	D
BK1/804,4	804.4	592	0.07	10.33	D
BK1/808,6	808.6	545	0.09	9.75	D
BK1/820	820	1220	0.10	10.15	LD
BK1/824	824	1497	0.10	12.43	LD
BK1/862	862	611	0.05	9.46	D
BK1/872	872	509	0.11	11.24	D
BK1/876,3	876.3	688	0.14	9.91	D
BK1/880,5	880.5	2585	0.12	14.04	A
BK1/888,5	888.5	530	0.03	9.33	D
BK1/892,5	892.5	544	0.02	9.52	D
BK1/908,6	908.6	905	0.05	10.04	A
BK1/914	914	587		0.48	D
BK1/944	944	521	0.03	9.42	LD

A = ANORTHOSITE
D = DIORITE
LD = LUCODIORITE
M = MAGNETITITE LAYER
G = GABBRO
T = TROCTOLITE
LG = LUCOGABBRO

BK1/954	954	510	0.01	8.97	D
BK1/963,2	963.2	521	0.01	9.82	LD
BK1/971,6	971.6	708			LD
BK1/983,7	983.7	510	0.01	9.09	D
BK1/995,4	995.4	530	0.01	9.66	D
BK1/1004	1004	529		11.46	D
BK1/1010,2	1010.2	532	0.03	10.17	D
BK1/1019,2	1019.2	525	0.01	9.15	D
BK1/1028,9	1028.9	546		7.89	D
BK1/1040	1040	666		8.91	D
BK1/1050,5	1050.5	588		10.20	D
BK1/1060,5	1060.5	502	0.01	10.80	D
BK1/1069	1069	578	0.01	11.63	D
BK1/1076,4	1076.4	568	0.01	14.21	D
BK1/1076,7	1076.7	536	0.02	15.66	D
BK1/1076,8	1076.8	548	0.01	13.33	D
BK1/1080,3	1080.3	522	0.01	12.21	D
BK1/1083,3	1083.3	733	0.02	11.77	D
BK1/1086,15	1086.15	569		15.73	D
BK1/1090,2	1090.2	536	0.02	18.52	D
BK1/1095,2	1095.2	523	0.02	18.68	D
BK1/1098,2	1098.2	572	0.02	17.16	D
BK1/1098,9	1098.9	597	0.05	17.35	D
BK1/1099	1099	715	0.03	15.69	LD
BK1/1105,7	1105.7		0.02	5.16	M
BK1/1111,2	1111.2	588	0.05	17.78	LD
BK1/1111,5	1111.5	648	0.06	17.30	M
BK1/1112	1112	559	0.06	16.61	M
BK1/1113	1113	574	0.07	19.32	M
BK1/1115,5	1115.5	1700	0.12	10.13	D
BK1/1116,9	1116.9	2932	0.13	11.07	D
BK1/1117,1	1117.1	2577	0.10	13.56	M
BK1/1118,2	1118.2	817	0.10	10.95	D
BK1/1123,7	1123.7	576	0.05	9.15	D
BK1/1128,2	1128.2	971	0.04	9.40	D
BK1/1132,7	1132.7	937	0.05	9.65	D
BK1/1138,2	1138.2	900	0.03	8.05	D
BK1/1144,7	1144.7	1347	0.05	10.33	D
BK1/1150,5	1150.5	916	0.09	8.49	LD
BK1/1158,6	1158.6	1390	0.15	10.33	A
BK1/1180,5	1180.5	909	0.04	7.95	LD
BK1/1190,1	1190.1	778		13.84	D
BK1/1199,2	1199.2	577	0.01	10.65	D
BK1/1210	1210	569	0.03	7.67	D
BK1/1239,1	1239.1	558		4.96	D
BK1/1266,7	1266.7	616		9.26	D
BK1/1270,4	1270.4	568		8.61	D
BK1/1283,9	1283.9	847	0.01	7.85	D
BK1/1284,1	1284.1	553	0.01	7.94	LD

BK1/1292,8	1292.8	761	0.01	8.34	D
BK1/1303,2	1303.2	588		8.91	D
BK1/1312,8	1312.8	514	0.01	9.76	D
BK1/1322,4	1322.4	575		11.14	D
BK1/1329,2	1329.2		0.01	10.33	D
BK1/1341,7	1341.7	533	0.01	9.20	D
BK1/1350,4	1350.4	564	0.02	8.63	D
BK1/1364,2	1364.2	594	0.03	10.47	D
BK1/1373,5	1373.5	540	0.05	10.77	D
BK1/1377,9	1377.9	501	0.05		D
BK1/1380,7	1380.7	760	0.05	16.07	D
BK1/1382,4	1382.4	570	0.05	17.34	D
BK1/1385,35	1385.35	530	0.06	17.40	D
BK1/1388,4	1388.4	507	0.05	8.45	D
BK1/1391,8	1391.8		0.06	9.69	D
BK1/1397,2	1397.2	569	0.05	9.00	D
BK1/1402,2	1402.2	579	0.07	11.92	D
BK1/1409,4	1409.4	575	0.07	16.92	D
BK1/1416,5	1416.5	566	0.11	11.15	D
BK1/1423,4	1423.4	580	0.10	14.54	D
BK1/1427,4	1427.4	574	0.08	14.55	M
BK1/1428,7	1428.7			16.59	M
BK1/1431,7	1431.7	519	0.10	16.11	M
BK1/1433,2	1433.2	562	0.08	14.20	M
BK1/1439,85	1439.85	557	0.14	13.96	M
BK1/1448,6	1448.6	567	0.12	15.94	LD
BK1/1449,6	1449.6	587	0.13	14.18	LD
BK1/1449,8	1449.8	604	0.16	13.43	M
BK1/1450,1	1450.1	917	0.16	13.69	LD
BK1/1450,5	1450.5	836	0.20	14.04	M
BK1/1451,9	1451.9	587	0.12	17.26	LD
BK1/1453,9	1453.9	931	0.20	15.92	M
BK1/1455,9	1455.9	1173	0.20	15.55	M
BK1/1457,7	1457.7	610	0.15	17.95	M
BK1/1459,3	1459.3	644	0.14	17.16	M
BK1/1463	1463	944	0.21	18.54	M
BK1/1465,1	1465.1	580	0.21	18.04	M
BK1/1466,6	1466.6	654	0.24	18.35	M
BK1/1468,1	1468.1	834	0.24	17.43	M
BK1/1469,9	1469.9	763	0.32	17.31	M
BK1/1472,25	1472.25	811	0.39	14.91	LD
BK1/1472,85	1472.85	826	0.40	12.65	LD
BK1/1477,7	1477.7	940	0.31	9.55	LD
BK1/1486,4	1486.4	4071	0.24	14.46	LD
BK1/1488,5	1488.5	5415	0.25	14.83	M
BK1/1488,85	1488.85	6267	0.27	15.00	M
BK1/1489,45	1489.45	2165	0.24	11.79	LD
BK1/1491,2	1491.2	1285	0.24	14.37	M
BK1/1492,1	1492.1	1582	0.17	14.44	M

BK1/1492,65	1492.65	1962	0.14	16.38	M
BK1/1493,15	1493.15	2056	0.18	15.41	M
BK1/1500,6	1500.6			12.92	D
BK1/1507	1507	851	0.07	12.26	A
BK1/1525	1525	647	0.07	11.91	A
BK1/1532,6	1532.6	557	0.01	16.85	LD
BK1/1537	1537	548	0.01	15.70	LD
BK1/1550,7	1550.7	511	0.07	12.49	D
BK1/1558,2	1558.2	581	0.10	12.45	D
BK1/1567,3	1567.3	526	0.10	10.96	D
BK1/1575,4	1575.4	526	0.14	11.71	D
BK1/1583,4	1583.4	526	0.15	14.78	D
BK3/540	1590		0.14	16.80	T
BK3/552	1602	517	0.24	14.20	LD
BK3/555	1605	511	0.24	14.20	D
BK3/556,85	1606.85	508	0.37	9.00	D
BK3/565	1615	506	0.27	10.00	D
BK3/580,1	1630.1	564	0.33	11.90	D
BK3/590	1640	2647	0.63	9.00	A
BK3/620	1670	638	0.29	11.00	T
BK3/630,7	1680.7	1164	0.41	12.10	T
BK3/650	1700	613	0.38	11.00	D
BK3/660,4	1710.4	504	0.27	10.60	D
BK3/700	1750	1166	0.56	9.40	D
BK3/715	1765	555	0.16	4.60	D
BK3/730	1780	612	0.46	8.60	A
BK3/742	1792	550	0.14	4.00	A
BK3/745,8	1795.8	797	0.43	10.10	LD
BK3/746	1796	942	0.44	11.90	M
BK3/750	1800	541	0.41	10.40	D
BK3/760	1810	635	0.33	9.90	D
BK3/770	1820	637	0.46	7.60	D
BK3/780	1830	856	0.52	9.60	LD
BK3/786,5	1836.5	643	0.44	10.60	LD
BK3/800	1850	752	0.41	9.30	A
BK3/810	1860	734	0.31	10.70	A
BK3/825	1875	836	0.30	10.60	LD
BK3/885	1935	556	0.56	5.60	A
BK3/900	1950	627	0.46	8.90	D
BK3/920	1970	803	0.42	10.30	D
BK3/926,5	1976.5	1851	0.57	10.40	D
BK3/928	1978	2037	0.54	12.50	M
BK3/931,5	1981.5	1702	0.63	10.60	M
BK3/938	1988	646	0.39	10.50	D
BK3/950,2	2000.2	521	0.44	11.40	LD
BK3/960	2010	538	0.48	12.30	D
BK3/970	2020	562	0.44	11.70	D
BK3/1000	2050	810	0.49	12.00	LD
BK3/1015	2065	516	0.56	12.20	D

BK3/1030	2080	521	0.69	12.60	D
BK3/1040	2090	527	0.80	13.70	D
BK3/1040	2090	537	0.79	13.60	D
BK3/1050	2100	520	0.66	12.40	D
BK3/1060	2110	522	0.82	13.60	D
BK3/1070	2120	517	0.78	13.30	D
BK3/1080	2130	513	0.64	11.90	D
BK3/1090	2140	551	0.77	11.80	D
BK3/1102,8	2152.8	702	0.64	12.10	G
BK3/1102,8	2152.8	697	0.65	12.10	G
BK3/1112	2162	518	0.67	12.00	G
BK3/1121,4	2171.4	518	0.67	11.80	G
BK3/1133,3	2183.3	527	0.73	11.90	G
BK3/1145,2	2195.2	531	0.72	13.70	G
BK3/1152,5	2202.5	514	0.58	10.80	G
BK3/1160	2210	520	0.56	10.60	G
BK3/1175	2225	523	0.70	11.50	G
BK3/1185,2	2235.2	538	0.84	13.20	G
BK3/1200	2250	584	1.07	7.50	G
BK3/1202	2252	556	0.82	11.10	LG
BK3/1204	2254	530	0.87	11.90	LG
BK3/1208	2258	515	1.02	12.40	LG
BK3/1212,25	2262.25	516	1.03	12.50	G
BK3/1219,8	2269.8	505	0.99	11.70	G
BK3/1224	2274	509	1.05	10.70	G
BK3/1228	2278	526	0.96	10.60	G
BK3/1231,7	2281.7	528	1.08	8.10	G
BK3/1238,1	2288.1	546	1.07	7.80	G
BK3/1240,7	2290.7	575	1.03	12.60	LG
BK3/1240,7	2290.7	573	1.06	13.00	LG
BK3/1245	2295	584	1.06	12.40	G
BK3/1250	2300	588	1.16	7.20	G
BK3/1254	2304	537	1.20	9.70	G
BK3/1260,5	2310.5	573	1.09	12.10	G
BK3/1267,8	2317.8	630	1.08	10.60	LG
BK3/1268,9	2318.9	694	1.16	12.10	LG
BK3/1271,2	2321.2	669	0.95	10.80	LG
BK3/1272	2322	753	1.03	11.80	G
BK3/1272,9	2322.9	756	1.00	11.10	G
BK3/1275	2325	610	1.10	10.00	G
BK3/1280	2330	661	1.16	11.30	G
BK3/1281	2331	598	1.11	11.60	LG
BK3/1285	2335	678	1.23	6.90	G
BK3/1289	2339	716	1.23	8.40	G
BK3/1290	2340	807	1.18	12.20	G
BK3/1292,55	2342.55	1037	1.13	12.00	M
BK3/1295	2345	569	1.12	12.60	LG
BK3/1303	2353	524	1.18	11.10	G
BK3/1305	2355	575	1.12	11.70	G

BK3/1314,7	2364.7	522	1.01	10.20	G
BK3/1326,8	2376.8	529	1.03	11.30	G
BK3/1333,95	2383.95	548	1.03	11.90	M
BK3/1334,05	2384.05	570	0.95	11.50	M
BK3/1338,1	2388.1	586	1.02	12.00	LG
BK3/1342,6	2392.6	566	1.12	11.60	LG
BK3/1360	2410	712	1.09	9.10	LG
BK3/1368,95	2418.95	1329	1.05	11.20	G
BK3/1373	2423	1256	1.05	9.50	G
BK3/1374,8	2424.8	1624	1.11	11.80	M
BK3/1375,85	2425.85	2442	1.22	13.10	M

Sample number denotes sample depth in m in drill core.

Table C13. Bellevue Drill Core Visually Estimated Abundances from Ashwal et al. (2005)

Lithology	Depth in drill core (m)	Magnetite (%)	Plag (%)	Olivine (%)	Opx (%)	Inv Pig (%)	Cpx (%)	Total Px (%)	Apatite (%)	Biotite (%)	Amphibole (%)	Quartz (%)
Olivine Ferrodiorite	83.69	10	45	16	0	0	12	12	2	0	8	7
Olivine Ferrodiorite	103.88	10	39	20	0	0	8	8	2	6	6	4
Olivine Ferrodiorite	105.23	7	39	18	0	0	5	5	3	2	15	7
Olivine Ferrodiorite	106.20	5	40	20	0	0	4	4	2	4	15	5
Olivine-Orthopyroxene Ferrodiorite	157.07	10	42	10	15	3	1	19	7	5	7	0
Magnetite-Olivine Norite	158.46	11	32	21	15	0	0	15	6	4	11	0
Magnetite Norite	269.25	10	33	0	40	0	0	40	4	4	7	2
Nelsonite	304.72	45	0	0	2	0	2	4	40	4	7	0
Magnetite-Plag-Opx Rock	305.44	65	16	0	10	0	0	10	0	2	7	0
Magnetite Norite	306.10	10	28	0	40	0	5	45	2	7	2	4
Magnetite Gabbronorite	311.16	7	42	0	20	0	20	40	0	0	5	3
Magnetite Gabbro	318.14	10	39	0	0	0	40	40	0	2	7	2
Ferrogabbro	318.26	7	40	0	0	0	40	40	0	3	7	2
Sulfide-Magnetite-Amph Gabbro	328.87	25	42	0	0	0	10	10	2	1	20	0
Magnetite-Plag-Olivine Rock	351.13	55	40	5	0	0	0	0	0	0	0	0
Magnetite-Plagioclase Rock	351.70	80	10	0	0	0	7	7	0	0	3	0
Quartz Anorthosite (altered)	352.10	3	83	0	0	0	0	0	0	4	0	10
Quartz Anorthosite	352.60	3	87	0	0	0	0	0	0	3	0	7
Quartz Anorthosite	417.90	1	87	0	0	0	0	0	0	0	2	10
Olivine Gabbro	420.38	4	58	18	3	0	10	13	0	3	4	0
Magnetite Olivine Gabbro	440.82	10	53	18	0	0	15	15	0	4	0	0
Olivine Gabbro	459.99	7	57	15	0	0	15	15	3	2	1	0
Magnetite Olivine Gabbro	462.66	10	46	15	3	0	18	21	3	5	0	0
Magnetite Olivine Gabbro	485.78	13	50	15	0	0	15	15	3	4	0	0
Magnetite Olivine Gabbro	506.10	15	47	22	0	0	8	8	6	2	0	0
Magnetite Olivine Norite	529.07	15	42	18	0	20	0	20	5	0	0	0
Magnetite Troctolite	549.36	10	39	40	0	0	3	3	6	2	0	0
Magnetite Olivine Gabbronorite	559.16	10	44	15	10	0	10	20	8	3	0	0
Magnetite Olivine Gabbronorite	567.03	10	37	20	0	5	17	22	9	2	0	0

Magnetite Olivine Gabbro	568.24	12	40	25	0	0	10	10	8	3	2	0
Magnetite Olivine Gabbro	571.10	12	43	30	0	0	10	10	5	0	0	0
Magnetite Olivine Gabbro	588.56	20	54	8	0	0	12	12	0	3	3	0
Magnetite Troctolite	588.67	60	22	15	0	0	0	0	0	3	0	0
Magnetite-Olivine Norite	589.85	10	62	15	10	0	2	12	0	1	0	0
Magnetite-Olivine Rock	590.22	45	20	31	0	0	0	0	0	4	0	0
Olivine Gabbro	590.25	7	61	18	2	0	5	7	2	5	0	0
Magnetite-Olivine Gabbro	590.50	40	32	20	0	0	5	5	0	3	0	0
Magnetite-rich Norite	602.90	35	40	0	10	0	1	11	2	7	5	0
Magnetitite (Layer Q)	603.60	90	6	0	2	0	2	4	0	0	0	0
Magnetite Gabbronorite	603.67	45	35	0	10	0	8	18	0	2	0	0
Altered Leucogabbronorite	608.80	1	79	0	10	0	10	20	0	0	0	0
Magnetite Gabbronorite	611.56	25	54	0	8	0	7	15	0	4	2	0
Magnetite Gabbronorite	611.76	50	42	0	5	0	3	8	0	0	0	0
Magnetite-Plagioclase Rock	612.00	30	62	0	0	0	0	0	0	5	3	0
Magnetite Olivine Gabbronorite	618.53	12	45	4	0	15	17	32	0	4	3	0
Magnetite Olivine Gabbro	622.68	17	61	15	0	1	3	4	0	3	0	0
Magnetite Gabbronorite	644.80	10	60	0	20	0	10	30	0	0	0	0
Leucogabbro	646.70	8	67	0	0	0	13	13	0	3	3	6
Magnetite Olivine Gabbro	671.08	9	59	12	0	2	10	12	1	7	0	0
Magnetite Pyroxenite	687.30	20	5	0	40	0	35	75	0	0	0	0
Magnetite Olivine Gabbro	689.49	10	57	8	0	0	23	23	0	2	0	0
Magnetite Olivine Gabbronorite	717.98	11	44	15	9	0	20	29	0	1	0	0
Magnetite Olivine Gabbro	739.61	11	60	11	2	0	15	17	0	1	0	0
Magnetite Olivine Gabbronorite	761.18	10	49	15	0	5	20	25	0	1	0	0
Magnetite Olivine Gabbronorite	784.22	16	57	9	0	6	11	17	0	1	0	0
Magnetite Olivine Gabbronorite	800.50	20	53	12	0	9	5	14	0	1	0	0
Magnetite Olivine Melagabbronorite	802.62	12	35	23	0	8	22	30	0	0	0	0
Magnetite Gabbronorite	806.02	30	42	0	18	0	8	26	0	2	0	0
Magnetite Olivine Gabbronorite	806.49	22	41	14	0	10	10	20	0	3	0	0
Magnetite Gabbronorite	826.41	17	42	0	0	20	20	40	0	1	0	0
Magnetite-Plagioclase Rock	830.57	55	42	0	0	0	0	0	0	3	0	0
Magnetite-Olivine Norite	830.62	40	40	6	10	0	0	10	0	4	0	0

Magnetite-Plagioclase Rock	830.75	60	29	0	5	0	3	8	0	3	0	0
Magnetitite	830.86	93	5	0	0	0	0	0	0	1	1	0
Magnetite Gabbronorite	847.42	12	55	0	0	15	16	31	0	2	0	0
Magnetitite (Layer L)	848.80	88	8	0	0	0	0	0	0	2	2	0
Magnetitite (Layer L)	849.56	90	6	0	1	0	0	1	0	3	0	0
Melagabbronorite	853.62	7	35	0	0	35	17	52	0	4	2	0
Anorthosite	859.70	2	92	0	0	3	1	4	0	2	0	0
Olivine Leucogabbronorite	871.58	8	70	7	0	6	4	10	0	3	2	0
Leucogabbro	877.75	6	75	0	0	0	7	7	0	2	3	7
Olivine-bearing Leucogabbronorite	882.05	7	68	5	6	6	6	18	0	2	0	0
Quartz Leucogabbronorite	885.18	8	73	0	4	0	11	15	0	2	0	2
Magnetite Leucogabbronorite	885.63	12	71	0	0	7	5	12	0	4	0	1
Anorthosite	893.90	2	88	0	0	0	2	2	0	2	1	5
Leucogabbronorite	894.00	8	74	0	0	10	5	15	0	2	1	0
Altered Anorthosite	901.10	0	95	0	0	0	0	0	0	5	0	0
Magnetitite (Layer K)	901.26	97	2	0	0	0	0	0	0	1	0	0
Leucogabbronorite	901.54	8	61	2	2	8	14	24	0	0	5	0
Magnetitite (just above Layer J)	902.78	100	0	0	0	0	0	0	0	0	0	0
Magnetite-Plagioclase Rock	903.00	35	59	0	2	0	0	2	0	4	0	0
Magnetite Gabbronorite	903.08	40	44	0	4	0	5	9	0	2	5	0
Magnetite Gabbronorite	904.53	10	47	0	0	25	15	40	0	3	0	0
Leucogabbronorite	910.10	3	68	0	0	10	10	20	0	3	2	4
Magnetite Leuconorite	917.35	12	64	0	0	20	2	22	0	2	0	0
Leucogabbronorite	920.83	7	67	0	4	6	7	17	0	3	5	1
Leucogabbro	924.10	6	71	0	5	2	11	18	0	4	0	1
Magnetite Gabbronorite	930.40	50	27	0	6	0	10	16	0	2	5	0
Magnetite-Olivine Gabbronorite	930.56	55	19	8	6	0	5	11	0	5	2	0
Leucogabbronorite	949.05	5	66	0	0	10	15	25	0	3	0	1
Magnetite-Olivine-Plag Rock	960.28	45	41	10	0	0	0	0	0	4	0	0
Magnetite-Plagioclase Rock	966.28	40	49	0	0	0	5	5	0	5	1	0
MagnetiteGabbronorite	969.50	14	66	0	0	10	7	17	0	3	0	0
Leuconorite	976.31	5	71	0	0	11	4	15	3	4	2	0
Magnetite-Olivine-Plag Rock	978.00	55	30	12	0	0	0	0	0	3	0	0

Magnetite Leucogabbro	980.00	10	72	0	2	0	8	10	0	3	5	0
Leucogabbro	983.51	4	72	0	2	0	12	14	1	6	2	1
Norite	997.30	5	52	0	25	7	5	37	0	4	0	2
Magnetite-Plagioclase Rock	1002.04	40	49	0	2	0	8	10	0	1	0	0
Magnetite-Plagioclase Rock	1002.28	30	48	0	5	0	10	15	0	3	4	0
Magnetite-Olivine Norite (pegm.)	1002.50	50	20	10	15	0	5	20	0	0	0	0
Leucogabbronorite	1025.54	7	84	0	3	0	4	7	0	2	0	0
Anorthosite	1028.03	3	91	0	0	0	0	0	0	0	6	0
Magnetite Anorthosite	1028.04	10	81	0	0	0	0	0	0	2	7	0
Leucogabbronorite	1041.22	4	70	0	0	9	14	23	0	2	1	0
Quartz Anorthosite	1046.50	2	87	0	0	0	0	0	0	1	0	10
Quartz Leucogabbro	1048.81	2	75	0	0	0	17	17	0	0	4	2
Hydrated Leucogabbro	1049.09	3	72	0	0	0	0	0	0	5	20	0
Leucogabbro (hydrated)	1049.26	8	78	0	0	0	0	0	0	5	9	0
Magnetitite	1049.30	100	0	0	0	0	0	0	0	0	0	0
Magnetite Leucogabbronorite	1065.36	11	75	0	0	6	6	12	0	2	0	0
Magnetite Leuconorite	1067.60	10	77	0	5	0	0	5	1	4	0	3
Quartz Leucogabbronorite	1070.94	5	76	0	0	5	5	10	0	2	3	4
Quartz Leucogabbro	1070.95	4	75	0	0	0	8	8	1	2	4	6
Leuconorite (altered)	1079.50	1	65	0	25	0	0	25	0	0	5	4
Magnetite Leuconorite (altered)	1083.06	10	69	0	5	0	0	5	0	3	10	3
Leucogabbro	1086.17	6	76	0	0	0	10	10	0	3	5	0
Anorthosite	1088.10	2	87	0	8	0	0	8	0	1	0	2
Leucogabbro (altered)	1090.20	3	82	0	0	0	5	5	0	2	8	0
Leuconorite	1102.19	5	81	0	5	0	0	5	1	2	0	6
Anorthosite	1105.50	2	88	0	0	0	6	6	0	1	0	3
Leucogabbro	1118.50	7	79	0	0	0	8	8	0	2	4	0
Leucogabbro (altered)	1126.92	2	82	0	0	0	10	10	0	1	0	5
(Qtz) Magnetite Leucogabbronorite	1138.20	10	78	0	3	0	3	6	0	2	1	3
Leucogabbro	1144.80	7	76	0	1	0	12	13	0	2	2	0
Magnetite Leucogabbronorite	1145.84	10	70	0	0	3	6	9	0	3	8	0
Leucogabbro	1146.00	8	81	0	0	0	3	3	0	5	0	3
Leucogabbronorite	1172.00	0	76	0	0	10	12	22	0	0	0	2

Leucogabbro	1173.10	1	81	0	0	0	10	10	0	0	2	6
Leucogabbronorite	1194.43	10	73	0	10	0	5	15	0	2	0	0
Magnetite Gabbronorite	1212.19	15	68	0	9	0	7	16	0	1	0	0
Gabbronorite	1216.13	8	57	0	25	0	10	35	0	0	0	0
Magnetite Gabbronorite	1237.50	10	47	0	15	0	25	40	0	3	0	0
Magnetite Gabbronorite	1260.24	10	48	0	15	0	25	40	0	2	0	0
Gabbronorite	1279.93	10	50	0	20	0	20	40	0	0	0	0
Gabbronorite	1280.25	7	43	0	22	0	26	48	0	2	0	0
Magnetite Leucogabbronorite	1302.79	12	70	0	10	0	5	15	0	3	0	0
Magnetite Gabbronorite	1316.52	30	52	0	10	0	5	15	0	3	0	0
Magnetite Norite	1316.54	35	45	0	12	0	3	15	0	5	0	0
Leucogabbronorite	1318.50	9	81	0	6	0	3	9	0	1	0	0
Leucogabbronorite	1322.00	8	84	0	3	0	3	6	0	2	0	0
Magnetite Leucogabbronorite	1327.68	10	79	0	3	0	5	8	0	2	1	0
Magnetite Anorthosite	1328.00	9	89	0	0	0	0	0	0	2	0	0
Magnetite-Plagioclase Rock (Layer F)	1334.25	45	53	0	0	0	0	0	0	2	0	0
Magnetite-Plagioclase Rock	1334.50	40	58	0	1	0	1	2	0	0	0	0
Magnetite Norite	1334.55	35	58	0	5	0	0	5	0	2	0	0
Leucogabbronorite	1348.54	8	72	0	8	3	6	17	0	2	1	0
Norite	1355.00	0	56	0	0	40	4	44	0	0	0	0
Leuconorite	1362.30	2	84	0	4	0	0	4	1	3	2	4
Leucogabbro	1371.65	8	84	0	1	0	7	8	0	0	0	0
Anorthosite (altered)	1374.84	0	95	0	0	0	5	5	0	0	0	0
Magnetite-Plagioclase Rock (Layer D)	1379.61	45	46	0	3	0	3	6	0	3	0	0
Anorthosite	1381.00	0	95	0	0	0	5	5	0	0	0	0
Quartz Anorthosite	1382.20	3	87	0	0	0	5	5	0	0	0	5
Quartz Anorthosite	1382.24	0	90	0	0	0	3	3	0	3	0	4
Leucogabbronorite	1395.49	9	81	0	4	0	4	8	1	1	0	0
Magnetite-Plagioclase Rock	1397.05	60	35	0	0	0	0	0	0	5	0	0
Magnetitite (Layer C)	1397.15	85	8	0	0	0	0	0	0	7	0	0
Magnetite Anorthosite	1402.60	13	82	0	0	0	3	3	0	2	0	0
Magnetitite	1403.07	93	0	0	0	0	0	0	0	7	0	0
Magnetite-Plagioclase Rock	1403.17	75	25	0	0	0	0	0	0	0	0	0

Magnetite Norite	1404.35	30	53	0	0	10	0	10	0	4	3	0
Magnetite-Plagioclase Rock	1404.40	40	53	0	5	0	0	5	0	2	0	0
Anorthosite (altered)	1413.44	0	86	0	0	4	2	6	0	1	4	3
Anorthosite	1413.80	0	94	0	0	0	2	2	0	0	0	4
Norite	1437.43	0	45	0	0	50	5	55	0	0	0	0
Anorthosite	1447.80	0	94	0	0	0	3	3	0	0	0	3
Leucogabbronorite	1454.35	6	78	0	0	4	5	9	0	3	2	2
Leucogabbronorite	1470.20	2	77	0	15	0	5	20	0	0	0	1
Anorthosite (altered)	1476.88	2	84	0	0	0	3	3	0	3	5	3
Gabbronorite	1483.34	2	42	0	20	5	20	45	0	5	2	4
Leucogabbronorite	1503.67	1	83	0	8	0	7	15	0	1	0	0
Anorthosite	1510.00	0	97	0	0	0	2	2	0	0	0	1
Quartz Leucogabbro	1520.33	6	84	0	0	0	2	2	0	2	1	5
Anorthosite	1522.99	4	89	0	0	0	6	6	0	1	0	0
Magnetite Gabbro	1534.91	12	43	0	4	0	41	45	0	0	0	0
Magnetite Gabbronorite	1536.22	10	49	0	20	0	20	40	0	1	0	0
Gabbronorite	1536.91	9	45	0	5	0	40	45	0	1	0	0
Gabbronorite	1539.05	8	36	0	25	0	30	55	0	1	0	0
Magnetite Gabbronorite	1541.03	10	30	0	20	0	40	60	0	0	0	0
Gabbronorite	1542.14	5	35	0	30	0	30	60	0	0	0	0
Gabbronorite	1544.00	5	45	0	20	0	30	50	0	0	0	0
Gabbronorite	1546.15	7	46	0	30	0	15	45	0	2	0	0
Leucogabbronorite	1547.90	9	73	0	0	6	12	18	0	0	0	0
Leucogabbronorite	1548.19	8	70	0	0	10	12	22	0	0	0	0
Gabbronorite	1550.89	8	65	0	0	17	10	27	0	0	0	0
Gabbronorite	1553.65	7	62	0	0	18	13	31	0	0	0	0
Leuconorite	1556.21	8	77	0	0	10	5	15	0	0	0	0
Magnetite Leucogabbronorite	1558.77	11	82	0	0	3	4	7	0	0	0	0
Leuconorite	1560.00	7	83	0	0	7	3	10	0	0	0	0
Magnetitite (Layer A)	1561.77	97	0	0	2	0	0	2	0	1	0	0
Gabbronorite	1562.68	8	68	0	0	15	7	22	0	2	0	0
Gabbronorite	1564.44	6	67	0	0	20	7	27	0	0	0	0
Magnetite Leucogabbro	1566.71	12	79	0	2	0	6	8	0	1	0	0

Leucogabbronorite	1567.32	7	87	0	2	0	4	6	0	0	0	0
Gabbronorite	1568.78	5	63	0	15	0	5	20	0	2	10	0
Magnetite Leuconorite	1572.14	11	70	0	0	15	3	18	0	1	0	0
Magnetite-plagioclase rock	1572.70	15	76	0	0	0	0	0	0	5	4	0
Leucogabbronorite	1573.00	8	87	0	2	0	2	4	0	1	0	0
Leucogabbronorite	1575.12	9	81	0	3	0	2	5	0	5	0	0
Leucogabbronorite UZ-MZ BOUNDARY	1575.81	4	86	0	3	0	3	6	0	2	0	2

Table C14. Bellevue Electron Microprobe Analyses of Magnetite from Ashwal et al. (2005)

Depth in drill core (m)	n	SiO_2 (wt%)	TiO_2 (wt%)	Al_2O_3 (wt%)	Cr_2O_3 (wt%)	V_2O_3 (wt%)	Fe_2O_3 (wt%)	FeO (wt%)	MnO (wt%)	MgO (wt%)	CaO (wt%)	NiO (wt%)	ZnO (wt%)	Total
83.69	2	0.23	8.15	0.43	0.00	0.01	50.84	37.61	0.56	0.10	0.03			**97.96**
98.73	9	0.28	6.66	0.75	0.04	0.07	55.42	37.86	0.19	0.03	0.04			**101.34**
103.88	5	0.25	9.89	2.02	0.03	0.06	45.88	39.99	0.39	0.04	0.03			**98.57**
157.07	8	0.72	10.80	1.48	0.06	0.05	44.87	41.85	0.41	0.04	0.07			**100.35**
269.25	7	0.98	5.21	0.94	0.17	0.15	55.01	36.36	0.23	0.07	0.44			**99.56**
304.72	7	0.37	4.32	1.67	0.05	0.33	58.08	35.91	0.13	0.03	0.04			**100.93**
305.44	7	0.36	16.09	2.49	0.08	0.08	34.58	46.67	0.41	0.03	0.04			**100.83**
306.10	4	2.51	7.38	1.50	0.03	0.14	47.01	39.91	0.03	0.63	0.24	0.00	0.22	**99.60**
311.16	3	0.64	5.93	1.96	0.04	0.09	52.53	36.64	0.32	0.14	0.05			**98.34**
318.14	2	0.33	1.96	0.77	0.02	0.26	62.52	32.80	0.14	0.03	0.10			**98.93**
318.26	2	0.28	1.32	0.66	0.01	0.21	63.78	32.19	0.05	0.01	0.04			**98.55**
328.87	4	0.36	3.72	1.78	2.33	0.25	55.89	34.80	0.33	0.00	0.03			**99.49**
351.13	8	0.14	18.44	3.01	2.31	0.08	26.50	47.53	0.46	0.36	0.03			**98.85**
351.70	7	0.16	17.30	2.74	0.83	0.18	31.04	47.24	0.37	0.12	0.03			**100.01**
440.82	5	0.31	10.70	1.93	0.04	0.02	45.04	41.12	0.29	0.07	0.08			**99.60**
549.36	8	0.23	15.53	2.30	0.04	0.11	36.42	45.81	0.37	0.17	0.06			**101.04**
559.16	8	0.68	14.63	1.51	0.08	0.17	35.28	44.29	0.33	0.04	0.23			**97.24**
568.24	4	0.27	7.42	2.37	0.06	0.26	51.27	38.18	0.21	0.23	0.06			**100.34**
571.10	5	0.15	17.34	2.39	0.05	0.16	27.00	44.66	0.40	0.18	0.07			**92.40**
588.56	5	0.23	18.20	3.23	0.18	0.18	29.34	47.50	0.45	0.54	0.01			**99.86**
588.67	9	0.16	17.14	3.00	0.29	0.18	31.30	46.04	0.38	0.67	0.01			**99.16**
589.85	4	0.18	15.27	3.05	1.13	0.34	32.59	44.94	0.31	0.04	0.06			**97.91**
590.22	5	0.19	18.34	2.94	0.24	0.26	26.70	46.47	0.36	0.43	0.03	0.00	0.14	**96.09**
590.50	10	0.14	22.13	2.88	0.08	0.16	21.51	51.00	0.37	0.31	0.02			**98.60**
602.90	5	0.32	18.95	3.04	0.07	0.38	25.53	48.10	0.38	0.10	0.02			**96.89**
603.67	8	0.13	20.98	3.18	0.08	0.47	24.87	50.13	0.35	0.69	0.02			**100.90**
609.27	10	5.20	19.18	3.21	1.15	0.46	11.67	52.00	0.51	0.61	1.25			**95.25**
611.56	5	0.22	13.88	3.27	0.02	0.57	36.18	42.73	0.30	0.72	0.03			**97.92**
611.59	7	0.12	10.19	2.47	0.81	0.46	44.26	39.44	0.24	0.64	0.04			**98.67**

611.76	8	0.17	18.69	3.05	0.03	0.37	26.58	47.25	0.31	0.41	0.02		**96.88**
618.53	10	0.27	14.77	3.04	0.08	0.52	35.80	45.26	0.38	0.04	0.02		**100.19**
644.80	10	0.14	14.86	4.12	1.30	0.56	34.20	44.93	0.20	0.61	0.01		**100.92**
646.70	3	5.09	7.74	3.26	0.96	0.43	35.53	43.78	0.15	0.60	0.03		**97.57**
671.08	5	0.23	14.71	2.66	0.02	0.12	36.25	44.12	0.38	0.41	0.02		**98.92**
687.30	7	0.19	11.73	2.06	0.07	0.12	42.62	41.84	0.26	0.06	0.05		**99.00**
689.49	4	0.33	11.24	2.84	0.03	0.12	41.69	41.41	0.17	0.13	0.02		**97.98**
739.61	5	0.27	14.57	2.81	0.10	0.15	36.18	44.08	0.31	0.36	0.15		**98.98**
761.81	4	0.25	14.59	2.83	0.05	0.31	35.28	44.09	0.30	0.25	0.03		**97.97**
800.50	8	0.15	17.27	2.87	0.04	0.20	31.80	46.58	0.33	0.51	0.03		**99.79**
802.62	5	0.25	15.61	2.87	0.04	0.35	34.52	45.50	0.35	0.30	0.02		**99.81**
806.02	8	0.17	17.36	2.64	0.04	0.30	30.08	46.30	0.31	0.29	0.04		**97.53**
806.49	1	0.23	17.27	2.35	0.14	0.16	30.26	46.49	0.32	0.12	0.00		**97.35**
826.41	5	0.20	16.03	3.13	0.04	0.72	31.71	45.27	0.34	0.29	0.01		**97.75**
830.62	10	0.14	17.08	3.07	0.07	0.65	30.96	46.47	0.34	0.35	0.04		**99.17**
830.75	8	0.16	15.61	2.69	0.09	0.72	32.51	44.49	0.34	0.28	0.03		**96.92**
830.86	9	0.15	14.60	2.97	0.03	0.67	35.69	42.83	0.34	1.07	0.02		**98.36**
847.42	6	0.20	15.88	2.53	0.13	0.67	33.71	45.74	0.38	0.09	0.07	0.00	0.00	**99.40**
848.80	8	0.22	17.30	1.08	0.12	0.80	31.60	46.40	0.32	0.15	0.05			**98.04**
849.56	10	0.23	17.77	1.25	0.09	0.72	31.07	45.53	0.26	1.08	0.03			**98.03**
853.62	2	0.53	5.16	1.03	0.04	1.10	54.94	35.66	0.15	0.14	0.24		0.19	**99.18**
871.58	5	1.44	11.54	1.42	0.34	1.16	38.98	42.67	0.26	0.19	0.14			**98.14**
877.75	2	0.46	3.54	1.16	0.12	1.20	56.57	33.99	0.16	0.02	0.14			**97.36**
882.05	8	0.56	14.25	2.14	0.28	1.18	37.49	45.53	0.25	0.11	0.05			**101.85**
885.18	7	6.15	14.47	2.56	0.16	1.48	20.27	49.99	0.28	0.45	1.06			**96.87**
885.63	6	0.31	13.43	0.96	0.11	1.31	39.43	43.64	0.21	0.02	0.08			**99.50**
894.00	7	0.98	12.70	2.47	0.05	1.32	37.03	43.45	0.27	0.26	0.04			**98.57**
901.26	10	0.14	12.13	2.46	0.12	1.08	42.62	41.41	0.24	1.09	0.03			**101.32**
901.54	5	1.21	7.29	3.73	0.15	1.02	44.84	37.63	0.17	0.84	0.05			**96.93**
902.78	12	0.15	15.08	1.72	0.10	0.98	35.27	42.40	0.28	1.33	0.02			**97.33**
903.00	2	0.05	11.24	1.92	0.10	n.a.	45.23	41.66	0.28	0.04	0.05			**100.57**
903.06	9	0.15	13.44	3.51	0.39	1.03	37.19	42.05	0.30	1.13	0.04			**99.22**
903.08	2	0.24	6.45	2.39	0.04	1.18	50.46	36.93	0.15	0.02	0.02			**97.88**

904.53	9	0.37	9.41	2.87	0.08	1.17	45.73	40.45	0.23	0.15	0.04		**100.50**
910.10	1	0.06	5.70	0.64	0.07	n.a.	58.36	36.89	0.22	0.00	0.02		**101.95**
917.35	4	1.12	7.53	1.13	0.07	1.26	48.78	38.71	0.14	0.38	0.06		**99.18**
920.83	9	0.43	2.82	1.59	0.03	1.17	59.65	34.29	0.13	0.09	0.04		**100.24**
924.10	5	0.48	6.50	1.51	0.06	1.34	50.87	37.09	0.18	0.10	0.01		**98.13**
930.40	2	0.15	11.91	3.33	0.22	0.98	42.96	41.66	0.31	1.14	0.02		**102.68**
930.56	9	0.13	12.01	2.84	0.11	0.99	41.23	40.76	0.28	1.07	0.03		**99.45**
949.05	7	0.21	9.26	2.08	0.03	1.16	46.60	39.86	0.24	0.01	0.03		**99.48**
960.28	4	0.09	13.72	2.46	0.02	1.26	37.13	42.17	0.29	0.79	0.06		**97.99**
966.28	8	0.62	13.82	2.61	0.14	1.29	36.38	44.50	0.32	0.20	0.04		**99.91**
976.31	5	0.56	6.88	2.05	0.07	1.00	49.01	36.93	0.18	0.14	0.07	0.06	0.24	**97.19**
978.00	6	0.13	12.94	3.24	0.06	1.20	36.85	40.92	0.29	0.78	0.01	0.09	0.39	**96.90**
980.00	7	0.19	3.37	2.82	0.07	1.26	54.46	33.47	0.14	0.01	0.01			**95.79**
983.51	2	0.22	7.82	2.29	0.20	1.07	47.32	37.65	0.28	0.08	0.00	0.03	0.00	**96.96**
997.30	3	0.89	4.93	1.27	0.06	1.41	52.42	35.36	0.19	0.32	0.04			**96.89**
1002.04	4	0.13	11.99	2.53	0.18	1.27	41.77	42.06	0.25	0.43	0.05			**100.66**
1002.28	4	0.22	4.41	1.65	0.07	1.33	57.02	35.69	0.17	0.04	0.01			**100.61**
1002.50	9	0.19	12.44	3.81	0.08	0.83	39.08	41.16	0.03	1.29	0.03			**98.94**
1025.54	5	4.49	12.22	2.66	0.06	1.01	28.76	45.72	0.18	1.11	0.13			**96.34**
1028.03	1	0.39	1.63	0.87	0.21	1.48	61.23	32.67	0.00	0.10	0.00			**98.58**
1028.04	4	0.37	0.33	0.33	0.03	1.53	66.04	31.96	0.09	0.06	0.01			**100.74**
1041.22	5	1.29	10.97	2.74	0.20	n.a.	39.82	41.98	0.15	0.33	0.01	0.00		**97.49**
1048.81	1	0.18	5.44	2.56	0.12	0.57	53.88	36.39	0.05	0.03	0.07			**99.28**
1049.09	6	0.20	0.72	0.42	0.09	1.69	63.09	31.16	0.04	0.03	0.04			**97.49**
1049.26	8	0.19	5.53	1.97	0.07	1.61	53.89	36.61	0.15	0.03	0.02			**100.07**
1049.28	7	0.16	6.44	1.98	0.05	1.38	52.95	36.50	0.11	0.70	0.01			**100.27**
1065.36	10	1.84	10.90	2.88	0.14	1.29	36.10	41.60	0.29	0.29	0.26	0.05	0.19	**95.84**
1067.60	9	0.59	7.61	1.91	0.30	1.38	47.51	38.22	0.24	0.06	0.04			**97.86**
1070.94	1	10.57	13.62	2.59	0.00	1.38	14.00	48.58	0.09	0.78	6.62			**98.23**
1070.95	5	1.21	1.95	0.88	0.04	0.60	59.64	33.49	0.15	0.27	0.03			**98.25**
1083.06	6	0.22	0.26	0.29	0.05	1.25	65.61	31.18	0.08	0.04	0.01			**98.99**
1086.17	5	0.57	0.63	0.35	0.13	1.58	64.05	31.87	0.04	0.12	0.20			**99.55**
1090.20	3	0.25	0.53	0.27	0.08	1.31	64.57	31.24	0.08	0.08	0.00			**98.41**

1102.19	8	3.34	7.58	1.07	0.11	1.11	44.33	39.43	0.37	0.30	2.00			**99.64**
1105.50	4	5.38	6.86	1.95	0.17	1.20	37.93	39.18	0.36	0.68	2.77			**96.48**
1118.50	6	9.33	11.33	1.58	0.12	1.48	21.71	44.58	0.06	0.20	7.29			**97.67**
1126.92	2	1.31	2.24	0.37	0.00	0.76	61.14	34.17	0.12	0.09	0.66			**100.85**
1138.20	10	0.27	12.10	2.68	0.31	1.25	38.02	41.85	0.23	0.03	0.01			**96.75**
1144.80	8	2.45	14.05	2.96	0.42	1.12	28.92	45.51	0.19	0.37	0.47			**96.46**
1145.84	8	0.67	9.94	1.33	0.29	1.29	45.05	40.85	0.32	0.08	0.10			**99.92**
1146.00	4	0.21	6.48	1.06	0.45	1.60	51.05	36.33	0.33	0.06	0.06			**97.63**
1212.19	5	0.31	11.55	2.85	0.05	1.22	39.35	40.57	0.23	0.37	0.08	0.05	0.27	**96.88**
1216.13	5	0.19	5.82	1.91	0.04	1.59	53.72	36.93	0.15	0.05	0.04			**100.44**
1237.50	5	0.33	10.25	2.04	0.02	1.26	44.67	40.73	0.27	0.17	0.05			**99.79**
1279.93	11	0.25	10.06	3.18	0.04	1.39	42.69	40.32	0.29	0.09	0.04			**98.35**
1280.25	5	0.25	8.66	2.83	0.04	1.47	46.51	39.33	0.28	0.10	0.02			**99.49**
1302.79	10	0.21	9.61	2.21	0.03	1.50	45.67	40.28	0.23	0.04	0.03			**99.81**
1316.52	8	0.14	11.51	1.98	0.05	1.38	42.90	41.81	0.25	0.17	0.04			**100.24**
1316.54	10	0.17	11.51	3.08	0.02	1.29	40.62	41.51	0.23	0.22	0.04			**98.69**
1322.00	10	0.41	7.73	1.68	0.02	1.66	49.05	38.55	0.20	0.07	0.05			**99.42**
1327.68	7	1.34	8.71	2.50	0.05	1.39	42.68	39.93	0.16	0.17	0.10			**97.03**
1328.00	5	2.09	12.04	2.86	0.14	1.47	34.80	44.08	0.23	0.39	0.07			**98.17**
1334.25	9	0.15	12.18	1.77	0.09	1.45	41.70	41.73	0.32	0.53	0.01			**99.93**
1334.55	8	0.17	12.93	3.90	0.05	1.34	37.72	41.32	0.26	1.36	0.03			**99.09**
1348.54	7	5.49	8.03	2.38	0.08	1.77	34.42	39.96	0.14	0.53	3.57			**96.37**
1362.30	3	0.56	6.20	2.12	0.01	1.23	52.15	37.25	0.16	0.03	0.45			**100.15**
1379.61	10	0.17	12.83	2.53	0.15	1.49	37.01	40.95	0.27	0.81	0.03			**96.24**
1395.49	9	0.20	10.50	3.00	0.32	1.60	42.06	41.08	0.15	0.02	0.04			**98.97**
1397.05	8	0.14	13.03	3.66	0.34	1.40	37.37	43.13	0.26	0.31	0.04			**99.67**
1397.15	10	0.92	13.28	1.82	0.38	1.56	35.61	42.37	0.31	0.86	0.08			**97.19**
1403.07	10	0.17	12.52	2.34	0.05	1.71	40.68	40.98	0.23	1.40	0.01			**100.08**
1403.17	8	0.15	11.88	0.96	0.03	1.71	43.10	41.91	0.26	0.24	0.02			**100.27**
1404.35	6	0.32	10.82	2.46	0.28	1.65	42.46	41.28	0.26	0.09	0.22			**99.84**
1404.40	10	0.22	10.26	3.08	0.29	1.55	42.40	39.86	0.24	0.55	0.02			**98.47**
1454.35	4	0.24	0.54	1.79	0.08	0.65	64.73	32.03	0.09	0.06	0.04			**100.25**
1470.20	4	0.25	3.77	1.85	1.58	1.26	55.77	34.71	0.06	0.18	0.03			**99.46**

1503.67	8	12.26	0.60	2.98	4.18	2.13	27.13	38.69	0.20	4.38	0.78		**93.33**
1522.99	5	0.28	3.61	1.88	4.63	1.30	51.33	34.06	0.22	0.04	0.03		**97.38**
1534.91	5	0.23	9.62	4.12	0.06	2.11	41.12	39.65	0.14	0.27	0.02		**97.34**
1536.22	6	0.19	11.66	2.64	0.09	1.91	41.08	42.11	0.24	0.16	0.07		**100.15**
1536.91	6	0.21	8.67	3.16	0.22	2.29	45.77	39.71	0.24	0.06	0.04		**100.37**
1539.05	6	8.24	9.11	3.02	0.12	2.51	26.93	43.57	0.18	0.69	5.16		**99.53**
1541.03	10	0.15	9.54	3.30	0.09	2.10	43.30	40.01	0.32	0.00	0.03		**98.84**
1542.14	5	0.16	6.91	2.52	0.04	2.11	46.64	36.24	0.26	0.03	0.03		**94.94**
1544.00	5	0.40	7.83	3.14	0.07	2.19	47.54	39.19	0.32	0.07	0.07		**100.82**
1546.15	6	0.70	5.94	1.21	0.46	2.19	49.33	36.00	0.22	0.16	0.13		**96.34**
1547.90	9	0.29	9.03	2.82	0.18	1.99	45.26	39.32	0.32	0.34	0.06		**99.60**
1548.19	6	0.24	7.02	2.76	0.05	2.17	50.29	37.48	0.25	0.31	0.29	0.04	0.16	**101.06**
1550.89	10	0.19	9.17	2.93	0.08	2.20	43.69	38.99	0.25	0.27	0.03		**97.80**
1553.65	8	0.19	8.23	2.78	0.11	2.12	45.59	37.82	0.25	0.39	0.02		**97.51**
1556.21	4	0.28	9.14	3.07	0.23	2.10	43.52	39.17	0.16	0.20	0.22		**98.09**
1558.77	9	0.17	6.54	2.87	0.57	2.39	0.00	0.00	0.14	0.23	0.03		**12.94**
1560.00	8	0.26	7.84	2.19	0.36	2.21	47.75	38.30	0.24	0.13	0.16		**99.44**
1561.77	6	0.23	9.97	3.79	0.76	1.92	42.09	38.81	0.30	1.26	0.01		**99.14**
1562.68	9	0.15	6.51	3.14	0.09	2.21	49.68	37.41	0.16	0.06	0.04		**99.46**
1564.44	8	0.19	10.15	2.56	0.03	1.95	41.53	39.49	0.32	0.18	0.01		**96.41**
1566.71	8	0.21	7.62	2.65	0.08	2.05	47.06	37.47	0.27	0.28	0.02		**97.70**
1567.32	7	0.32	9.52	2.70	0.11	1.91	44.85	39.72	0.23	0.35	0.07	0.06	0.24	**100.08**
1568.78	5	0.20	3.11	0.53	0.09	2.38	56.67	32.81	0.12	0.09	0.03		**96.03**
1572.14	9	0.13	5.27	2.73	0.25	2.43	52.37	35.73	0.16	0.36	0.02		**99.44**
1572.70	7	0.18	4.62	1.45	0.18	2.43	53.72	34.88	0.09	0.10	0.02		**97.67**
1573.00	9	0.19	6.67	2.86	0.26	2.31	48.22	37.03	0.20	0.05	0.05		**97.84**
1575.12	10	0.16	3.51	2.12	0.89	2.08	54.91	33.90	0.21	0.10	0.02		**97.90**
1575.81	10	0.22	2.77	1.38	1.24	2.17	56.42	33.25	0.09	0.06	0.03		**97.63**
1579.72	9	0.19	5.61	1.93	1.18	1.67	50.52	35.69	0.25	0.01	0.02		**97.07**
1580.06	10	0.25	4.85	2.13	1.35	1.81	52.47	35.63	0.19	0.02	0.06		**98.77**
1581.57	7	0.19	2.12	1.17	1.25	1.92	58.05	32.45	0.14	0.07	0.00		**97.36**

Highlighted cells = Magnetitite Layer
n = Number of analyses per sample